INVESTIGATION OF THE GRAIN SIZE, SHAPE, AND TEXTURE OF THE PERSEVERANCE DRIFT, ANTARCTIC PENINSULA: SEDIMENT TRANSPORT HISTORY AND HOLOCENE VARIABILITY

A Thesis

Presented to

the Faculty of the Department of Earth and Atmospheric Science

University of Houston

In Partial Fulfillment

of the Requirements for the Degree

Master of Science

in Geology

By

Alicia Barbara Staszyc

December 2014

INVESTIGATION OF THE GRAIN SIZE, SHAPE,

AND TEXTURE OF THE PERSEVERANCE DRIFT,

ANTARCTIC PENINSULA: SEDIMENT TRANSPORT HISTORY

AND HOLOCENE VARIABILITY

Alicia Barbara Staszyc

APPROVED:

Dr. Julia Smith Wellner

Chair of Committee

Department of Earth and Atmospheric Sciences

Dr. Joel Saylor

Department of Earth and Atmospheric Sciences

Dr. Kyle Strom

Department of Civil and Environmental Engineering

Dean of the College of Natural Sciences and Mathematics

ACKNOWLEDGEMENTS

My sincerest gratitude goes to Dr. Julia Wellner for the opportunity to work with her on this project. Her continuous support and assistance for the past two years have made this journey invaluable. I would also like to extend my appreciation to my colleagues in LARISSA for providing me with data and advice throughout this thesis. This research was funded by the National Science Foundation grant ANT-0732614. I also thank the Antarctic Research Facility at the Florida State University, especially Dr. Charlotte Sjunneskog, for the quick delivery of samples and data when needed. Very special thanks to Dr. John Anderson and Becky Minzoni for allowing me to use their lab at Rice University. My thanks also goes to Daniel Livsey and Dr. Isabelle Charpentier for all of their fruitful assistance in grain shape analysis. I thank Dr. Amy Leventer and Kara Vadman for diatom data. I also express my appreciation to Dr. James Meen and Dr. Karoline Mueller for taking the time to help me with the SEM. I would like to thank Yuribia Muñoz for all of her helpful input and discussions about Antarctica. I am also grateful to Vanessa Alejandro for all of her hard work and assistance with this project. Finally, I would like to thank my dearest parents for all of the support I've ever needed to attain this goal.

INVESTIGATION OF THE GRAIN SIZE, SHAPE,
AND TEXTURE OF THE PERSEVERANCE DRIFT,
ANTARCTIC PENINSULA: SEDIMENT TRANSPORT HISTORY
AND HOLOCENE VARIABILITY

An Abstract of a Thesis

Presented to

the Faculty of the Department of Earth and Atmospheric Science

University of Houston

In Partial Fulfillment

of the Requirements for the Degree

Master of Science

in Geology

By

Alicia Barbara Staszyc

December 2014

Abstract

The Perseverance Drift, on the northern Antarctic Peninsula continental shelf, records changes in ocean and ice conditions throughout the Holocene. This study uses the sedimentary archive contained in a 25.81m jumbo piston core taken from a ~100m thick sedimentary drift deposit. The drift deposit is composed of laminated, black- to olive-colored diatomaceous mud and ooze; several horizons of ikaite crystals occur throughout the section. Grain size, grain shape, and grain textures of sediments in the drift deposit can be used to determine sediment transport history and assess variations in the relative proportions of current-transported, iceberg-rafted, and aeolian-transported sediment. Based on grain size and lithologic description, four sediment facies were assigned. Facies 1 and Facies 3 contain a high abundance of terrigenous material brought to the site by strong currents and aeolian processes to sea ice. The presence of sea ice causes a decrease in phytoplankton growth. The lack of biogenic material amplifies the terrigenous signal. Facies 2 and Facies 4 are dominated by biogenic sedimentation; in these two facies terrigenous sediment is delivered by currents and ice rafting. In all facies, there is an input of terrigenous sediment by aeolian processes. Ikaite occurs throughout the core, and there is no direct correlation between ikaite intervals and the facies. Based on the four facies, two units are assigned to the site: Unit 1, representing a warmer, open marine environment, and Unit 2, representing an open marine environment with varied sea ice. These are interpreted to be a Warm Period, from present to 1,700 cal. yr. BP, and the Neoglacial, from 1,700 to >3,375 cal. yr. BP. The end of the Neoglacial in the Bransfield Basin to the west of the Perseverance Drift occurs at nearly the same time. Grain microtextures show a very high abundance of silica precipitation, covering textures that

would give clues about the transport history to the site. The silica precipitation is interpreted to form quickly and in situ. The high-resolution grain-shape results are inconclusive because authogenically precipitated silica obscures the original shape of the grain.

Table of Contents

Introduction

The Antarctic Peninsula (AP) is a narrow, mountainous region (Figure 1; Heroy and Anderson, 2005). It is covered by approximately 500m of ice (Heroy and Anderson, 2005). Average temperatures on the western AP range from 0 °C to -16 °C from the north to the south, respectively, and temperatures on the eastern AP range from -5 °C to -17 °C from the north to the south, respectively (Figure 2; Morris and Vaughan, 2003; Cook and Vaughan, 2009). Due to storms, which control temperature and precipitation in the AP, the western side of the AP is warmer and wetter, while the eastern side is colder and drier (Reynolds, 1981). Today, the AP is one of the most rapidly warming regions on earth (Turner et al., 2005). It has experienced warming approximately six times faster than the global mean, increasing 3.7±1.6 °C versus 0.6±0.2 °C over the last century (Vaughan et al., 2003). Evidence of this warming can be seen in the collapse of ice shelves in the AP over the past 50 years (Cook et al., 2005). Ice shelves exist from the northern portion of the cold, eastern side and farther south on the warm, western side of the AP, and they remain stable in a range of -5 °C to -9 °C (Vaughan and Doake, 1996). However, since 1992, the loss of ice mass has been increasing by the melting of the base of floating ice shelves and calving of icebergs (Jacobs et al., 2011; Pritchard et al., 2012; Van Ommen, 2013; Williams, 2014). Over the last half century, a decrease in extreme cold events has occurred in the AP (Franzke, 2013). In the northeastern AP, the summer melting has reached levels unprecedented over the past 1,000 years (Abram et al., 2013). In the northwestern AP, the summer warming has increased at a rate of 2.4±1.7 °C per century (Vaughan, 2006).

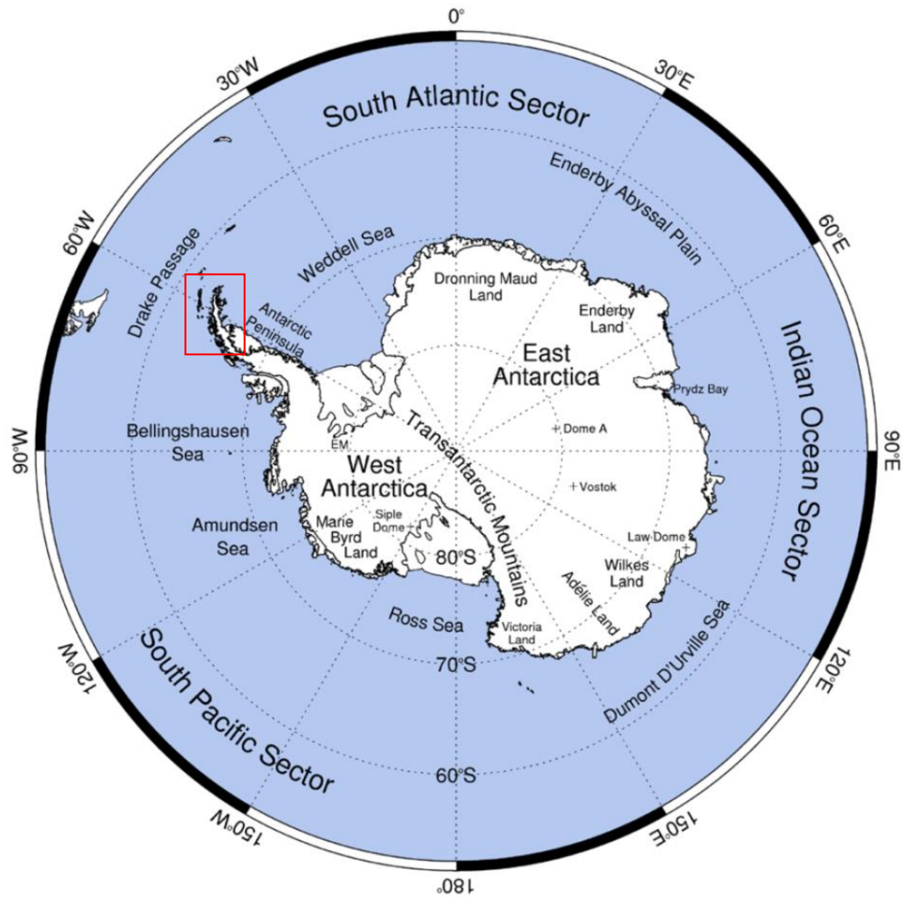

Figure 1: Polar projection map of Antarctica (Turner et al., 2009).

Northern AP study area is marked with a red box.

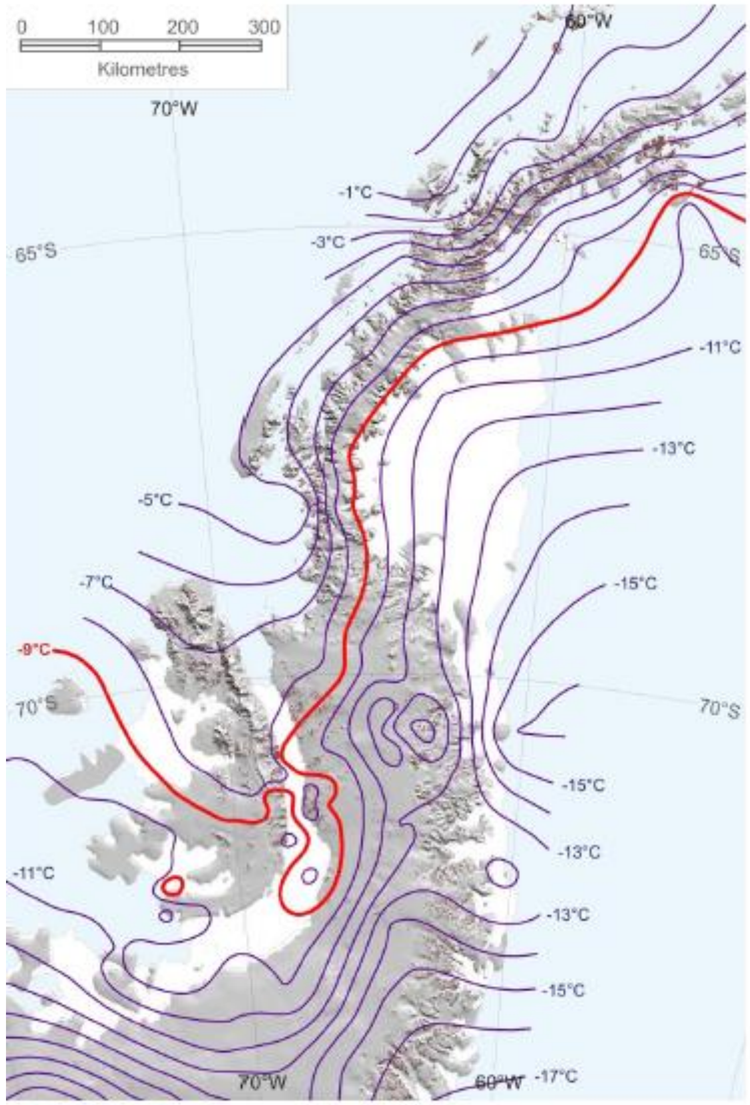

Figure 2: The Antarctic Peninsula with isotherms representing interpolated mean annual temperature. The -9 °C isotherm is represented by red color (Morris and Vaughan, 2003; Cook and Vaughan, 2009).

To understand the paleoclimate changes throughout the Holocene, it is necessary to study the proxy records of marine and terrestrial environments in the region (Bentley et al., 2009). Mulvaney et al. (2012) state that during the late Holocene, the last 2,000 cal. yr. BP, the western AP experienced a warming while the eastern AP experienced a cooling in climate. However, with today's increased anthropogenic warming, it is unclear that this pattern will still remain throughout the AP. With the recent collapses of ice shelves on the eastern AP and synchronous surface melting patterns between the western and eastern AP, it is important to note that the present day temperatures are exceeding the warmest Holocene temperatures and leave the eastern AP vulnerable to ice loss (Domack et al., 2005; Hodgson et al., 2006; Mulvaney et al., 2012; Barrand et al., 2013). Although the entire AP shows evidence of warming conditions, it must be noted that the timing and extent of the retreat of ice sheets is asynchronous, but that this retreat occurs in a general north to south pattern (Cook et al., 2005; Steig et al., 2009; Mulvaney et al., 2012).

Over the past 30 years, the northwestern Weddell Sea surface water has experienced a decrease in salinity, which is a result of collapsing ice shelves in the south (Hellmer et al., 2011). An increase in precipitation over the 20th century on the continental shelf in the western Weddell Sea also contributes to this freshening (Hellmer et al., 2011). The northern AP is influenced by multiple currents (Figure 3). The Weddell Sea Transitional Water Current is a deep water mass which dominates the Bransfield Strait and surrounding regions in the northern AP (Tokarczyk, 1987; Shevenell and Kennett, 2002). The cold, saline Weddell Sea/ Bransfield Strait Surface Water Current flows over the tip of the AP allowing for a mixing between waters and nutrients in northwestern Weddell Sea and the Bransfield Strait (Ishman and Domack, 1994;

Hoffman, 1996; Shevenell and Kennett, 2002; Von Glydenfelt et al., 2002). The upwelling of nutrient-rich water onto the shelf, along with a combination of meltwater from seasonal ice, forms an ideal environment for diatoms to thrive making them the most abundant microfossils in the Antarctic (Maddison et al., 2005). The area of study, the Perseverance Drift, is located in the northern AP and is impacted by the currents in the area.

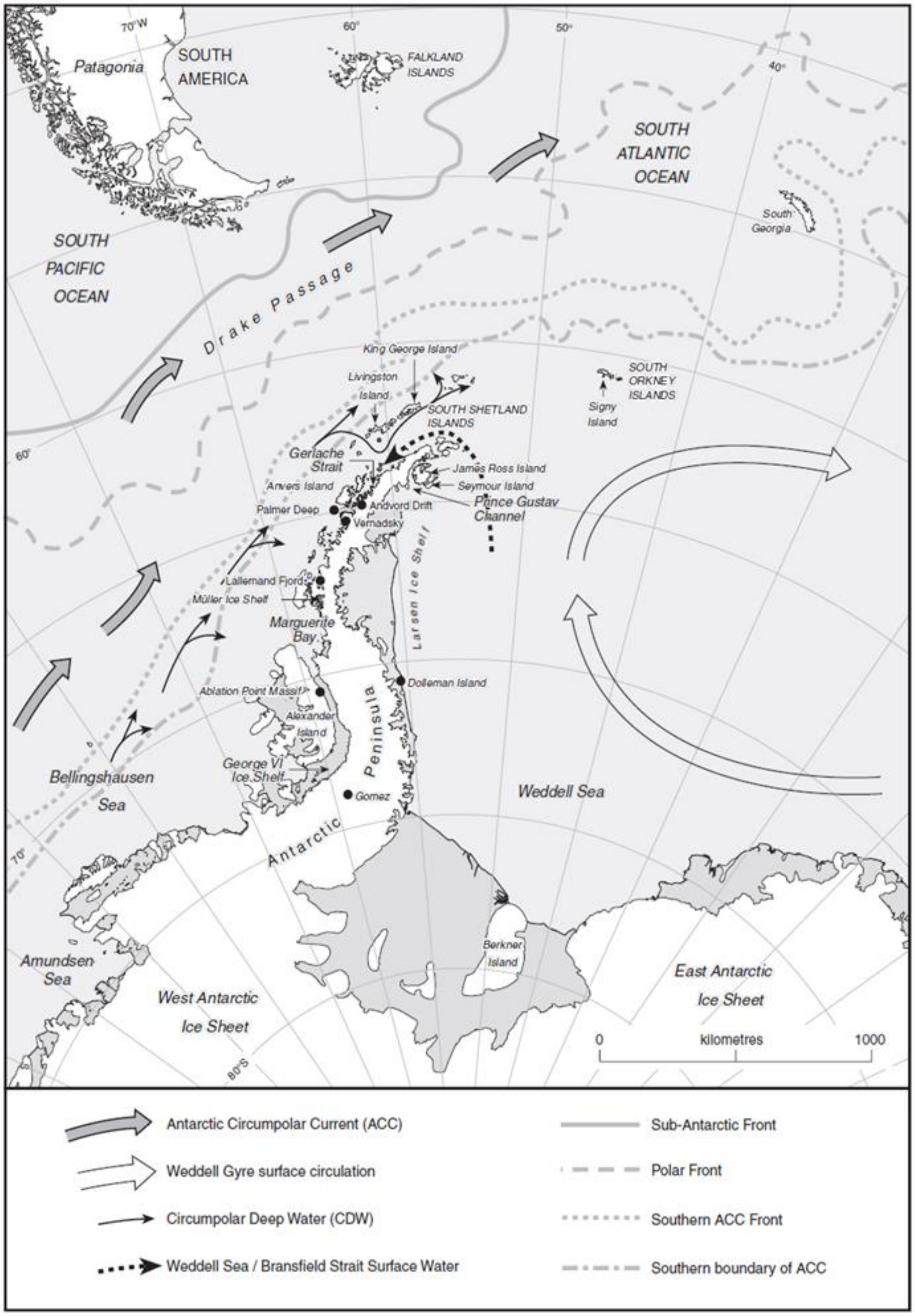

Figure 3: Antarctic Peninsula ocean currents (Bentley et al., 2009). Ocean circulation front boundaries after Orsi et al., (1995), Garabato et al., (2002), and Hernandez-Molina et al., (2006).

The Perseverance Drift is a diatom-rich drift deposit located on the continental shelf in the northeastern AP. Its formation is a result of the complex currents in the region (Figure 3). These currents allow for a high sedimentation rate making the study area useful for late Holocene paleoclimate reconstruction. The Perseverance Drift contains fifteen intervals of a mineral which has the potential to be a paleoclimate proxy, ikaite (Rickaby et al., 2006). The hydration water in the mineral records the $\delta^{18}O$ composition of seawater without temperature controlled fractionation (Rickaby et al., 2006). Despite similar organic-rich sediment occurring throughout the AP, ikaite is only found in locations also characterized by a high sedimentation rate and a high organic component in the northwestern Weddell Sea and the eastern Bransfield Basin (Domack et al., 2007). By studying the grain size, grain shape, and grain texture of the site, evidence of transport history to the site can be observed. This determines the relative roles of glacial transport, current transport, and aeolian transport through time, all of which help constrain the time of past climatic events. If the drift deposit is recording changing sediment transport over time, including not only glacial marine and current deposits but also periods dominated by aeolian influence, then ikaite may form in distinct sediment horizons, which allows development of better understanding on parameters controlling ikaite growth.

Background

Climate

The modern climate of the western AP differs from the eastern AP. Storms, which are formed in the Amundsen Sea, move north to the Bellinghausen Sea, and eventually reach the Drake Passage, are responsible for the warm and moist climate of the western AP (Reynolds, 1981). Conversely, the eastern side of the AP is colder and drier because of the northward movement of cold air masses from the continent into the Weddell embayment and the limited influence of the warm, mid-latitudinal air masses (Reynolds, 1981; Bentley et al., 2009).

Currents

The Antarctic Circumpolar Current (ACC) flows clockwise around the continent (Figure 3; Figure 4). The AP deflects the ACC to the north and through the Drake Passage; therefore the continental shelf of the northern Pacific margin of the AP is sensitive to any current changes (Bentley et al., 2009). The ACC carries the Circumpolar Deep Water current (CDW), which consists of the Upper Circumpolar Deep Water (UCDW), which is characterized by varying temperature and high nutrient concentration, and the Lower Circumpolar Deep Water (LCDW), which is characterized by high salinity (Orsi et al., 1995). Intrusions of LCDW are absent on the Antarctic shelf but intrusions of UCDW onto the shelf do occur (Ducklow et al., 2007). The intrusions contribute warm, salty water to the shelf (Klinck et al., 2004; Bentley et al., 2009). The western AP has experienced ocean warming higher than the global average due to increased presence of UCDW on shelf (Meredith and King, 2005).

The Perseverance Drift is located in the northeastern AP between Joinville Island to the south and D'Urville Island to the north (Figure 4). The site is in the trough at the eastern opening of the Antarctic Sound between the two islands. The unique influence of currents in the northern AP allows for the formation of the Perseverance Drift deposit. Accumulation of sediment on the continental shelf at this site occurs from the deceleration of the Weddell Sea Transitional Water current exiting the Larsen Channel to the east (Figure 5).

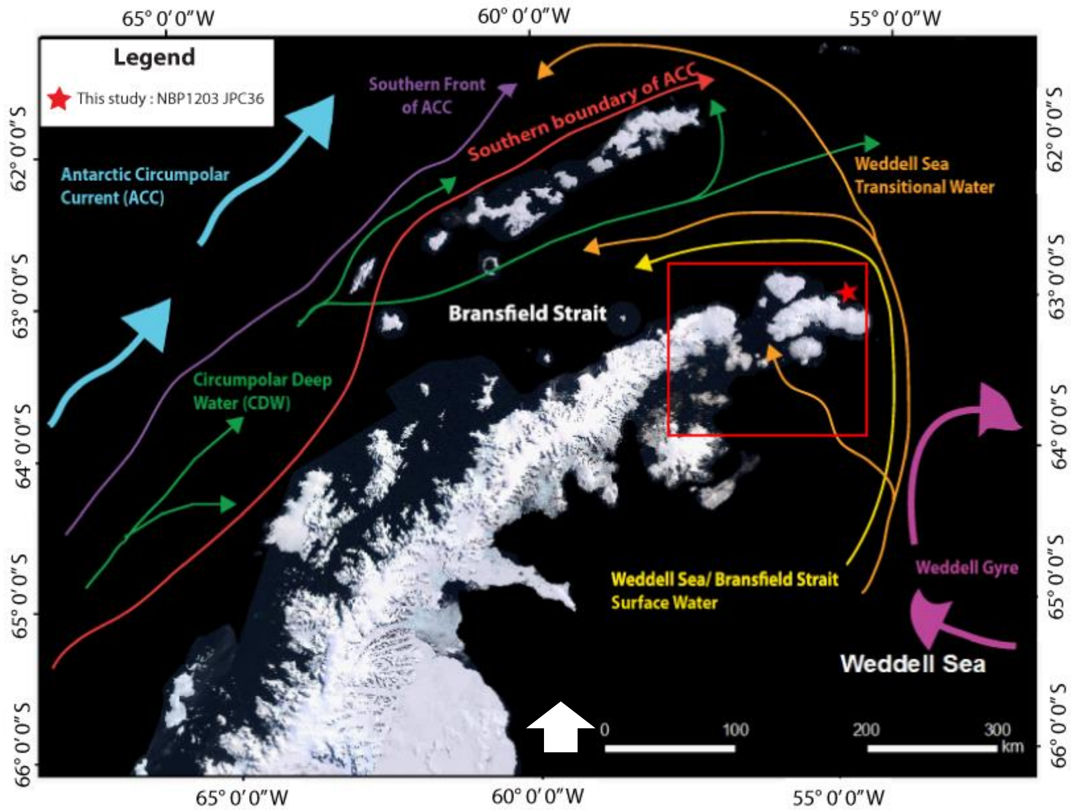

Figure 4: Northern Antarctic Peninsula ocean currents (Tokarczyk, 1987; Ishman and Domack, 1994; Hoffman, 1996; Shevenell and Kennett, 2002; Von Glydenfelt et al., 2002). Red box represents the zoomed in area in Figure 5. Landsat Image Mosaic of Antarctica (LIMA) project images downloaded from http://lima.usgs.gov/access.php.

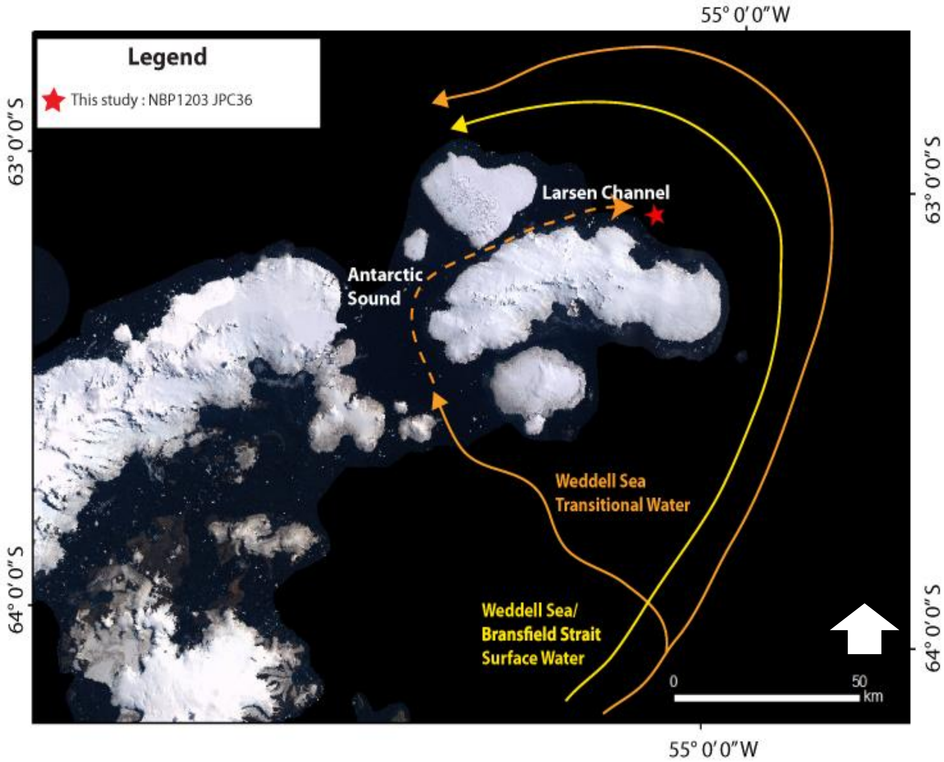

Figure 5: The influence of currents on Perseverance Drift. The Weddell Sea Transitional Current flows through the Antarctic Sound, flows between D'Urville and Joinville Island in the Larsen Channel, and deposits sediment on the continental shelf as a result of slowing velocity (Tokarczyk, 1987; Ishman and Domack, 1994; Hoffman, 1996; Shevenell and Kennett, 2002; Von Glydenfelt et al., 2002). Red star represents location of Perseverance Drift. Landsat Image Mosaic of Antarctica (LIMA) project images downloaded from http://lima.usgs.gov/access.php.

Last Glacial Maximum

During the Last Glacial Maximum (LGM) about 26,000-19,000 cal. yr. BP, global ice sheets reached their maximum extent with some areas reaching the continental shelf break (Heroy and Anderson, 2005; Clark et al., 2009). This was when the Antarctic Peninsula Ice Sheet (APIS) extended to the continental shelf break of the western AP (Figure 6; Anderson et al., 2002; Heroy and Anderson, 2005; 2007). Based on this, the AIS most likely reached the break of the continental shelf on the northern AP and grounded ice covered the Perseverance Drift during this time; however a bathymetry data for the location is sparse. An initial retreat of the ice sheet from the outer continental shelf began around 18,500 cal. yr. BP, and by 5,000 cal. yr. BP, the ice sheet grounding line was on the inner continental shelf or close to its position today (Heroy and Anderson, 2005; Bentley et al., 2014; Ó Cofaigh et al., 2014).

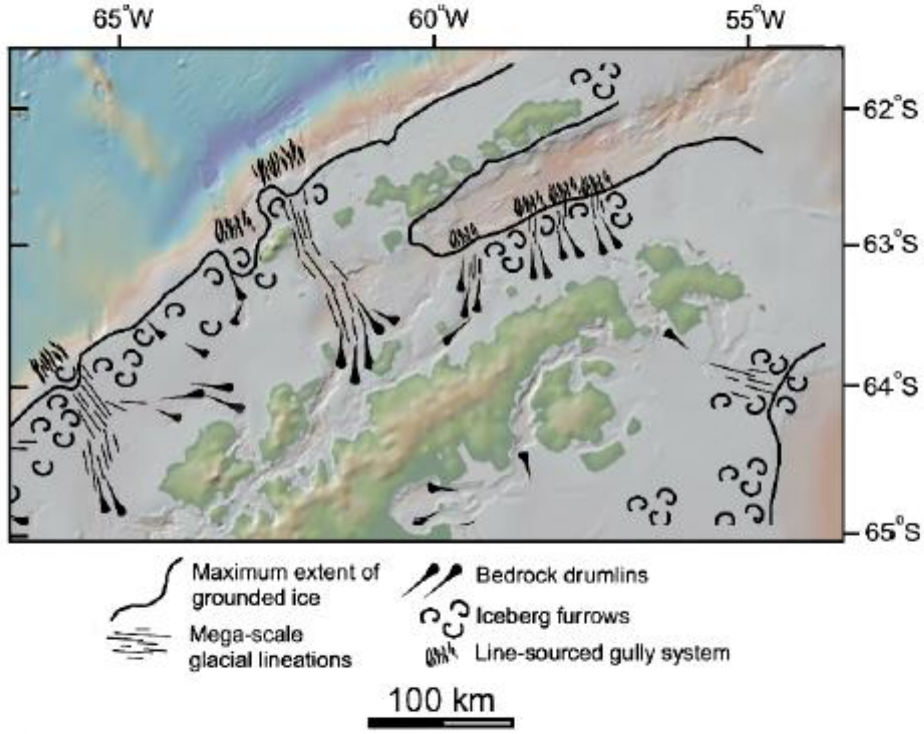

Figure 6: The extent of the grounding zone during the LGM and geomorphic features resulting from ice movement on the continental shelf (Heroy and Anderson, 2005; Modified by Barnard, 2010).

Holocene Climate

A comprehensive review of broad Holocene environmental and paleoclimate change for the Antarctic Peninsula can be found in Bentley et al. (2009). During the Holocene, Bentley et al. (2009) recognize four Holocene warming periods, three Holocene cooling periods, and period of very slow warming (Figure 7).

Climatic event	Age (Cal. yr. BP)
Recent Rapid Warming	100- recent
Little Ice Age	700-150
Medieval Warm Period	1,200-600
Neoglacial	2,500-1,200
Mid-Holocene Warm Period	4,500-2,800
Deglaciation	9,500-4,500
Early Holocene Climatic Optiumum	11,000-9,500

Warm

Slow warming

Cold

Figure 7: Holocene paleoclimate from the early Holocene to present day. Four warm periods, three cold periods, and period of slow warming represent the Antarctic Peninsula climate during the Holocene. These are based Holocene proxy records of marine and terrestrial paleoclimate (adapted from Bentley et al., 2009).

The Early Holocene Climatic Optimum, from 11,000-9,500 cal. yr. BP, is a warm period in the AP as shown by higher diatom abundance and higher coarse-grain material in sediment cores (Domack et al., 2002; Sjunneskog and Taylor, 2002; Taylor and Sjunneskog, 2002). Following the Early Holocene Climatic Optimum, a deglaciation period occurred from 9,500-4,500 cal. yr. BP, and during this time, the AP experienced an asynchronous series of slow warming events throughout the region; however some proxy data shows evidence of some ice shelf reformation (Bentley et al., 2009). The Mid-Holocene Warming Period (MHWP), from 4,500-2,800 cal. yr. BP, is agreed to represent a warm climate across the entire AP and is marked by rapid marine sedimentation, high organic productivity, and an increase in meltwater-derived sedimentation (Shevenell et al., 1996; Taylor et al., 2001; Domack et al., 2003). After the Mid-Holocene Warming Period, the Neoglacial (NEOG) occurred from 2,500-1,200 cal. yr. BP, and evidence for this paleoclimate includes a decrease in the Mass Accumulation Rate (MAR) and diatom abundances correlate with increased sea ice and cold waters (Domack, 2002; Sjunneskog and Taylor, 2002; Taylor and Sjunneskog, 2002). The Medieval Warm Period (MWP), from 1,200-600 cal. yr. BP, in which proxy records are limited to marine cores that show increased productivity peaks and lower magnetic susceptibility signals, which are a signal of warm water (Khim et al., 2002; Domack et al., 2003). The Little Ice Age (LIA), from 700-150 cal. yr. BP, represents a time in the AP with increased sea ice and local glacial advances; however the records of it are erratic due to limited data (Bentley et al., 2009 and references therein). The Recent Rapid Warming period (RRW), from 100 cal. yr. BP to present day, is a result of anthropogenic effects. High resolution marine cores show warm water diatom species, increases in ice rafted debris (IRD), and a high abundance of percent clay resulting from increased flux of meltwater (Domack et al., 2003). To shed light on today's warming temperatures, it is important to study the climate changes leading up to the Medieval Warm Period and the Little Ice Age.

Regional Paleoclimate Studies

The Perseverance Drift has not been studied previously. However, marine sediment cores from the northwestern and northeastern AP have been studied for paleoclimate reconstructions using multiple proxies. Because the locations of previously studied areas are relatively close to the Perseverance Drift, ties can be made to help with interpreting past climate (Figure 8).

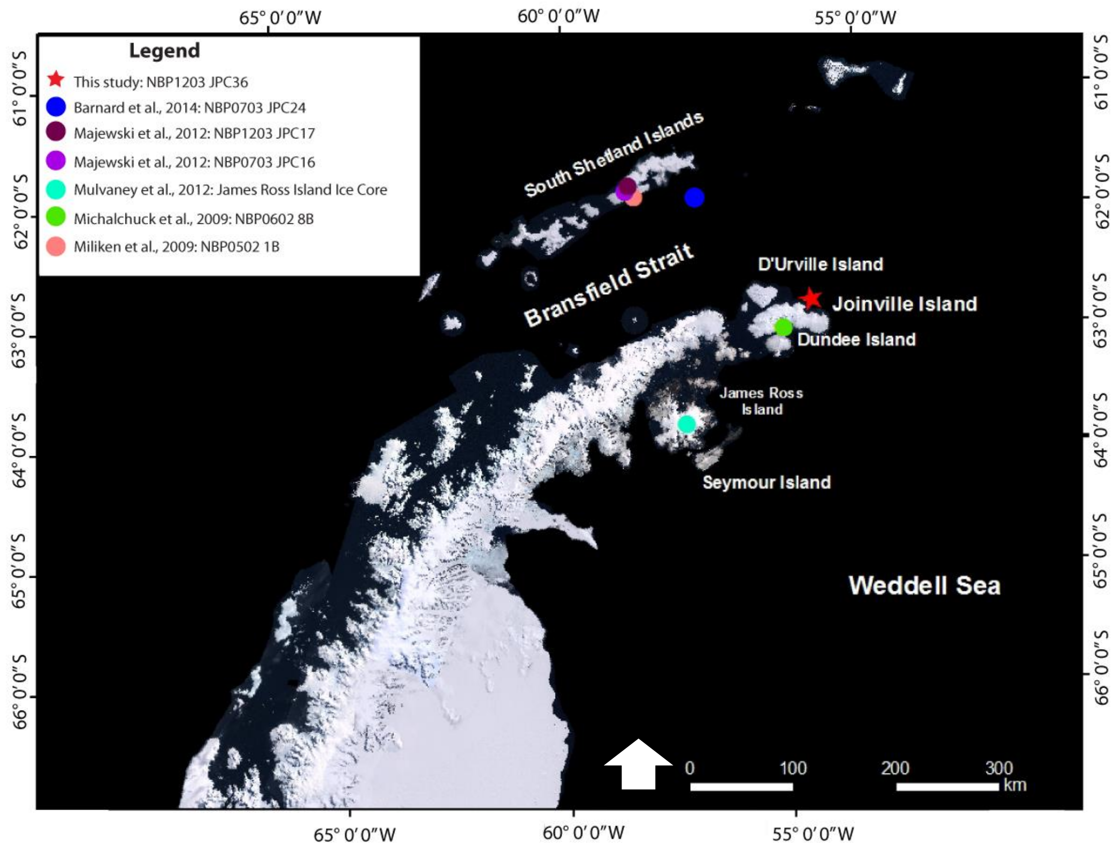

Figure 8: Previously studied areas in the northern AP. Landsat Image Mosaic of Antarctica (LIMA) project images downloaded from http://lima.usgs.gov/access.php.

A sediment core collected from Maxwell Bay in 2005, located in the South Shetland Islands, provides a high resolution climate reconstruction (Milliken et al., 2009). Milliken et al. (2009) used the following proxies: magnetic susceptibility, total organic carbon, carbon and nitrogen isotopic composition, pebble content, grain size, and biogenic silica content. Variations in sea-ice cover occurred from 5,900-2,600 cal. yr. BP representing the Mid-Holocene Warm Period (Rau et al., 1991; Gibson et al., 1999; Villinski et al., 2000). The transition from the Mid-Holocene Warm Period to the Neoglacial occurred at 2,600 cal. yr. BP and can be seen by changes in the nitrogen isotope signature and magnetic susceptibility. The Neoglacial occurs from 2,600-1,100 cal. yr. BP. The Medieval Warm Period is identified to be from 1,100-700 cal. yr. BP and the Little Ice Age from 700-200 cal. yr. BP by changes in magnetic susceptibility and isotopic signatures (Bentley et al., 2009; Milliken et al., 2009).

Two sediment cores collected in 2007, also from Maxwell Bay, South Shetland Islands, were used to help with paleoclimate reconstruction in the region using the following proxies: magnetic susceptibility, grain size, total organic carbon, and benthic foraminifera (Majewski et al., 2012). An increased abundance of planktonic *Neogloboquadrina pachyderma* represents the Mid-Holocene Warm Period with warm, open water conditions from 3,500-2,000 cal. yr. BP. An onset of the Neoglacial is seen from 2,000 cal. yr. BP by a decreased total organic carbon and an increase in the glacier-proximal *Globocassidulina biora*. The Medieval Warm Period is represented by minor decreases in the $\delta^{18}O$ from 900-400 cal. yr. BP. A cooling period representing the Little Ice Age can be seen by changes in magnetic susceptibility from 400 cal. yr. BP to present (Majewski et al., 2012).

A sediment core from the Firth of Tay on the eastern AP was collected in 2006 to use sedimentological proxies to reconstruct a paleoclimate history throughout the Holocene (Michalchuck et al., 2009). The proxies used in this study are: magnetic susceptibility, electric resistivity, porosity, ice-rafted debris content, organic carbon content, nitrogen content, biogenic silica content, and diatom and foraminiferal assemblages. Radiocarbon dates from the core show that the glacier decoupled from the seafloor at 9,400 cal. yr. BP. At 3,500 cal. yr. BP, the transition between the Mid-Holocene Warm Period and the Neoglacial occurred. This can be seen by changes in magnetic susceptibility values and increase in bulk silica accumulation (Michalchuck et al., 2009).

A sediment core was collected from the King George Sub-Basin of the Central Bransfield Basin in the Bransfield Strait in the western AP for a detail sedimentological study to reconstruct Holocene climate change (Barnard et al., 2014). The proxies used in this study were: x-ray analysis, multi-sensor core logger data, and weight percentages along with isotopic values of total organic carbon and nitrogen. The Mid-Holocene Warm Period is from 3,650-2,600 cal. yr. BP as suggested by high abundance of ice-rafted debris and low magnetic susceptibility. The time from 2,600-1,600 cal. yr. BP represents the Neoglacial by lower $\delta^{15}N$ values. A low primary productivity is represented by low $\delta^{15}N$ values (Khim et al., 2005). The Medieval Warm Period, from 1,600-500 cal. yr. BP is represented by abundant, angular pebbles and low magnetic susceptibility values. The Little Ice Age is represented from 500-50 cal. yr. BP by a very low abundance of pebbles relative to other units and a low density (Barnard et al., 2014).

An ice core taken from James Ross Island on the eastern side of the AP reconstructs Holocene climate history using deuterium/hydrogen isotope ratios (Mulvaney et al., 2012). Based on variations in δD, the Mid-Holocene Period is from 9,200-2,500 cal. yr. BP. The Neoglacial is present from 2,500-600 cal. yr. BP. The cooling is interpreted to be a result of the Antarctic Dipole, a climate pattern which contributes warm air to the western AP and cool air to the eastern AP (Renwick et al., 2005; Ding et al., 2011; Mulvaney et al., 2012). A warming period is present from 600 cal. yr. BP to present. Having these data on the eastern side of the AP, in addition to the data on the western side, allows for a better late Holocene paleoclimate reconstruction.

Sediment Drift Deposits

Sediment drift deposits are thick sequences of sediment deposited by bottom water currents transporting sediment on the seafloor (Harris et al., 2001). Based on seismic profiles, they are characterized by a mound-like geometry in which stratified units drape over an underlying bedrock surface (Harris et al., 2001). These deposits are composed mainly of finely laminated, fine-grained diatomaceous mud deposited after the LGM (Camerlenghi et al., 2001). They are deposited after the deceleration of flow, which results in a gyre or eddy allowing for a drift's deposition (Harris et al., 1999). They have been recognized as good paleoclimate indicators because of their low energy of deposition and high sedimentation rate (Domack et al., 2001). These deposits have been found in deep sea settings all around the world including the northern Atlantic Ocean, but only recently they have been found on the Antarctic continental shelf (Harris et al., 1999; Faugeres et al., 1999). The known drift deposits in the northern AP are: the Vega Drift, Andvord Drift, Palmer Drift, Perseverance Drift, and Scholleart Drift (Harris et al., 1999; Wright, 2000; Domack et al., 2001; Backman and Domack, 2003; Domack et al., 2007).

Grain size

Currents carry sediment sourced from a variety of different locations and deposit it in a sediment drift once the current slows (Harris et al., 1999). Although sediment drifts are composed mainly of finely laminated, fine-grained diatomaceous mud, they also contain pebbles (from glaciers and sea ice), glacial silt (from meltwater), and silt-sized phytoplankton detritus (Mashiotta, 1992; Domack and Ishman, 1993; Camerlenghi et al., 2001). Therefore, mud-sized particles dominate these deposits; there is a medley of grain sizes present in sediment drifts.

Grain size is a useful proxy for reconstructing paleoclimate. Ice-rafting releases sediment as icebergs calve and melt (MacAyeal, 1992). In warm, open marine conditions, calved icebergs have a direct contribution to seafloor sedimentation by melting and releasing a range of grain sizes, including coarse-grained particles, such as gravel and sand, from their matrix (Figure 9; Hillenbrand et al., 2009; Barnard et al., 2014). Residual glacial marine sediments are sourced from these icebergs and ice shelves, and once settled on the seafloor, they can be winnowed by strong bottom currents leaving behind a sandy and gravelly lag (Figure 9; Anderson et al., 1980; Wellner et al., 2011). Currents also contribute particles of various sizes (Figure 9).

The melting of seasonal sea ice allows for the delivery of aeolian sediment onto the seafloor. Based on the proximity to exposed land, sea-ice aeolian sediment is a major contributor of clay-sized to well-sorted fine-grained sand to the modern continental shelf in regions of high latitude (Figure 9; Darby et al., 1974; Barrett et al., 1983; Anderson et al., 1984; Hughes and Krissek, 1984; Bartek and Anderson, 1991; Chewings et al., 2014). Strong kabatic winds are always prominent along Antarctica's coast (Parish and Bromwich, 1998). Clay-, silt-, and sand-sized aeolian grains can also be transported directly to the seafloor by strong, coastal winds in (Figure 9; Laluraj et al., 2014).

High silt values can be a result of proximal glacial melt or ice rafting influences (Warner and Domack, 2001). The diatom species, *Chaetoceros,* can also contribute to the silt-sized content. *Chaetoceros* forms resting spores when unfavorable growth conditions, including temperature stress and nutrient limitation after blooms, arise (Armand et al., 2005). The size of *Chaetoceros* resting spores are the same as size as high, medium, and low-sized silt (Warner and Domack, 2001). If there is a high abundance of silt in a deposit known to have *Chaetoceros*, then the depositional environment is one with more biogenic control and less permanent sea ice (Figure 9; Warner and Domack, 2001).

Studies have shown that iron- rich terrigenous sediment melted from sea-ice triggers and allows for seasonal, large-scale phytoplankton blooms (Sedwick and DiTullio, 1997; Sedwick et al., 2000; Lannuzel et al., 2007; Raiswell et al., 2008; Atkins and Dunbar, 2009). A high volume of clay-sized biogenic sediment on the seafloor is produced from these events (Figure 9; Dunbar et al., 1985, 1989). High clay percentages are also present in the form of clay minerals, which are terrigenous in origin (Bentley et al., 2009).

Mechanism	Clay	Silt	Sand	Granule	Pebble
Iceberg- rafting	●	●	●	●	●
Current winnowing			●	●	●
Currents	●	●			
Aeolian delivery to sea ice	●	●	●		
Direct delivery by aeolian processes	●	●	●		
Biogenic processes	●	●			

Figure 9: Various grain sizes and their corresponding delivery mechanism.

Grain shape

Grain-shape studies have been conducted to determine the transport history mechanism and to identify the source of a sediment in multiple environments (Ehrlich and Weinberg, 1970; Ehrlich et al., 1980; Mazzullo and Ritter, 1991; Murillo-Jimenez et al., 2007; Livsey et al., 2013). Quartz grain roughness can reflect whether the dominant mode of transport was glacial, which will result in rougher grains, or nonglacial that will result in smoother grains (Haines and Mazzullo, 1988; Livsey et al., 2013). In periods of deglaciation, smoother grains are expected because of the increased effect of subaqueous current activity and aeolian transport allowing for grain-to-grain contact (Livsey et al., 2013).

Grain texture

Using a scanning electron microscope, studies of grain texture have been done to help determine the transport history (Mahaney et al., 1995; Mahaney, 2002; Asthana et al., 2009; Madhavaraju et al., 2009; Sweet and Soreghan, 2010; Kirshner and Anderson, 2011). After transportation, quartz grains record features left behind by glaciers and wind or water medium, therefore providing a dependable record of climate changes in Antarctica (Mahaney, 2002; Kirshner and Anderson, 2011). Features such as: fracture faces, subparallel linear fractures, conchoidal fractures, arc shaped steps, linear steps, and sharp angular features are classified as polygenetic in origin (Sweet and Soreghan, 2010; Kirshner and Anderson, 2011). Sustained high impact features, which are glacial in origin, include: high relief surfaces, blocky breakage, crescentic gouges, straight grooves, curved grooves, and deep troughs (Sharp and Gomez, 1986; Asthana et al., 2009; Sweet and Soreghan, 2010; Kirshner and Anderson, 2011). Aeolian features include: mechanically upturned plates, v-shaped collision pits, edge rounding, dissolution etching, weathered surfaces, dish-shaped concavities, and meandering ridges (Asthana et al., 2009; Madhavaraju et al., 2009; Sweet and Soreghan, 2010; Kirshner and Anderson, 2011). Quartz grains influenced by currents will exhibit a smooth texture as well as edge rounding (Anderson et al., 2011; Wellner et al., 2011). By studying the relative abundances of these microtextures, a reconstruction of the paleoclimate can be assessed.

The Antarctic Silica Budget

Dissolved silica (SiO_2) in the world's oceans is used by silicoflagellates, sponges, radiolarians, and diatoms to build their skeletons. Within the upper 100m of the water column, a large portion of the biogenic silica production is recycled via dissolution and reused by organisms (Nelson and Gordon, 1982; Nelson et al., 1991, 1995; Treguer et al., 1995; Nelson and Brzezinski, 1997). Eventually, some reaches the seafloor and this final deposit represents about 25-50% of the silica that enters the Antarctic marine environment (DeMaster et al., 1991; Treguer et al., 1995; DeMaster et al., 2002; Buffen et al., 2007). The biogenic silica on the seafloor dissolves, and when concentrations of silica are large enough, authigenic quartz will precipitate (Füchtbauer, 1988).

Ikaite

Ikaite is a hydrous polymorph of calcium carbonate and is a precursor to glendonite (Suess et al., 1982). It is only stable at near-freezing temperatures (Selleck et al., 2011; Lu et al., 2012). Domack et al. (2007) proposed that the contribution of very cold waters coming from the Weddell Sea aid in the formation of the mineral by maintaining ikaite's stability field of 6°C. High regional productivity results in high organic content in muds, which may allow for the formation of ikaite (Domack et al., 2007). Therefore, cold Weddell Sea water and high organic content, along with high pore water alkalinity and high levels of dissolved phosphate, contribute to ikaite's formation (Bischoff et al., 1993; Domack et al., 2007). Greinert and Derkachrv (2004) suggest that the high levels of dissolved phosphate stop carbonate phases from precipitating and allow ikaite to form.

Ikaite tends to form around the sulfate methane transition (Lu et al., 2012). At this transition, 2-4m, the porewater profiles also show a high calcium concentration and high dissolved organic concentration. At this boundary, rapid carbonate precipitation occurs with the removal of dissolved calcium. Ikaite growth below 2-4m is unlikely because calcium concentration is low below 5m. Therefore, the age of an ikaite crystal is younger than the surrounding sediments by the amount of time it took for the deposition of 2-4m of sediment (Lu et al., 2012).

Ikaite is a very useful tool because it is an accurate recorder of $\delta^{18}O$ of seawater, which helps to reconstruct past $\delta^{18}O$ of porewater to aid in paleoclimate analysis (Rickaby et al., 2006; Lu et al., 2012). In the northern AP, ikaite has been found in the Vega Drift, Firth of Tay, Bransfield Basin, and now Perseverance Drift (Figure 10; Zhou et al., in press; Domack et al., 2007). The mineral has been found in sediment cores from non-glacial, but still cold and deep, waters of the Zaire Fan, located west of the Congo, and the Argentine Basin, located east of Argentina. Again, this proves that temperature alone cannot be the only parameter for ikaite formation (Zhou et al., in press). Zhou et al. (in press) propose phosphate recycling to be the mechanism responsible for the ikaite's formation, because geochemical data from the ikaite sites in the Atlantic Ocean and Antarctica indicate a high phosphate concentration in the sites. According to this hypothesis, the pore water phosphate concentration in areas containing ikaite is high because crustal atmospheric dust, rich in iron, blows from land, settles on the seafloor, and, during iron reduction, releases phosphate forming the mineral (Slomp et al., 1996; McConnell et al., 2007; Zhou et al., in press).

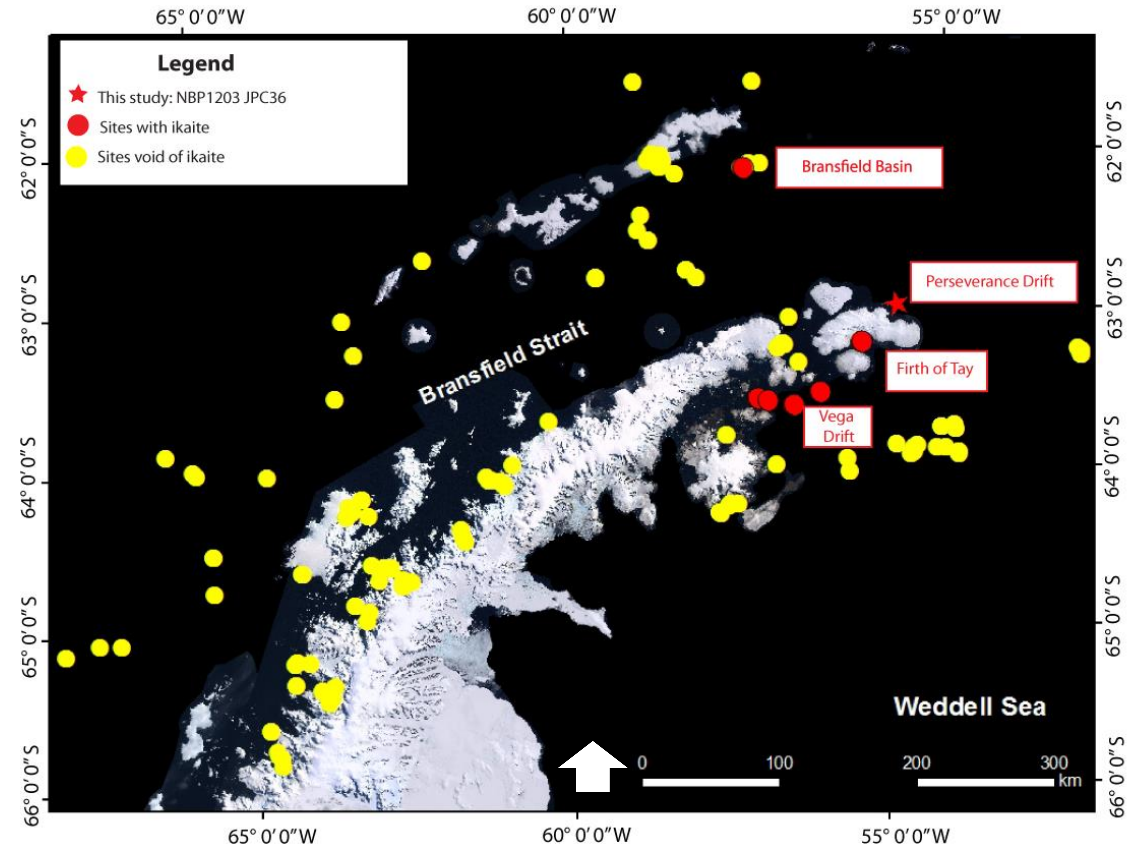

Figure 10: Distribution of ikaite throughout the AP. Out of hundreds of cores collected, only 7 contain the mineral. Many more cores without ikaite are not shown. Landsat Image Mosaic of Antarctica (LIMA) project images downloaded from http://lima.usgs.gov/access.php.

Diatoms

Chaetoceros spp. are associated with large spring blooms and high productivity given ample nutrients in a system after sea-ice breakup at ice edge (Leventer et al., 1996; Leventer, 1998; Sjunneskog and Taylor, 2002). They are present as spores or vegetative cells. *Chaetoceros* forms resting spores form during conditions of stress, such as temperature change and nutrient limitation, in order to survive (Armand et al., 2005).

Fragilariopsos curta spp. prefers to live in water with very cold sea-surface temperatures and usually within sea ice and at the sea-ice edge (Fryxell et al., 1989; Leventer et al., 1998; Cunningham et al., 1999). *Fragilariopsos cylindrus* spp. also prefers to live in a sea-ice-rich environment and conditions with melting ice (Leventer et al., 1998).

Porosira glacialis spp. and *Thalassiosira antarctica* spp. are also classified as sea-ice diatom, as they are abundant near the sea-ice edge (Pike et al., 2009). However, *Porosira glacialis* prefers conditions that are slightly cooler and icier than *Thalassiosira antarctica* (Pike et al., 2009). *Thalassiosira antarctica's* morphology is dependent on water temperature and grows larger in warm, open water settings (Villareal and Fryxell, 1983; Cooper and Leventer, 2005).

Two other common Antarctic diatoms include *Fragilariopsos kerguelensis* spp. and *Cocconeis spp. Fragilariopsos kerguelensis* spp. are considered open marine diatoms (Crosta et al., 2005). They occur in warm waters away from the ice edge (Leventer et al., 1998). *Cocconeis spp.* represent epiphytic diatoms. They use sea ice as a substrate and can be classifies as benthic diatoms (Al-Handel et al., 2010; Majewska et al., 2013).

These diatoms live in a nearshore, well-lit environment attached to microalgae (Vadman, 2014).

Study Area

Figure 4 and Figure 5 both show location of the Perseverance Drift in the northeastern AP in an open marine environment. A 3.5 kHz CHIRP profile of the Perseverance Drift shows the drift deposit's mound-shape geometry (Figure 11). The deposit is 100m thick and the jumbo piston core extends 24m.

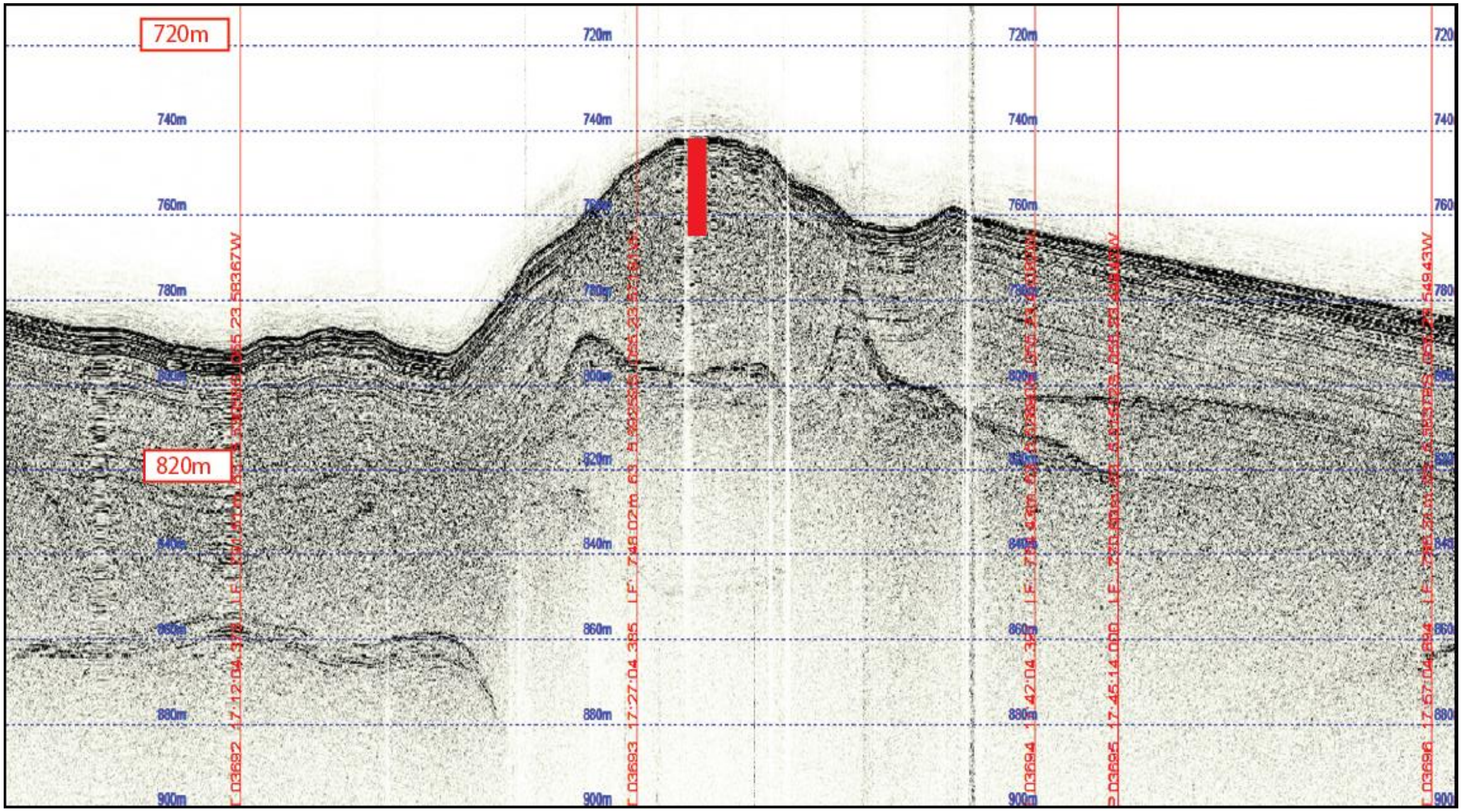

Figure 11: A 3.5 kHz CHIRP profile of the Perseverance Drift. Red polygon represents the core taken at the site.

Due to its northerly location in the AP, some islands surrounding the Perseverance Drift have ice-free areas (Figure 12). This allows for the high input of terrigenous material to the site by aeolian processes through the melting of sea ice and direct transport from land to sea (Figure 13).

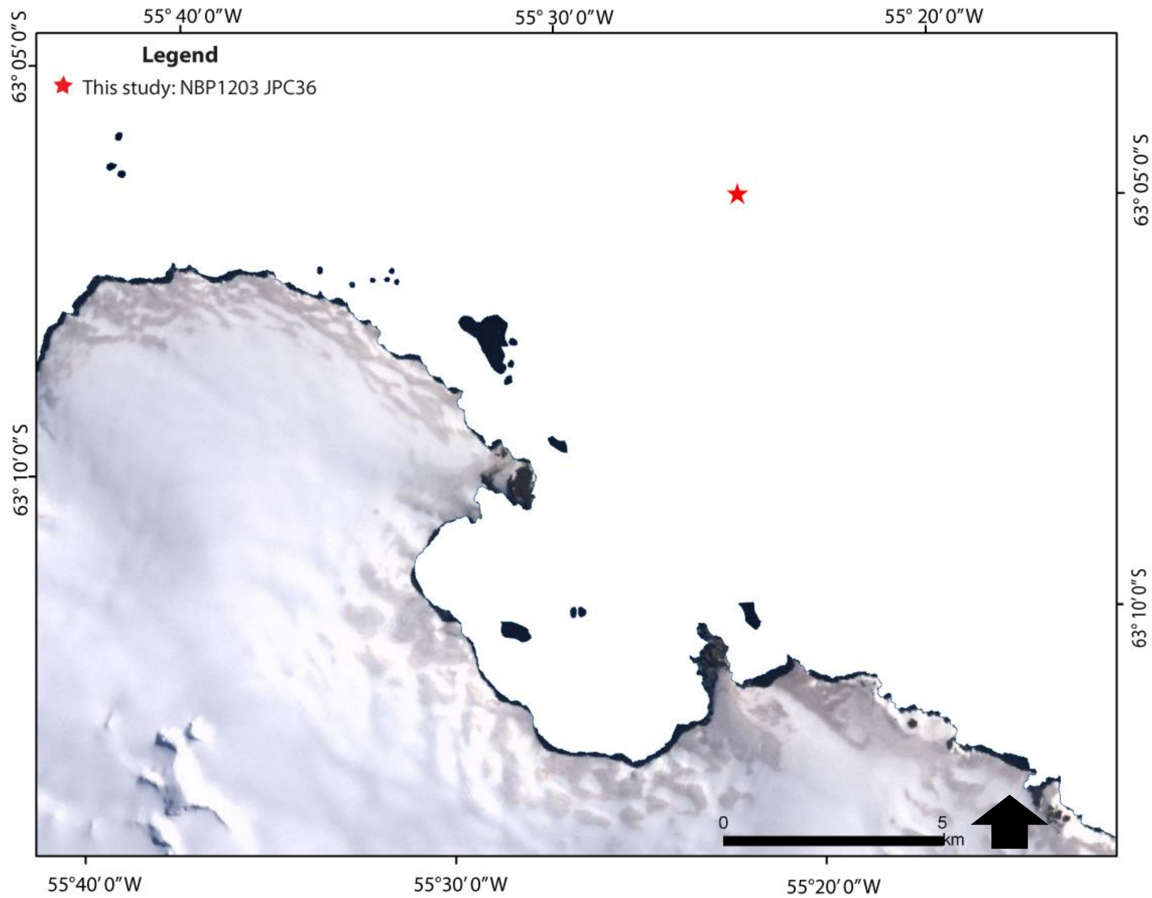

Figure 12: The Perseverance Drift in relation to exposed land on the northernmost part of Joinville Island. Exposed land is represented by the dark grey color. Landsat Image Mosaic of Antarctica (LIMA) Project images downloaded from http://lima.usgs.gov/access.php.

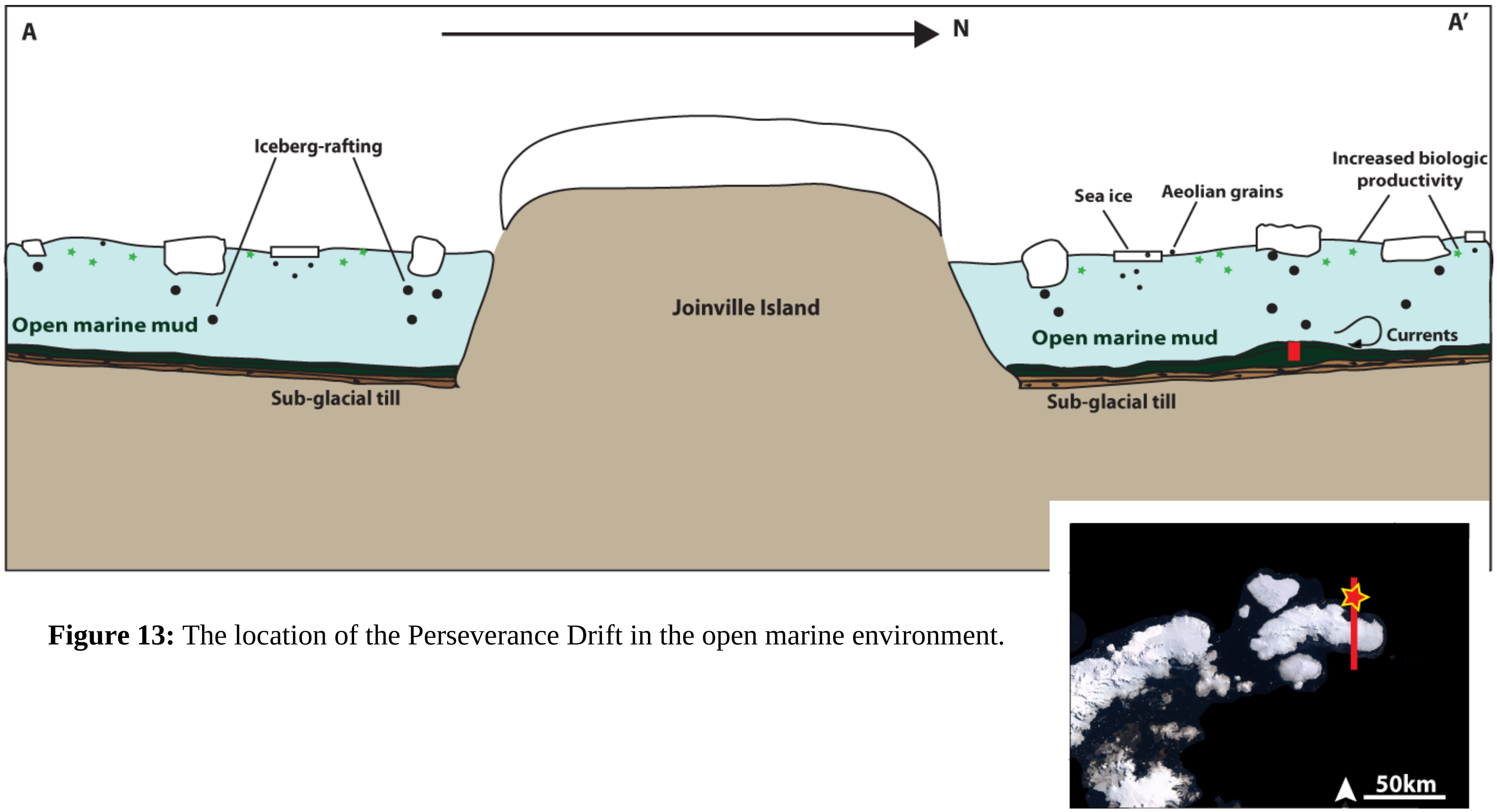

Figure 13: The location of the Perseverance Drift in the open marine environment.

Methods

The data used for this study were collected in the austral summer on the third cruise of 2012 on the RV/IB *Nathaniel B. Palmer* as part of the LARISSA (LARsen Ice Shelf System Antarctica) project. Sediment core data was collected at the Perseverance Drift, AP. Geophysical data, including 3.5 kHz CHIRP data and multi-beam swath bathymetry data were also collected at the site.

Sediment Core Data

A jumbo piston core (JPC36) and a jumbo trigger core (JTC36), were collected at the Perseverance Drift, AP at 63° 05.34 S, 55° 23.92 W. A jumbo kasten core, NBP1203 JKC36, was collected at 63° 05.35 S, 55° 24.67 W, ~600m to the west of JPC36. NBP1203 JPC36, NBP1203 JTC36, and NBP1203 JKC36 measure 24m, 1.2m, and 1.81m, respectively. NBP1203 JPC36 and NBP1203 JTC36 were taken at a water depth of 806m. Because NBP1203 JTC36 samples the sediment-water interface and NBP1203 JPC36 does not, it is necessary to combine the two into one long core of 25.81m. Throughout this paper, this core will continue to be called NBP1203 JPC36.

JKC36 was opened at sea and described onboard. NBP1203 JPC36 was opened at the Antarctic Research Facility (ARF) at Florida State University and described at ARF. The cores were described by colleagues from LARISSA. Initial visual descriptions included color, sedimentary structures, and grain size. A lithologic log was created from this information. Any large ikaite crystals were taken out and placed in a freezer to avoid deterioration. The cores were then sent to ARF to be split with one half designated for the archives and the other for study. About 5cc of sediment from JPC36 was bagged every 5cm down-core and sent to The University of Houston for this study.

X-rays were taken at ARF to look for IRD and various sedimentary structures. Magnetic susceptibility every 5cm down-core was measured using a Geotek multi-sensor logger at ARF.

Grain Size

A Malvern Mastersizer 2000 LPSA at Rice University, Houston, Texas and a CILAS LPSA at the University of Houston, Houston, Texas were used to measure grain size. Only 17 intervals were measured for grain size using the CILAS LPSA, while the remaining 465 intervals were measured using the Malvern Mastersizer LPSA. Sediment was sampled for 1cm intervals every 5cm down-core. About 1cc of sediment was prepared for grain size analysis. The preparation process included: adding the ~1cc sample to ~100mL of de-ionized water, adding a small amount sodium hexametaphosphate to allow for the deflocculation of clay, stirring the sample, covering it, and letting it sit overnight. Before introducing the sample into the Malvern Mastersizer 2000 LPSA or CILAS LPSA, a magnetic stirrer was used and a pipette was used to sample from the center of the whirlpool, on the wall of the beaker, in order to avoid bias in grain size.

After the grain-size statistics were produced, grain-size classification was conducted using the Wentworth grain-size classification (Wentworth, 1922). The classification included: clay-sized particles as < 3.9µm, very fine silt-sized particles as 3.9-8µm, fine silt-sized particles as 8-16µm, medium silt-sized particles as 16-3µm, 31-

63μm as coarse silt-sized particles, and sand-sized particles as > 63μm. Pebbles were classified as 2-4mm and were counted every 5cm in x-rays.

Grain Shape

A CILAS LPSA at the University of Houston was used to analyze grain-shape. Sixty-nine intervals were sampled for grain-shape analysis. All 15 intervals of ikaite were also sampled. To prepare the samples for grain-shape analysis, ~3cc of sediment was placed in ~100mL of water. A small amount sodium hexametaphosphate was added to deflocculate clay in the sample. The samples were stirred and covered overnight. They were then sieved at 63μm. A magnetic stirrer was used to stir up the sediment, and a pipette was used to sample along the wall of the beaker, in the center of the whirlpool. The sample was then introduced into the CILAS LPSA. For each interval, an Excel sheet with shape statistics was produced along with a JPEG of every particle.

Grain shape was measured using Fourier analysis (Ehrlich and Weinberg, 1970). Higher-order harmonics were used in order to describe weathering and transport history (Ehlrich et al., 1980; Murillo-Jimenez et al., 2007; Livsey et al., 2013). Like Livsey et al. (2013), using the harmonic range of 17-21, a dimensionless roughness coefficient (Rc) was use to quantify grain shape. In this study, the equation used for finding the Rc is $Rc_{a\text{-}b}= \sqrt{0.5 \sum R_n^2}$. The harmonic range is represented by *a-b* and is 17-21. R_n is the nth harmonic coefficient.

MORPHEO, a Matlab code, was used to output Fourier harmonics by using Fast Fourier Transform (FFT) (Charpentier et al., 2013). For MORPHEO to be able to detect a particle, a JPEG of a quartz grain entered into the code must have its resolution increased by 360 DPI in Adobe Photoshop. With this step, the perimeter of a particle is always greater than 500 pixels. Therefore, this provides a detailed outline of the grain allowing for MORPHEO to make an accurate interpolation. The physical length scale resolved with harmonics 17-21 is also dependent on the resolution of the JPEG, and if the resolution is increased to 360 DPI, then errors in interpolation are small (Charpentier et al., 2013).

For each interval sampled, a minimum of 30 JPEGs of > 63μm quartz particles were run through MORPHEO. As MORPHEO analyzed each grain, the outline of each grain was observed, and if the outline had gaps in it, the grain was removed from analysis. The final roughness coefficient for the interval is the mean of the 5 values from harmonics 17-21.

Grain Texture

A scanning electron microscope (SEM) at the University of Houston, Houston, Texas was used for grain texture analysis. Forty-four intervals were selected for textural analysis, including the 15 ikaite intervals. To prepare the samples for analysis, ~2cc of sediment was placed in ~100mL of water. A small amount of sodium hexametaphosphate was added into the beaker to allow for the deflocculation of clay. The beaker was covered and left overnight. The sediment was then sieved at > 63μm and oven-dried. A minimum of 10 quartz grains were picked under a reflected light microscope and placed on carbon tape on a carbon disk. The mounted grains were then carbon coated using the Ladd Vacuum Evaporator at the University of Houston with 30μm of carbon.

Microtextures were identified based on standard criteria and comparison with published examples (Pittman, 1972; Krinsley, 1971; Sharp and Gomez, 1986; Mahaney, 1995; Mahaney, 2002; Asthana et al., 2009; Madhavaraju et al., 2009; Narayana et al., 2010; Sweet and Soreghan, 2010; Anderson et al., 2011; Kirshner and Anderson, 2011; Wellner et al., 2011). Microtextures were classified as high, medium, and low relative abundance. Microtextures in each interval were tallied based on these abundances and represented on a bar graph with their respective transport history. Energy Dispersive Spectroscopy (EDS) was completed on ikaite crystals and selected grains.

Diatom Data

Diatom data were provided by Kara Vadman and Amy Leventer from Colgate University in Hamilton, New York. Every 50cm in JPC36, quantitative diatom slides were created and were counted for total percentage *Chaetoceros* and total assemblage.

Chronology Data

Radiocarbon dating of carbonate material in the core was provided by Eugene Domack from the University of South Florida. Samples were analyzed at Woods Hole Oceanographic Institute. The dating method used for the chronology data in this study is ^{14}C absolute dating of shell material from NBP1203 JPC36 and NBP1203 JKC36. Radiocarbon dating in Antarctica has some complications because the waters have unusually low ^{14}C (Maddison et al., 2005). Previous studies have yielded anomalously old ^{14}C dates for living forams, indicating the importance of a reservoir correction for carbonate samples (Andrews et al., 1999; Harris, 2000; Pudsey and Evans, 2001). These dates were corrected for the reservoir effect by the value of 1,260 years (Domack et al., 2001).

Data and Results

Sediment Core Data

The core analysis methods conducted on NBP1203 JPC36 and JTC36 include: lithological descriptions, sediment facies, grain size, x-ray, pebble count, ikaite data, grain shape, grain texture, diatom abundance, magnetic susceptibility, and density. Together, NBP1203 JPC36 and JTC36 are 25.81m long and, as mentioned in the methods section of this paper, they will be referred to as NBP1203 JPC36.

Lithological Description:

NBP1203 JPC36 consists of alternating laminations of diatomaceous mud and ooze, which is olive green to black and grey in color. There is fine-grained sand dispersed throughout the core. There are scattered pebbles ranging in size from 2-4mm in diameter. Calcareous shells begin to appear at 4.38m and continue down-core. Because of the rich biogenic content of NBP1203 JPC36, gas was released upon recovery. The degassing process is likely responsible for the empty intervals down-core.

Sediment Facies:

The core is rather homogeneous throughout. However, it shows some color variation and some grain-size differences. It was split into four sediment facies: (1) black to grey sandy diatomaceous mud (≥ 20% sand), (2) olive-green sandy diatomaceous mud (≥ 20% sand), (3) black to grey diatomaceous mud, and (4) olive-green diatomaceous mud (Figure 14). In this study, ≥ 20% sand was chosen as the cutoff between high sand abundance and low sand abundance. Sediments with a high biogenic component are green in color, while sediments with a high terrigenous component tend to be grey to black in color.

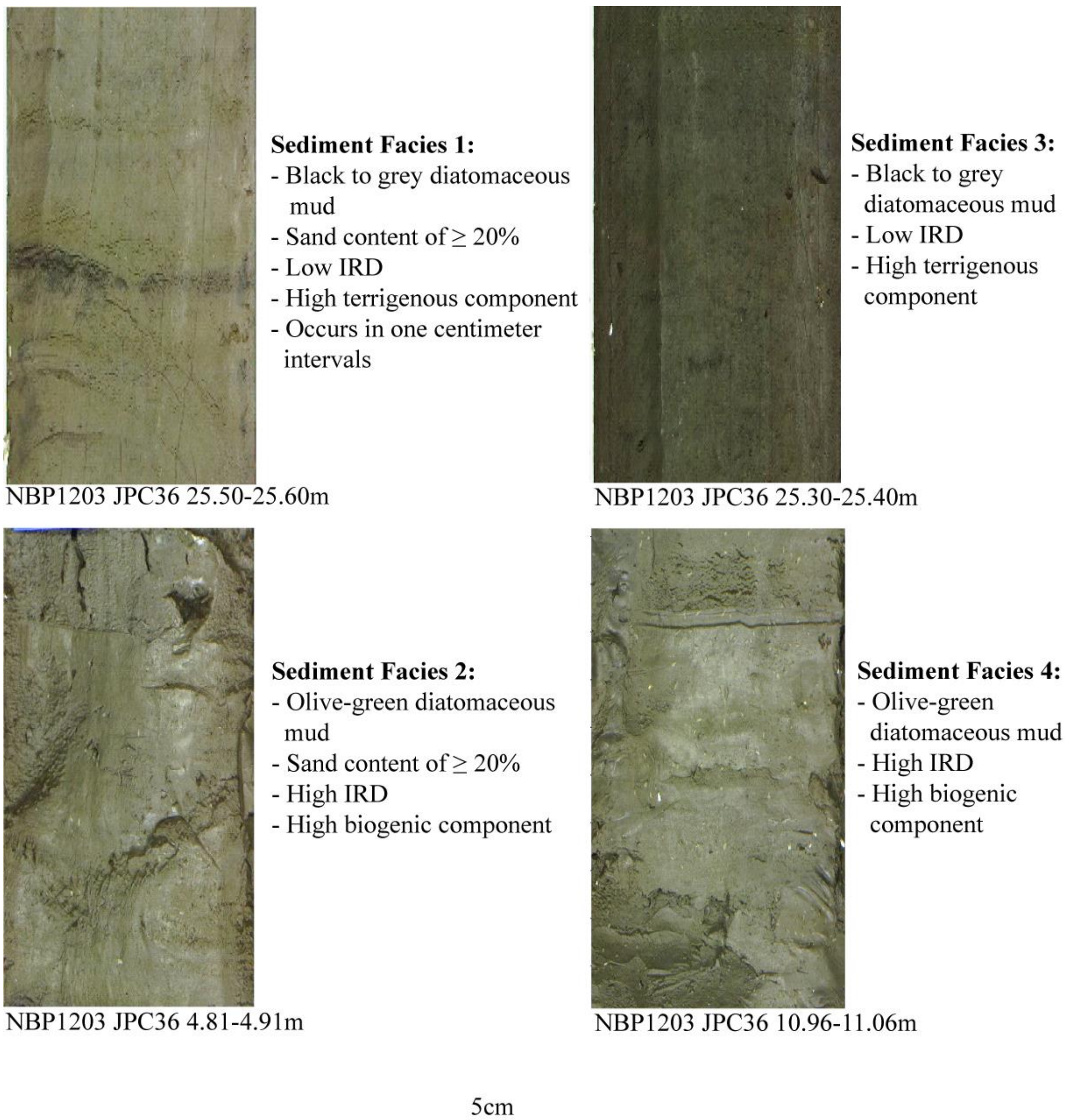

Figure 14: The physical characteristics of the four sediment facies defined for this study. Images were adjusted in Adobe Photoshop for better contrast.

Sediment Facies 1:

Sediment Facies 1 is composed of black to grey diatomaceous sandy mud with sand abundance at ≥ 20% (Figure 15). Grain size analysis shows an average of 22% sand, 65% silt, and 13% clay. This facies occurs in thin, one centimeter intervals.

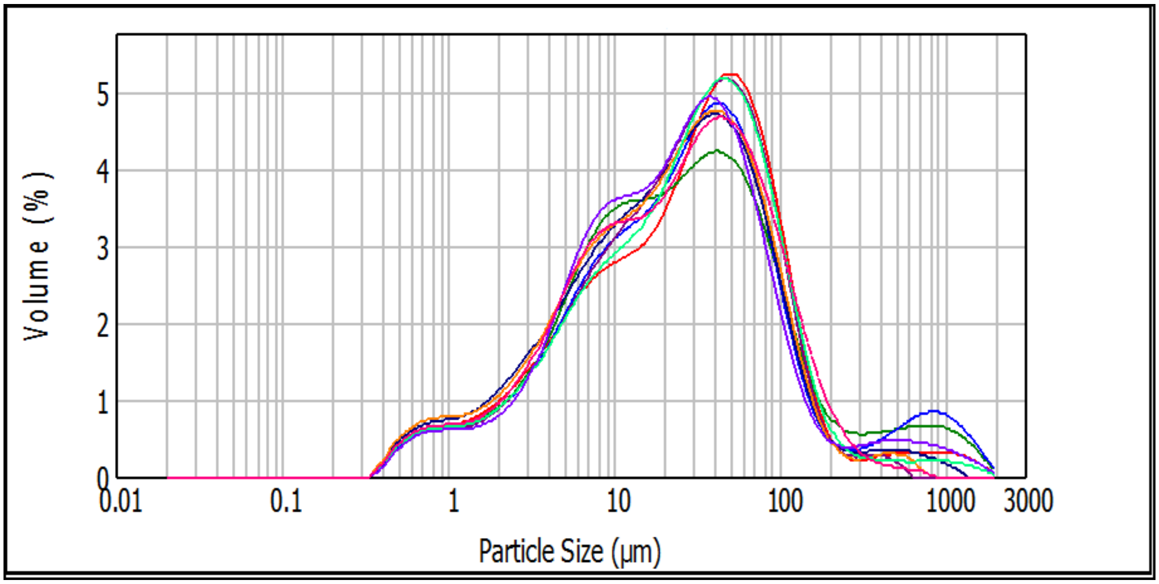

Figure 15: Grain size distribution for Sediment Facies 1. Each colored line is representative of a 1cm interval in NBP1203 JPC36.

Sediment Facies 2:

Sediment Facies 2 is composed of olive-green diatomaceous sandy mud with a sand abundance at ≥ 20%. The sand component averages to 21%, the silt component to 66%, and the clay component to 13% (Figure 16).

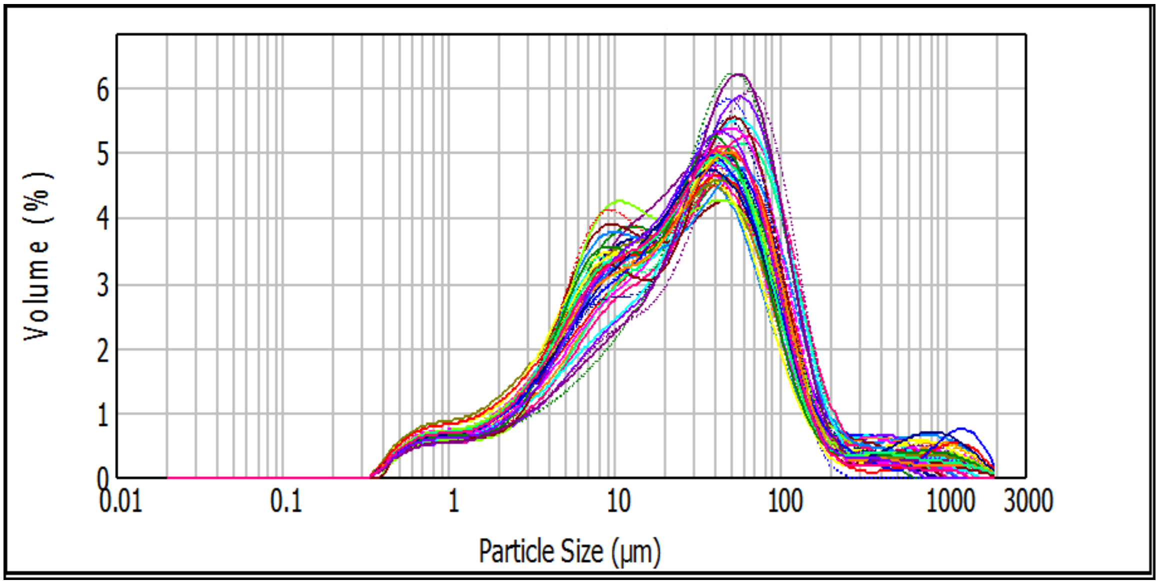

Figure 16: Grain size distribution for Sediment Facies 2. Each colored line is representative of a 1cm interval in NBP1203 JPC36.

Sediment Facies 3:

Sediment Facies 3 is composed of black to grey diatomaceous mud. Mean grain sizes include: 12% sand, 73% silt, and 15% clay (Figure 17). This facies is characterized by a low sand percentage.

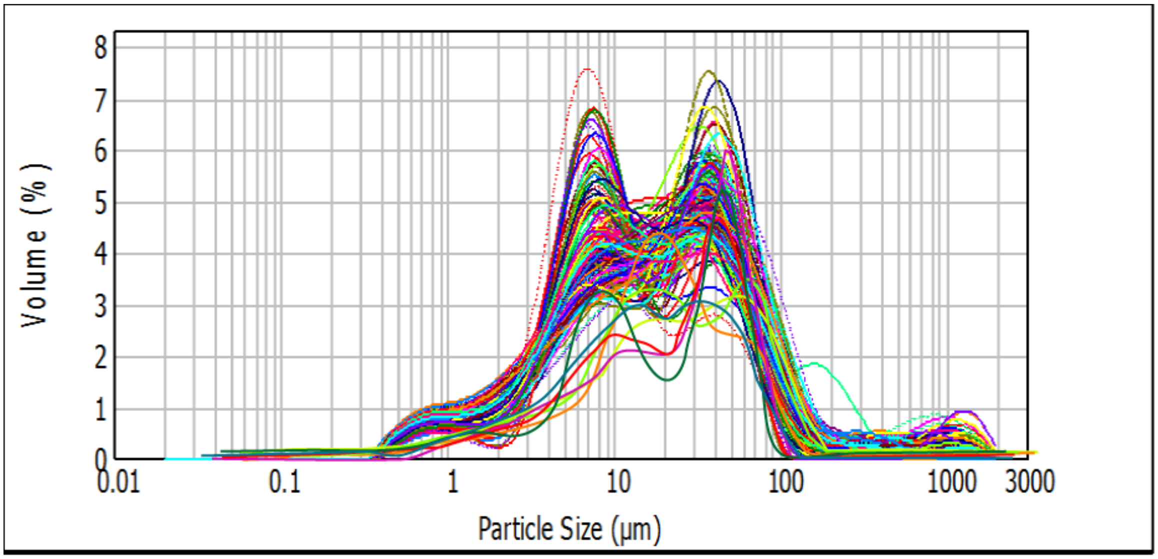

Figure 17: Grain size distribution for Sediment Facies 3. Each colored line is representative of a 1cm interval in NBP1203 JPC36.

Sediment Facies 4:

Sediment Facies 4 is composed of olive-green diatomaceous mud. The sand component is 14%, the silt component is 72%, and the clay component is 14% (Figure 18). This facies is characterized by a low sand percentage.

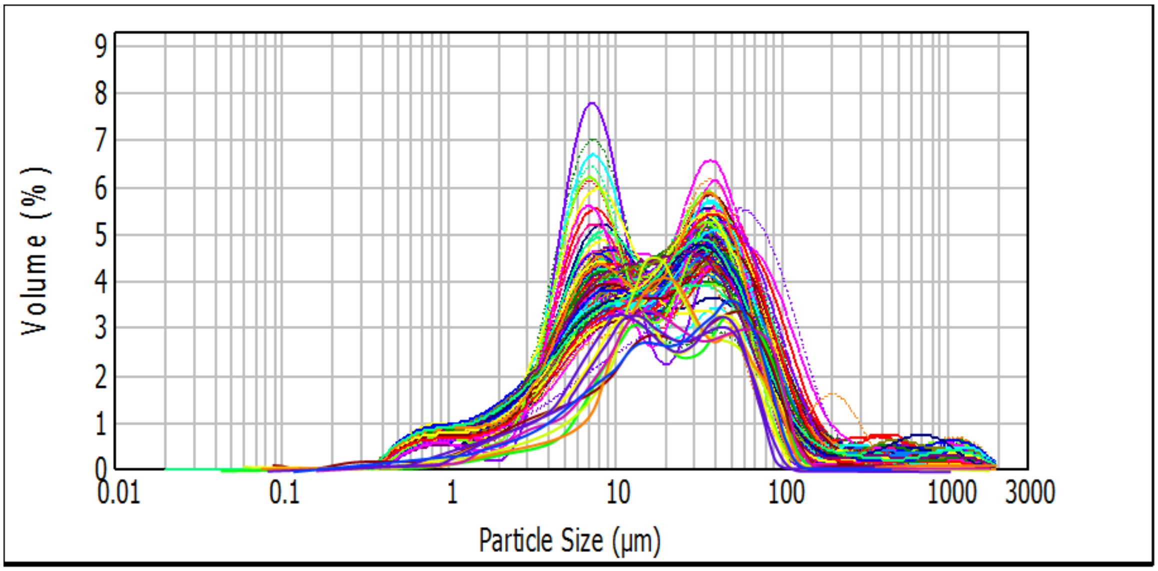

Figure 18: Grain size distribution for Sediment Facies 4. Each colored line is representative of a 1cm interval in NBP1203 JPC36.

It is important to consider the contribution of biogenic versus detrital grains to the site. *Chaetoceros* spores are silt-sized and account for a significant biogenic contribution in Antarctic marine sediments (Warner and Domack, 2001). To consider only the terrigenous input into the Perseverance Drift, the diatom fraction of the sediment would have needed to be removed. This was not completed, therefore both the terrigenous and biogenic contribution were analyzed in the study. Previous studies have also used both fractions to study glacial sediments (Milliken et al., 2009; Michalchuck et al., 2009; Barnard et al., 2014).

To quantify the average abundance of a specific grain size, an average of the percent volume was found. Coarse silt represents the highest percent volume in NBP1203 JPC36 with an average of 20%. Clay and sand have an equal average percent volume in the core of 14%. Very fine silt represents 15%, fine silt represents 18%, and medium silt represents 19% of the deposit.

X-rays:

X-rays can be used to show sedimentary structures and other internal features of sediment cores are especially valuable for glacial facies. In Adobe Photoshop, the x-rays were altered to enhance the sediment; dark colors represented more dense material, whereas light colors represented less dense material. The x-rays can be divided into four facies: homogenous, wavy, continuous laminations, and discontinuous laminations (Figure 20). The wavy sediment facies is most likely a result of biogenic degassing in the core.

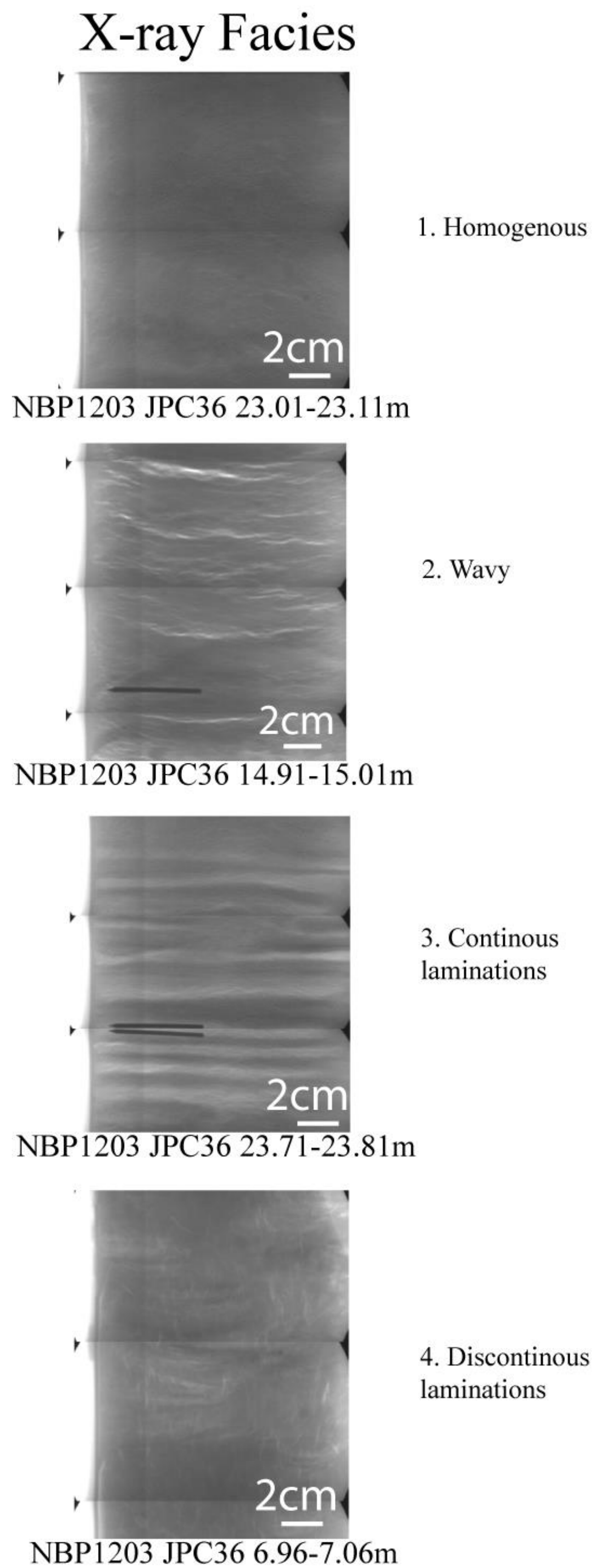

Figure 19: X-ray facies in NBP1203 JPC36.

The x-rays also reveal pebbles entrapped in the sediment (Figure 20). These are 2-4mm in diameter. There are many pebbles scattered throughout the core. These helped distinguish the sediment facies in the core.

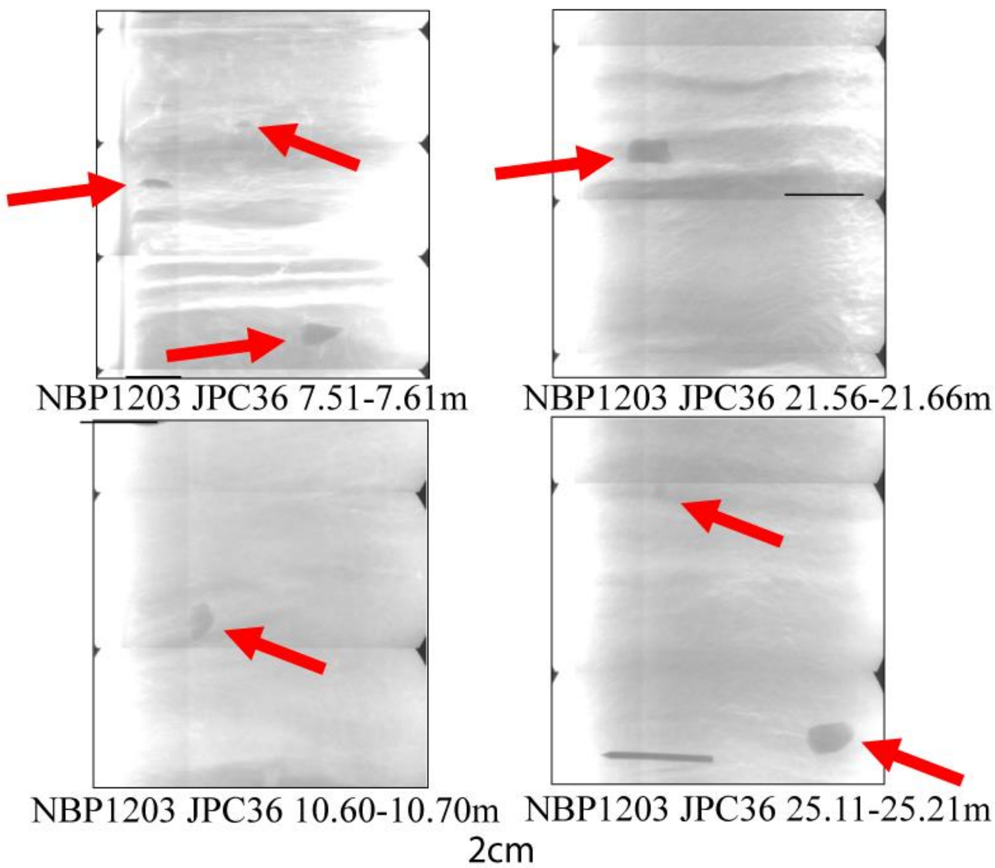

Figure 20: X-rays showing examples of pebbles in NBP1203 JPC36. Images are further enhanced in Adobe Photoshop for a clearer pebble outline.

Ikaite:

Table 1 shows the distribution of intervals of small, degraded ikaite and large, degraded monoclinic ikaite throughout the four different sediment facies in the core. While sieving, some degraded micro-ikaite was found (Figure 21). EDS, which allows for elemental analysis, was conducted on all ikaite crystals found while at the SEM. This was done to confirm the mineral's chemical composition, $CaCO_2 \cdot 6(H_2O)$. An example is shown in Figure 22 and Figure 23.

	Small, degraded ikaite	Large, degraded monoclinic ikaite
Facies 1	———	18.76-18.77m
Facies 2	———	———
Facies 3	9.86-9.87m	18.71-18.76m
	10.86-10.87m	———
	13.96-13.97m	———
	20.83-20.85m	———
	23.39-23.40m	———
Facies 4	0.71-0.74m	———
	6.46-6.47m	———
	9.56-9.57m	———
	14.61-14.66m	———
	14.78-14.80m	———
	17.31-17.33m	———
	17.36-17.37m	———
	17.45-17.46m	———
	19.96-19.97m	———

Table 1: Intervals of small, degraded ikaite and large, degraded monoclinic ikaite found in the four assigned sediment facies in NBP1203 JPC36.

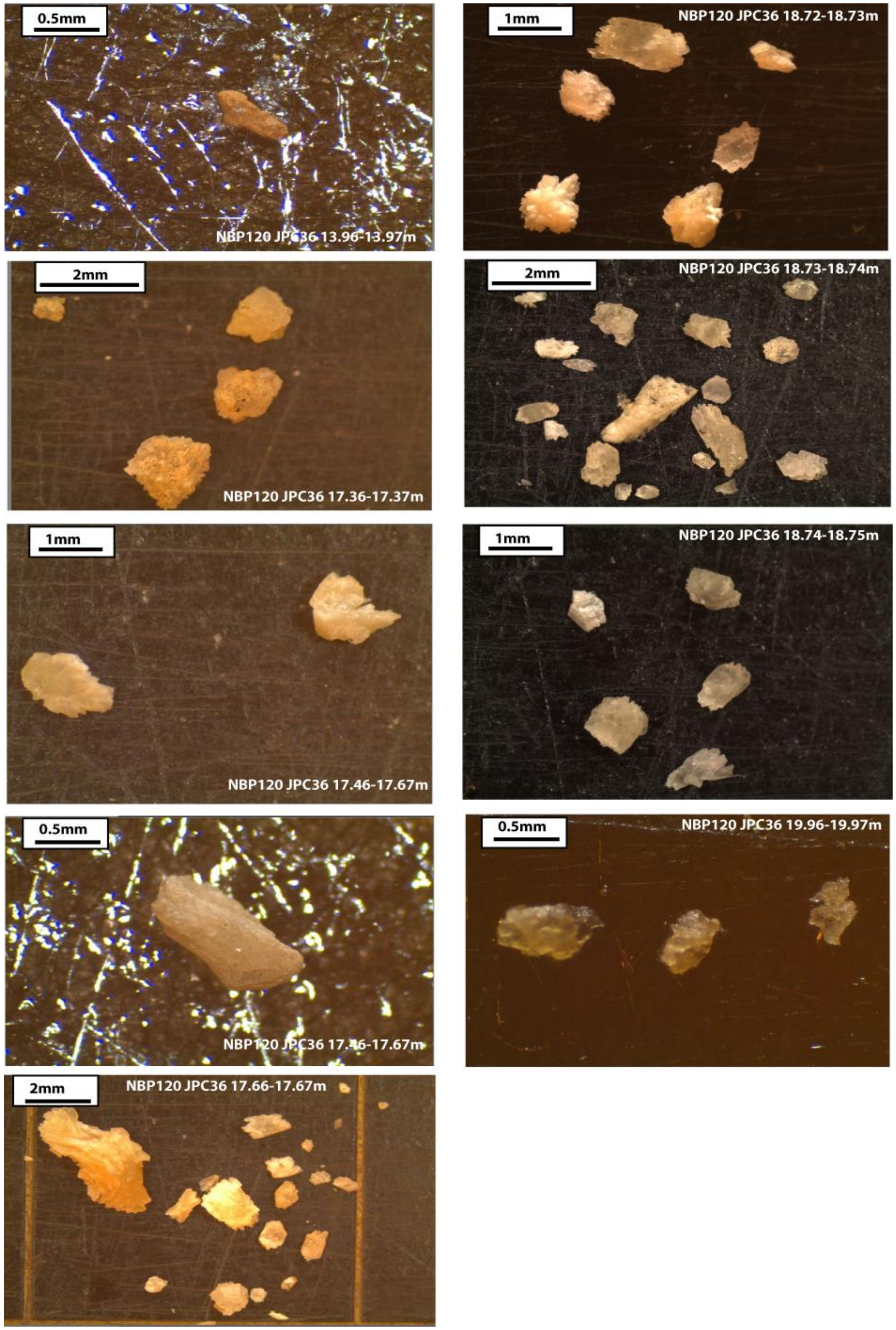

Figure 21: Small ikaite found in NBP1203 JPC36 during sieving.

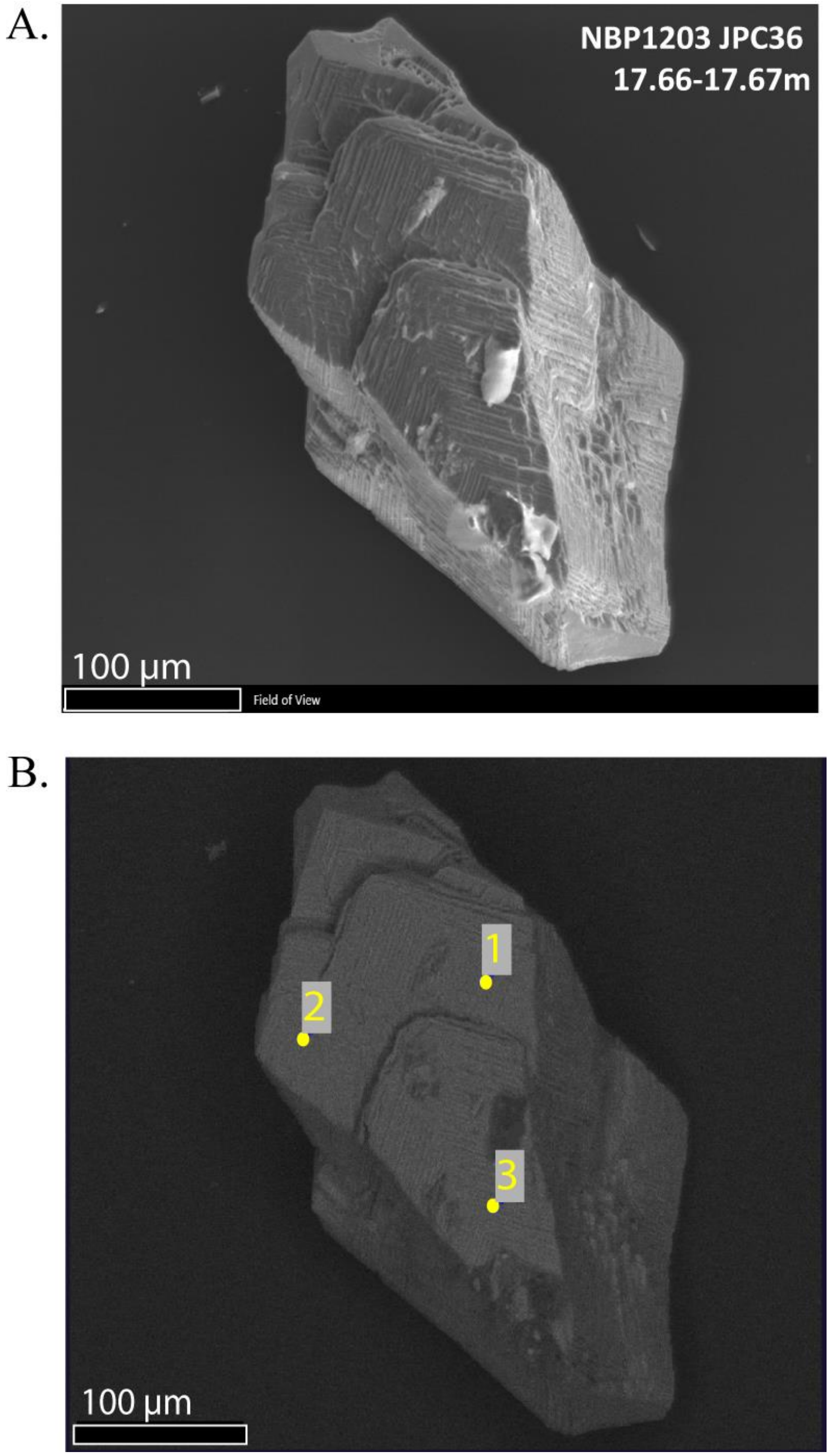

Figure 22: A) Example of an SEM image of an ikaite crystal.

B) Three points chosen for EDS.

A.

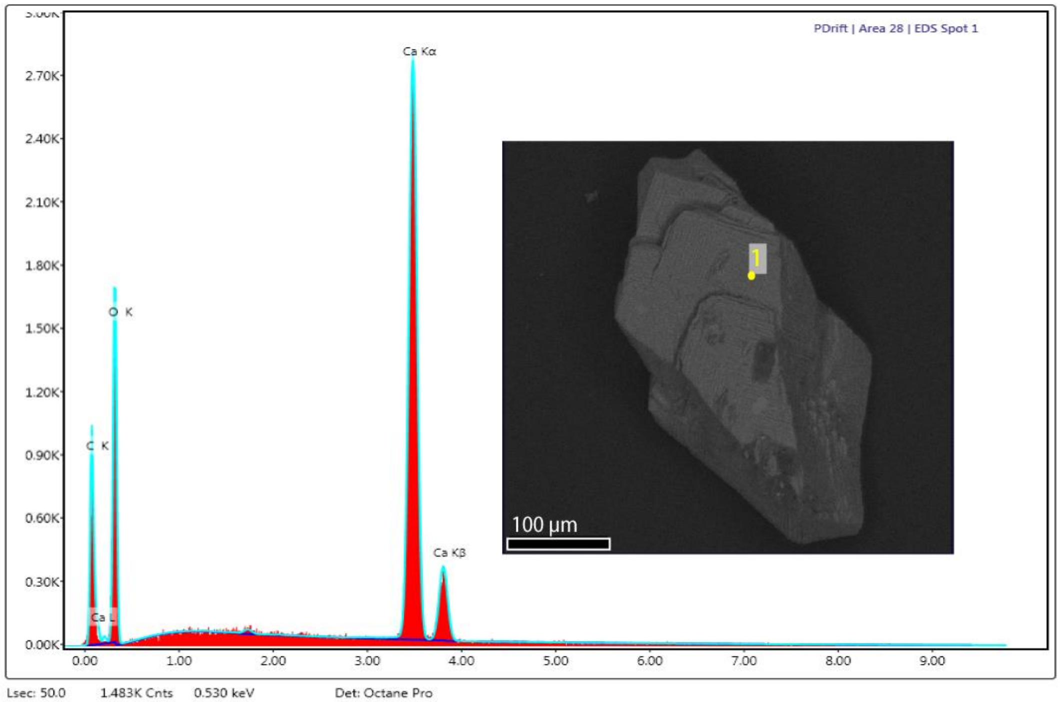
PDrift | Area 28 | EDS Spot 1
Ca Kα
O K
C K
Ca L
Ca Kβ
100 µm
1
Lsec: 50.0
1.483K Cnts
0.530 keV
Det: Octane Pro

B.

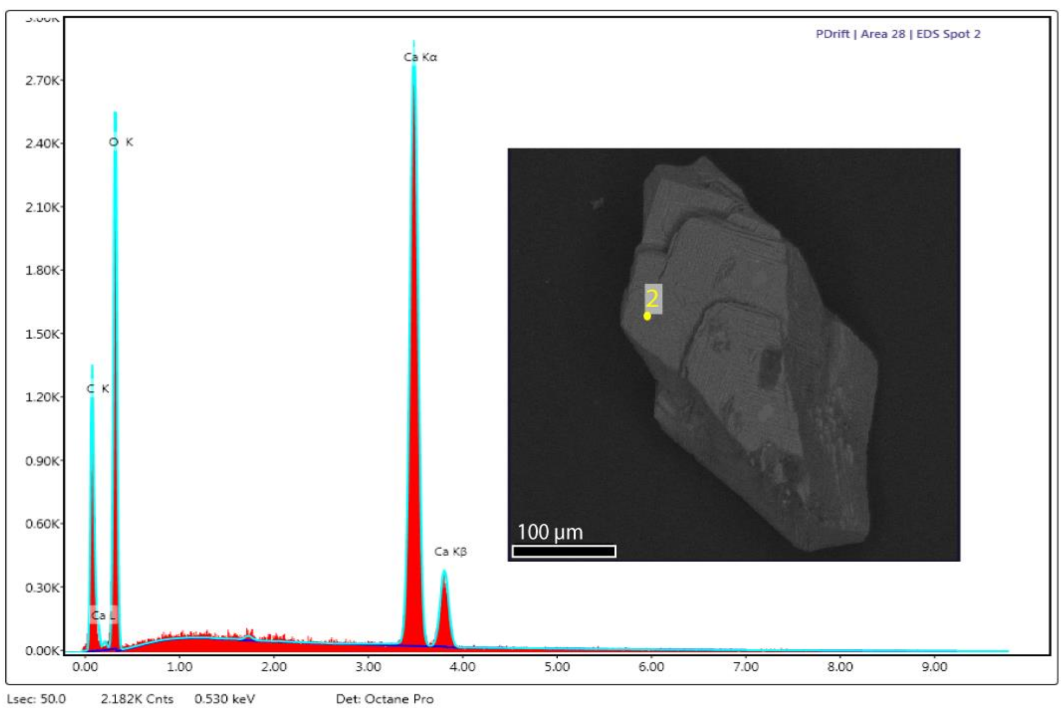
PDrift | Area 28 | EDS Spot 2
Ca Kα
O K
C K
Ca L
Ca Kβ
100 µm
2
Lsec: 50.0
2.182K Cnts
0.530 keV
Det: Octane Pro

C.

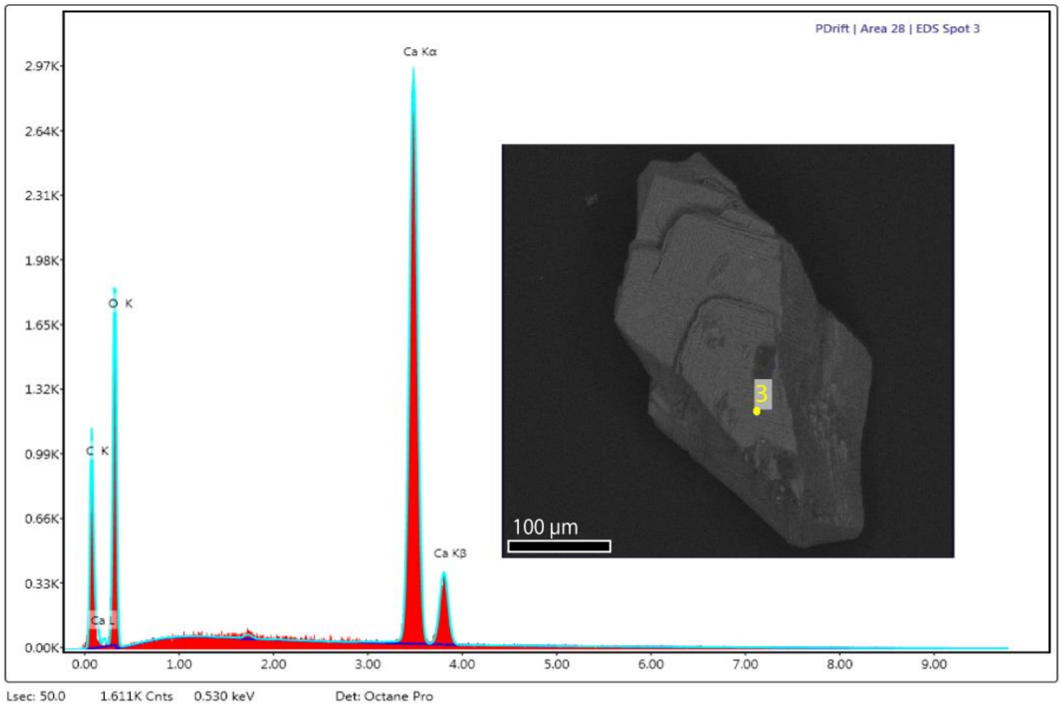

Figure 23:

A) Example of EDS of spot 1 on ikaite crystal. Inset, from Figure 22, shows exact location of sampled area.

B) Example of EDS of spot 2 on ikaite crystal. Inset, from Figure 22, shows exact location of sampled area.

C) Example of EDS of spot 3 on ikaite crystal. Inset, from Figure 22, shows exact location of sampled area.

Grain Shape:

A roughness coefficient (Rc) was found for 87 intervals, including the ikaite-bearing intervals, in NBP1203 JPC36 (Table 2). The Rc's range from 0.00408 to 0.00889 (Table 2). The Rc describes the difference in grain angularity. A well rounded grain will have an Rc closer to zero, while an angular grain will have an Rc closer to one. When the Rc increases, the angularity of the quartz grain increases and, conversely, when the Rc decreases, the angularity of the grain decreases (Ehrlich and Weinberg, 1970; Ehrlich et al., 1980; Livsey et al., 2013).

Sample name	Rc
NBP1203 JPC36 0.04-0.05m	0.00444
NBP1203 JPC36 0.29-0.3m	0.00797
NBP1203 JPC36 0.725-0.735m	0.00883
NBP1203 JPC36 0.89-0.9m	0.00889
NBP1203 JPC36 2.56-2.76m	0.00607
NBP1203 JPC36 2.81-2.82m	0.00641
NBP1203 JPC36 3.31-3.32m	0.00761
NBP1203 JPC36 3.81-3.82m	0.00537
NBP1203 JPC36 4.01-4.02m	0.00456
NBP1203 JPC36 4.16-4.17m	0.00600
NBP1203 JPC36 4.26-4.27m	0.00599
NBP1203 JPC36 4.36-4.37m	0.00630
NBP1203 JPC36 4.46-4.47m	0.00507
NBP1203 JPC36 4.61-4.62m	0.00647
NBP1203 JPC36 4.81-4.82m	0.00483
NBP1203 JPC36 4.96-4.97m	0.00408
NBP1203 JPC36 5.11-5.12m	0.00630
NBP1203 JPC36 5.31-5.32m	0.00806
NBP1203 JPC36 5.71-5.72m	0.00731
NBP1203 JPC36 6.26-6.27m	0.00750

Table 2: Grain shape data for NBP1203 JPC36. Ikaite intervals are highlighted in blue. Table continued on next page.

Sample name	Rc
NBP1203 JPC36 6.36-6.37m	0.00713
NBP1203 JPC36 6.46-6.47m	0.00866
NBP1203 JPC36 6.81-6.82m	0.00418
NBP1203 JPC36 7.41-7.42m	0.00629
NBP1203 JPC36 7.61-7.62m	0.00563
NBP1203 JPC36 8.01-8.02m	0.00532
NBP1203 JPC36 8.41-8.42m	0.00590
NBP1203 JPC36 8.56-8.57m	0.00516
NBP1203 JPC36 8.66-8.67m	0.00576
NBP1203 JPC36 9.06-9.07m	0.00494
NBP1203 JPC36 9.46-9.47m	0.00495
NBP1203 JPC36 9.56-9.57m	0.00470
NBP1203 JPC36 10.21-10.22m	0.00675
NBP1203 JPC36 10.26-10.27m	0.00670
NBP1203 JPC36 10.36-10.37m	0.00562
NBP1203 JPC36 10.46-10.47m	0.00731
NBP1203 JPC36 10.81-10.82m	0.00459
NBP1203 JPC36 10.86-10.87m	0.00727
NBP1203 JPC36 11.81-11.82m	0.00710
NBP1203 JPC36 12.16-12.17m	0.00651
NBP1203 JPC36 12.61-12.62m	0.00592
NBP1203 JPC36 12.81-12.82m	0.00631
NBP1203 JPC36 12.96-12.97m	0.00532
NBP1203 JPC36 13.01-13.02m	0.00599
NBP1203 JPC36 13.11-13.12m	0.00542
NBP1203 JPC36 13.16-13017m	0.00676
NBP1203 JPC36 13.46-13.47m	0.00506
NBP1203 JPC36 13.76-13.77m	0.00551
NBP1203 JPC36 13.96-13.97m	0.00553
NBP1203 JPC36 14.31-14.32m	0.00792
NBP1203 JPC36 14.46-14.47m	0.00523
NBP1203 JPC36 14.61-14.62m	0.00849
NBP1203 JPC36 14.62-14.63m	0.00525
NBP1203 JPC36 14.63-14.64m	0.00673
NBP1203 JPC36 14.64-14.65m	0.00615
NBP1203 JPC36 14.65-14.66m	0.00505
NBP1203 JPC36 14.76-14.77m	0.00481

Table 2 (cont.): Ikaite intervals are highlighted in blue. Table continued on next page.

Sample name	Rc
NBP1203 JPC36 14.78-14.79m	0.00439
NBP1203 JPC36 14.79-14.8m	0.00493
NBP1203 JPC36 15.31-15.32m	0.00640
NBP1203 JPC36 16.01-16.02m	0.00624
NBP1203 JPC36 17.06-17.07m	0.00717
NBP1203 JPC36 17.31-17.32m	0.00657
NBP1203 JPC36 17.32-17.33m	0.00511
NBP1203 JPC36 17.36-17.37m	0.00704
NBP1203 JPC36 17.45-17.46m	0.00604
NBP1203 JPC36 17.46-17.47m	0.00756
NBP1203 JPC36 17.66-17.67m	0.00579
NBP1203 JPC36 18.71-18.72m	0.00635
NBP1203 JPC36 18.72-18.73m	0.00669
NBP1203 JPC36 18.73-18.74m	0.00723
NBP1203 JPC36 18.74-18.75m	0.00571
NBP1203 JPC36 18.75-18.76m	0.00768
NBP1203 JPC36 18.76-18.77m	0.00724
NBP1203 JPC36 18.77-18.78m	0.00684
NBP1203 JPC36 19.01-19.02m	0.00579
NBP1203 JPC36 19.86-19.87m	0.00456
NBP1203 JPC36 19.96-19.97m	0.00551
NBP1203 JPC36 20.66-20.67m	0.00640
NBP1203 JPC36 20.71-20.72m	0.00867
NBP1203 JPC36 20.83-20.84m	0.00706
NBP1203 JPC36 20.84-20.85m	0.00537
NBP1203 JPC36 21.16-21.17m	0.00640
NBP1203 JPC36 21.26-21.27m	0.00578
NBP1203 JPC36 21.56-21.57m	0.00506
NBP1203 JPC36 22.16-22.17m	0.00514
NBP1203 JPC36 22.41-22.42m	0.00523
NBP1203 JPC36 22.66-22.67m	0.00545
NBP1203 JPC36 22.76-22.77m	0.00531
NBP1203 JPC36 22.96-22.97m	0.00437
NBP1203 JPC36 23.39-23.4m	0.00808
NBP1203 JPC36 23.51-23.52m	0.00624
NBP1203 JPC36 23.96-23.97m	0.00494
NBP1203 JPC36 24.56-24.57m	0.00597
NBP1203 JPC36 25.21-25.22m	0.00530
NBP1203 JPC36 25.51-25.52m	0.00466
NBP1203 JPC36 25.56-25.57m	0.00762

Table 2 (cont.): Grain shape data for NBP1203 JPC36. Ikaite intervals are highlighted in blue.

Grain Texture:

Quartz grain textures were analyzed for 44 intervals, including the 15 ikaite intervals, in NBP1203 JPC36. An overwhelming majority of the grains exhibited silica precipitation (Figure 24; Pittman, 1972; Mahaney, 2002; Narayana et al., 2010).

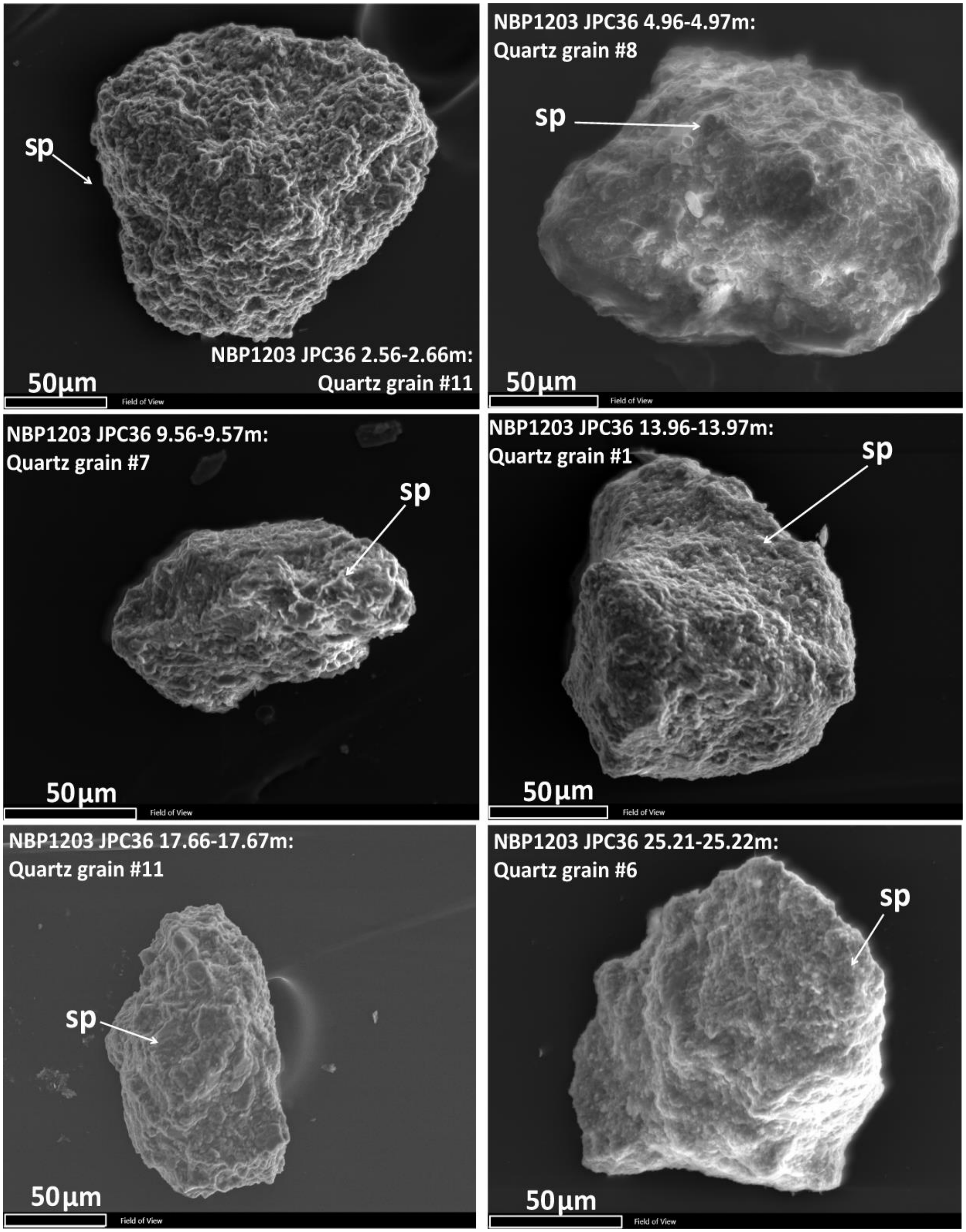

Figure 24: Silica precipitation (sp) is the most common microtexture in NBP1203 JPC36.

To assess whether the abundance of silica precipitation has any correlation with intervals containing ikaite or voids of ikaite, graphs of abundance were created (Figure 25; Figure 26). In both, a high abundance of silica precipitation dominates.

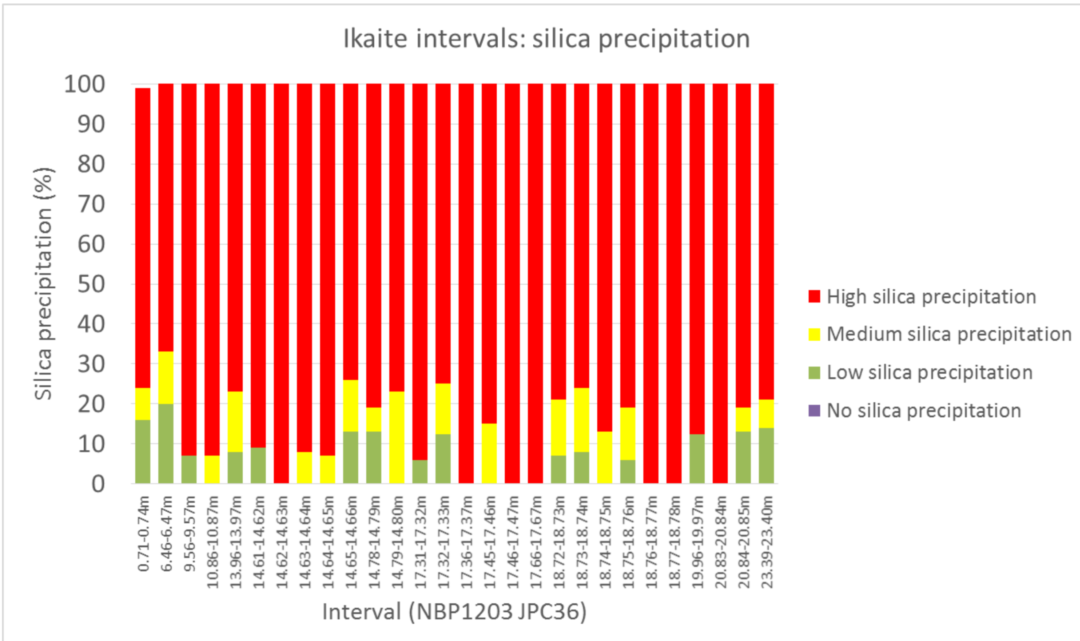

Figure 25: Abundance of silica precipitation in ikaite intervals.

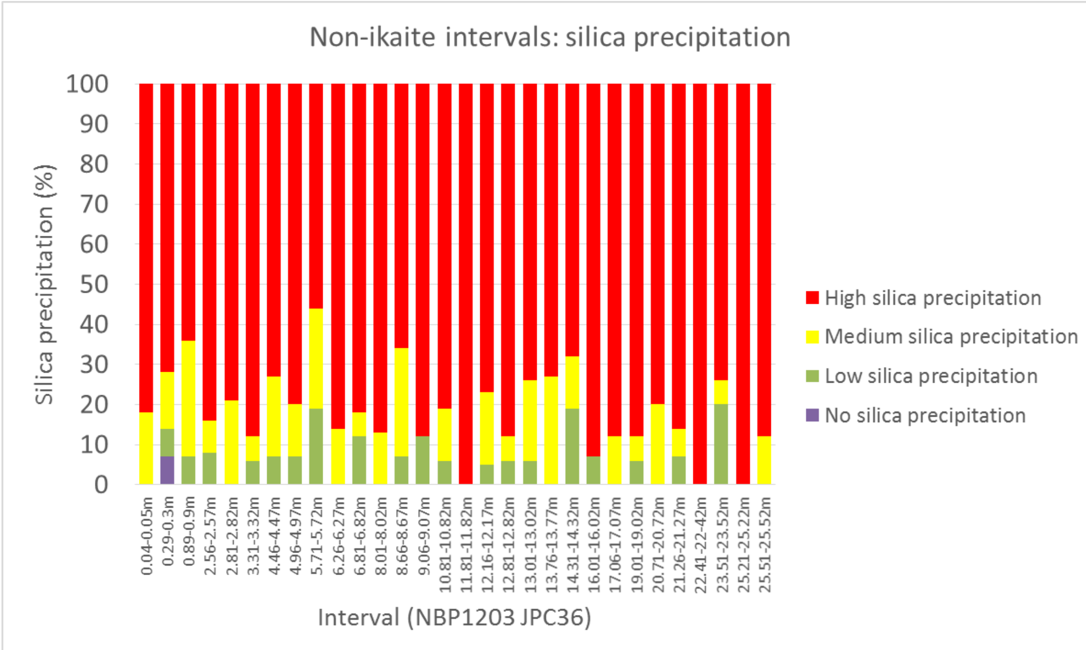

Figure 26: Abundance of silica precipitation in non-ikaite intervals.

Despite the very high abundance of silica precipitation on the majority of the grains, some show evidence of glacial, aeolian, or current transport (Figure 27; Figure 28; Figure 29, respectively). Overall, both ikaite and non-ikaite intervals show a high amount of glacial influence. In intervals containing ikaite, the amount of glacial microtextures ranged from 28-100%, the amount of aeolian microtextures ranged from 0-33.33%, and the amount of current microtextures ranged from 0-33.33% (Figure 30). In intervals void of ikaite, the amount of glacial microtextures ranged from 60-100%, the amount of aeolian microtextures ranged from 0-69%, and the amount of current microtextures ranged from 0-33.33% (Figure 31).

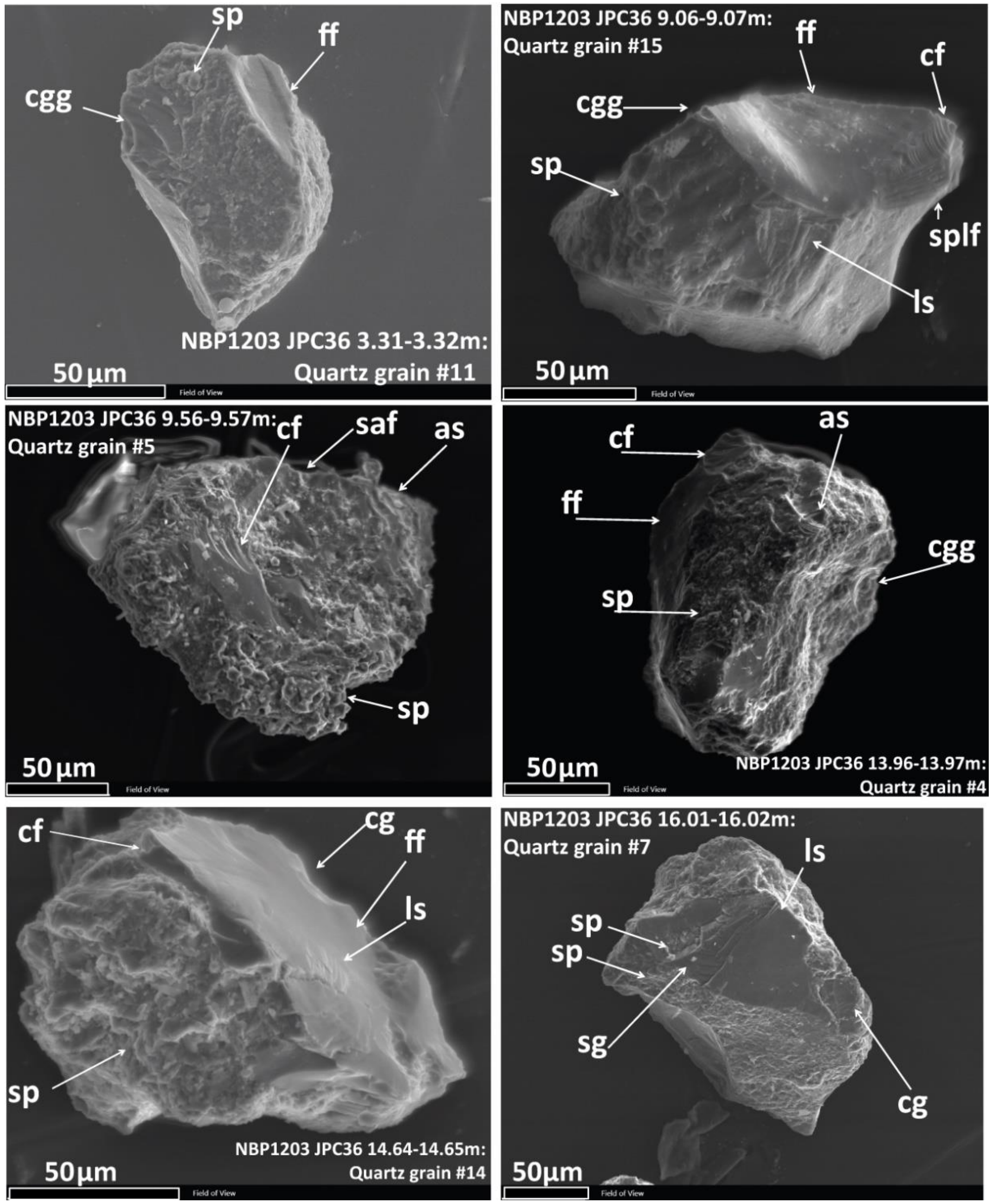

Figure 27: Examples of glacial influence in NBP1203 JPC36. Glacial microtextures include: crescentic gouges (cgg) and curved grooves (cg). Polygenetic microtextures include: fracture faces (ff), conchoidal fractures (cf), sharp angular features (saf), subparallel linear fractures (splf), linear steps, and asymmetrical steps (as). Silica precipitation (sp) is present.

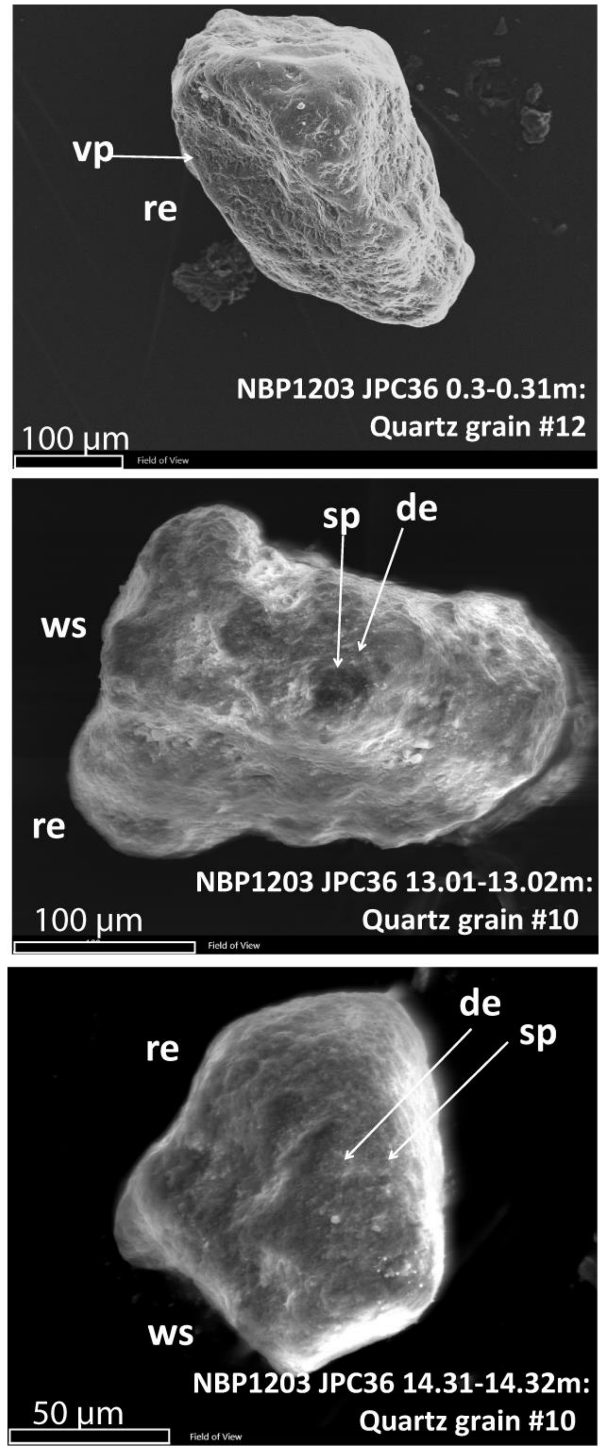

Figure 28: Examples of aeolian influence on grains in NBP1203 JPC36. Microtextures include: rounded edges (re), dissolution etching (de), weathered surface (ws), and v-shaped pits (vp). Silica precipitation (sp) is present.

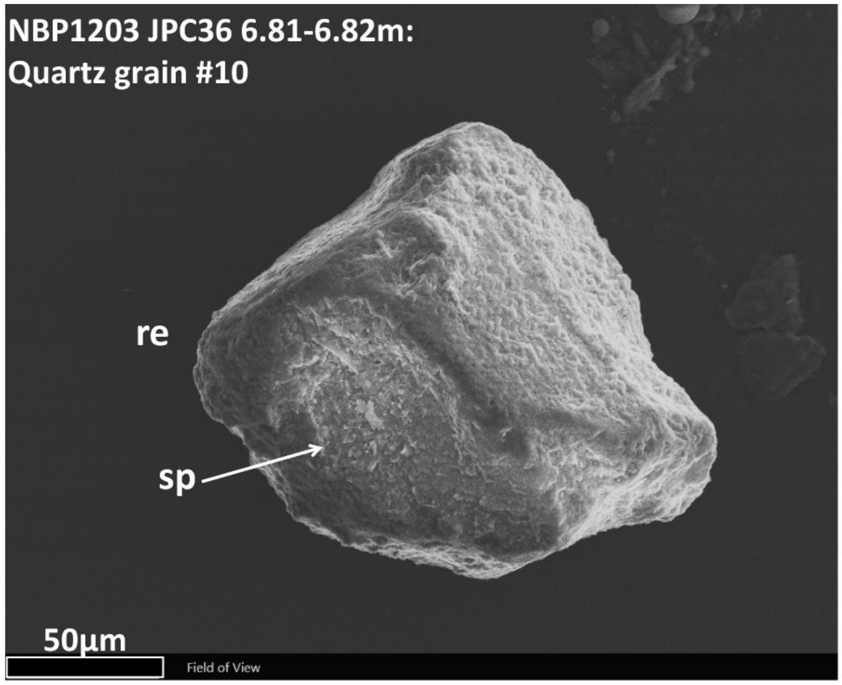

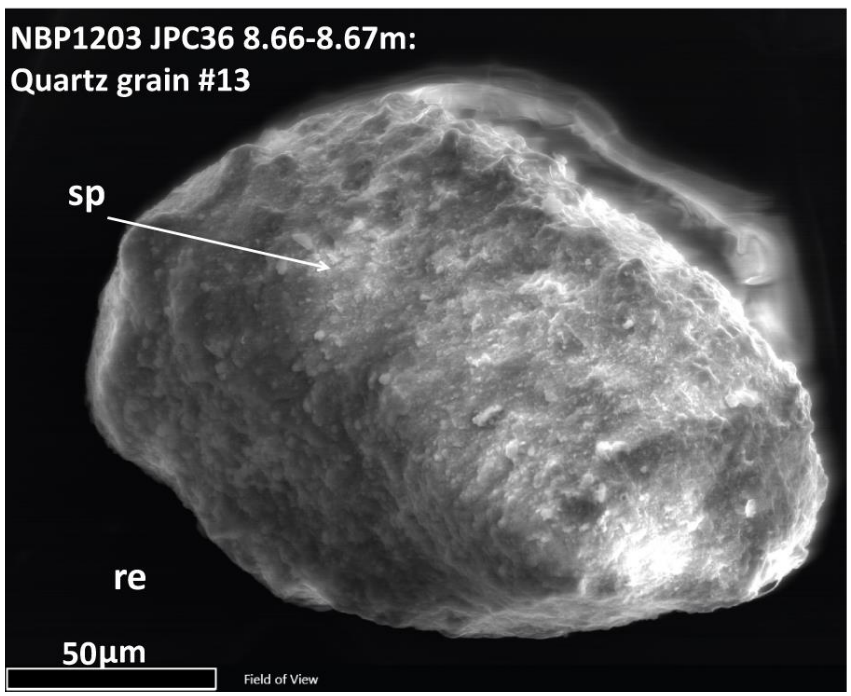

Figure 29: Examples of current influence in NBP1203 JPC36. Current microtextures include: rounded edges (re). The only detectable microtexture in these grains are rounded edges. Silica precipitation (sp) covers others.

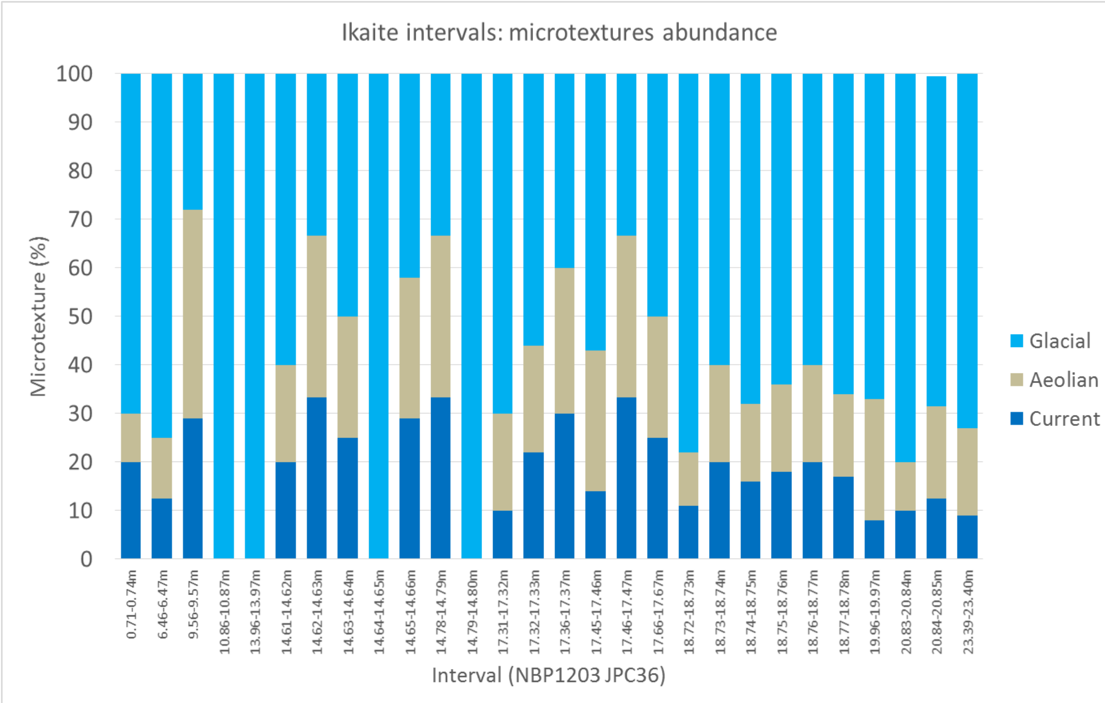

Figure 30: Abundance of glacial, aeolian, and current microtextures in ikaite intervals.

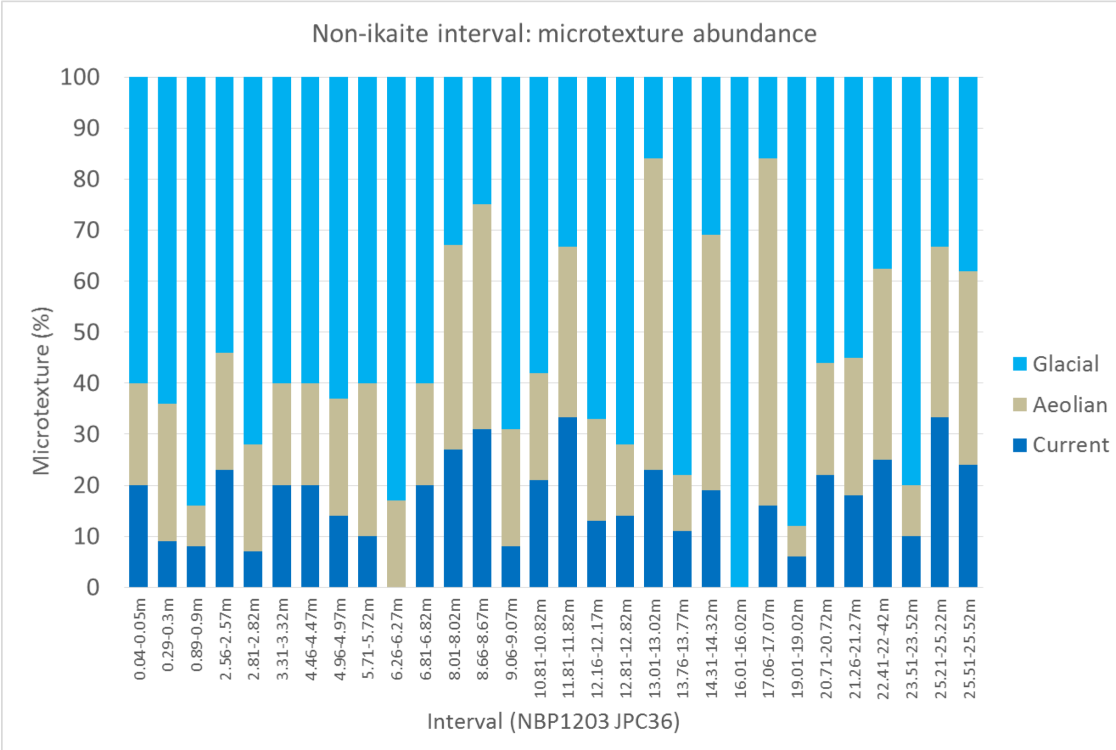

Figure 31: Abundance of glacial, aeolian, and current microtextures in non- ikaite intervals.

Diatom Abundance:

Chaetoceros spp. are the most dominant diatom in NBP1203 JPC36 making up more than 90% of the total relative species abundance. Only two intervals, 12.82m and 17.82m, show a ratio of resting spores versus vegetative cells at greater than one suggesting a warm environment with overall ample nutrients (Figure 32).

Fragilariopsos curta spp. are present in the core in small amounts at 5.32m and at 6.82m, at 1.72% and 2.22%, respectively (Figure 32). *Fragilariopsos cylindrus* spp. are sparse in the core, with the three largest peaks at 3.11m, 7.82m, and 10.82m, at 1%, 0.89%, and 1.5%, respectively (Figure 32).

The highest abundance of *Porosira glacialis* spp. exists at 11.82cm at 1% total abundance (Figure 32). *Thalassiosira antarctica* warm, are larger in size and represent a significantly higher total percent than *Thalassiosira antarctica* cold. *Thalassiosira antarctica* warm have major peaks at 7.82m, 11.82m, and 18.82m with percentages at 4.63%, 5.52%, and 4.98%, respectively (Figure 32). *Thalassiosira antarctica* cold have some small peaks at 4.82m, 6.82m, 15.82m and 19.82m, with percentages at 0.19%, 0.19%, 0.184%, and 0.20%, respectively (Figure 32).

Fragilariopsos kerguelensis spp. occur very seldom throughout the core at 2.32m, 6.32m, 10.82m, and at 15.82m with at 0.20%, 0.19%, 0.187%, and 0.184%, respectively (Figure 32). *Cocconeis spp.* high abundance in the core is due to rafted algal mats or downslope transport (Figure 32; Vadman, 2014).

The *Chaetoceros* resting spore to vegetative cell ratio shows conditions with ample nutrient availability except for the two peaks. During this time, it is expected that sea ice is present as opposed to open water conditions (Leventer et al., 2002). However, these intervals do not correlate with high peaks of sea-ice diatoms (Figure 32). From this, it is evident that although primary productivity is high in the site, *Chaetoceros* vegetative cells may not be dependent on sea-ice-derived iron (Vadman, 2014).

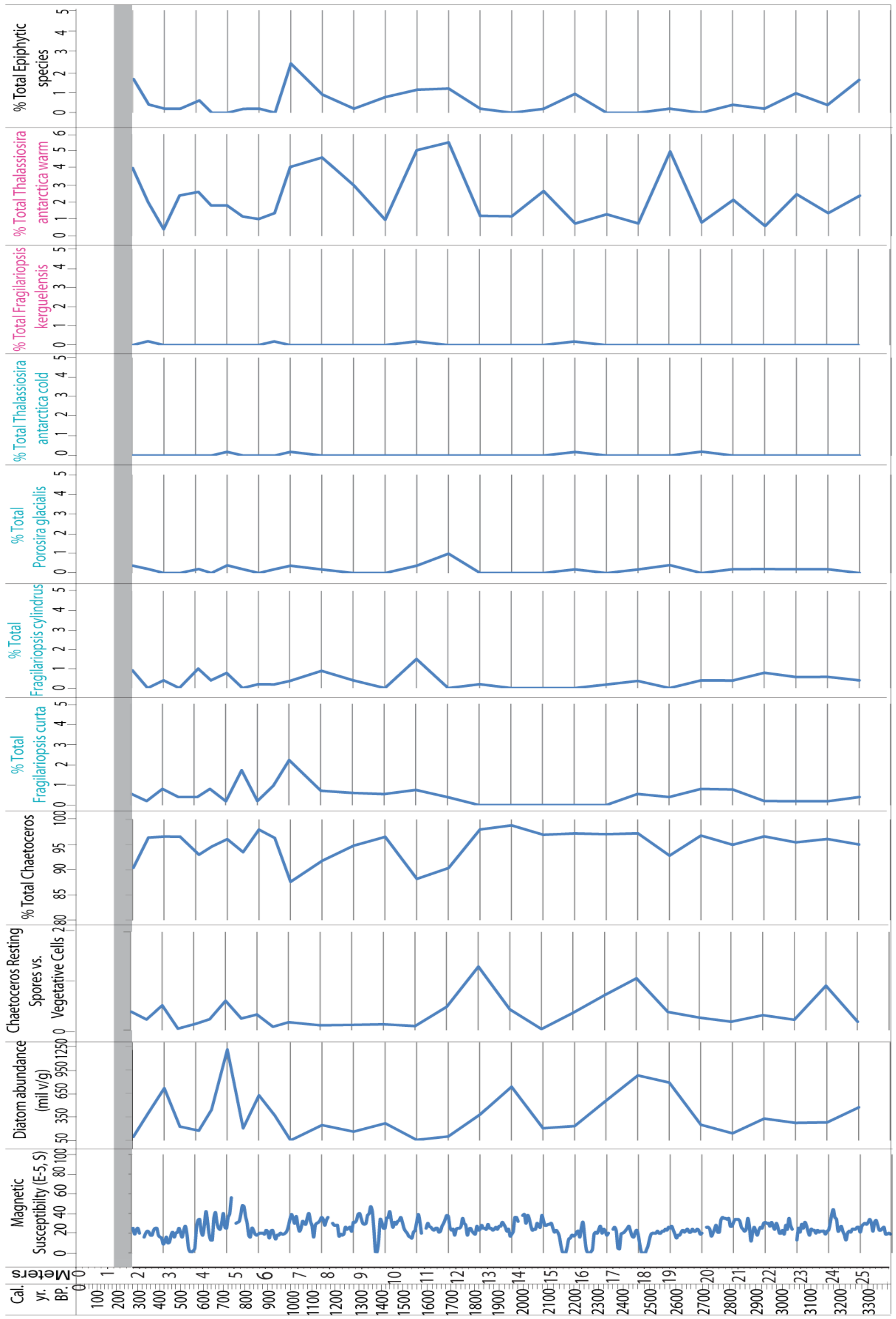

Figure 32: Magnetic susceptibility, diatom abundance, *Chaetoceros* resting spores versus vegetative cells, and percent total diatom species in NBP1203 JPC36. Diatom data from Kara Vadman and Dr. Amy Leventer from Colgate University.

Magnetic Susceptibility:

Magnetic susceptibility (MS) records whether the sediment is from a terrestrial or biogenic source (Domack and McClennen, 1996; Leventer et al., 1996; Brachfeld et al., 2002). Higher magnetic signals indicate land-derived sediment with a high abundance of iron-rich minerals, whereas lower magnetic signals indicate a high contribution from biogenic diatom mud and ooze (Leventer et al., 1996). Therefore, low MS will correlate with warmer sea-surface temperatures and high diatom abundance, while high MS will correlate with cooler sea-surface temperatures and low diatom abundance (Leventer et al., 1996). NBP1203 JPC36 has a relatively constant MS signal through time (Figure 33). However, previous studies show that the MS signals in the northeastern AP, near the Perseverance Drift, show no correlation with diatom abundance (Perez et al., 2005). From this it can be concluded that the terrigenous input into the study site holds a complex relationship between MS and biologic productivity.

To reinforce the complexity of the MS in the Perseverance Drift, it can be seen that the MS does not correlate to any of the diatom curves (Figure 33). The low abundance of sea-ice diatoms and high abundance of warm, open marine diatoms suggests open marine conditions present through time. However, intermittent sea ice has been present allowing for a small percentage of sea ice diatoms to thrive.

Density:

The density log allows for the measure of down-core compaction. It can also highlight potential lithologic changes. In NBP1203 JPC36, the density remains constant (Figure 33).

Units:

To help understand the relationship between facies, intervals of ikaite, grain size, pebble counts, grain shape, grain texture, diatom abundance, magnetic susceptibility, and density, a compilation of these data was drafted (Figure 33). Based on these data, two main units make up the core: Unit 1 and Unit 2. These are based on the four sediment facies that define the core.

Black to grey sediment is interpreted to have a high terrigenous input and olive-green sediment is interpreted to have a high biogenic component. At 11.90m, a distinct change in facies occurs from a dominance olive green to dominance in grey to black facies (Figure 33). Unit 1 extends from 0-11.90m, or 0-1,700 cal. yr. BP. Unit 2 extends from 11.90- 25.81m, or 1,700-3,375 cal. yr. BP. The presence of ikaite intervals in these units is shown in Table 3.

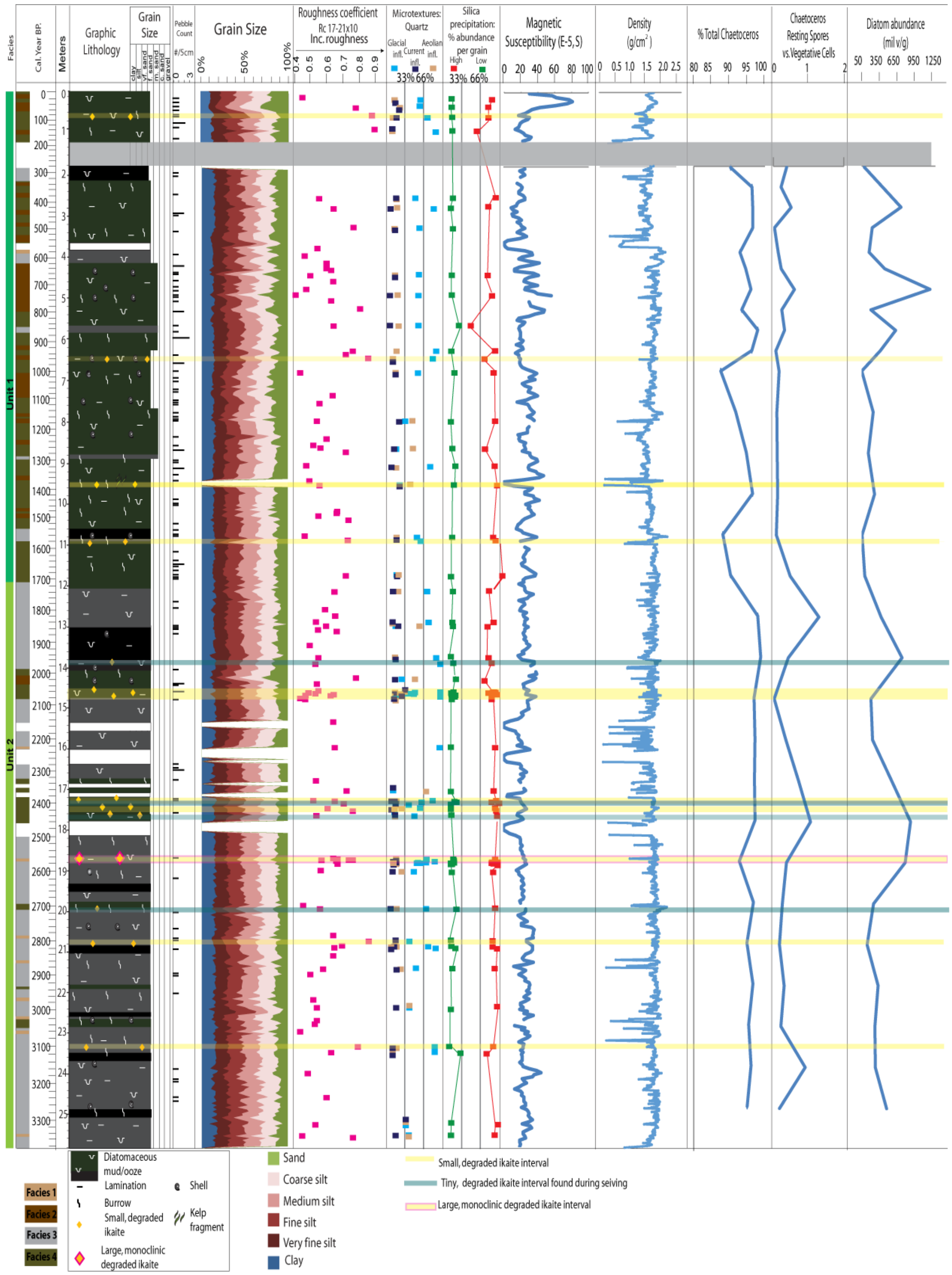

Figure 33: Compilation of data for NBP1203 JPC36.

Facies	Unit 1	Unit 2
1	————	18.76-18.77m* 1cm of a larger interval*
2	————	————
3	10.86-10.87m 13.96-13.97m 2 intervals	9.86-9.87m 18.71-18.72m 18.72-18.73m 18.73-18.74m 18.74-18.75m 18.75-18.76m 20.83-20.84m 23.39-23.40m 4 intervals
4	0.71-0.74m 6.46-6.47m 9.56-9.57m 3 intervals	14.61-14.62m 14.62-14.63m 14.63-14.64m 14.64-14.65m 14.65-14.66m 14.78-14.80m 17.31-17.33m 17.36-17.37m 17.45-17.46m 19.96-19.67m 6 intervals

Table 3: The four sediment facies and their corresponding ikaite intervals. Purple color represents a single interval split up by one centimeter.

Chronology Data

The isotopic dating method used in NBP1203 JPC36 was ^{14}C dating. Because of the abundance of calcareous forams in the core, a reliable radiocarbon age model can be created (Table 4; Figure 34). The ages reveal a sedimentation rate of 7.64 mm/yr.

Depth (m)	Age (years)	Calibrated Age (cal. yrs. BP)	Age Error (years)
1.81	1,500	282	20
3.04	1,630	422	20
4.21	1,810	536	20
4.56	1,880	596	20
7.96	2,150	1,217	20
10.92	3,010	1,744	20
13.32	3,510	1,900	20
15.80	3,310	2,091	20
24.99	4,270	3,284	20

Table 4: Foram sample depth and its corresponding calibrated age with an age error of ±20 years. Raw ages are also shown.

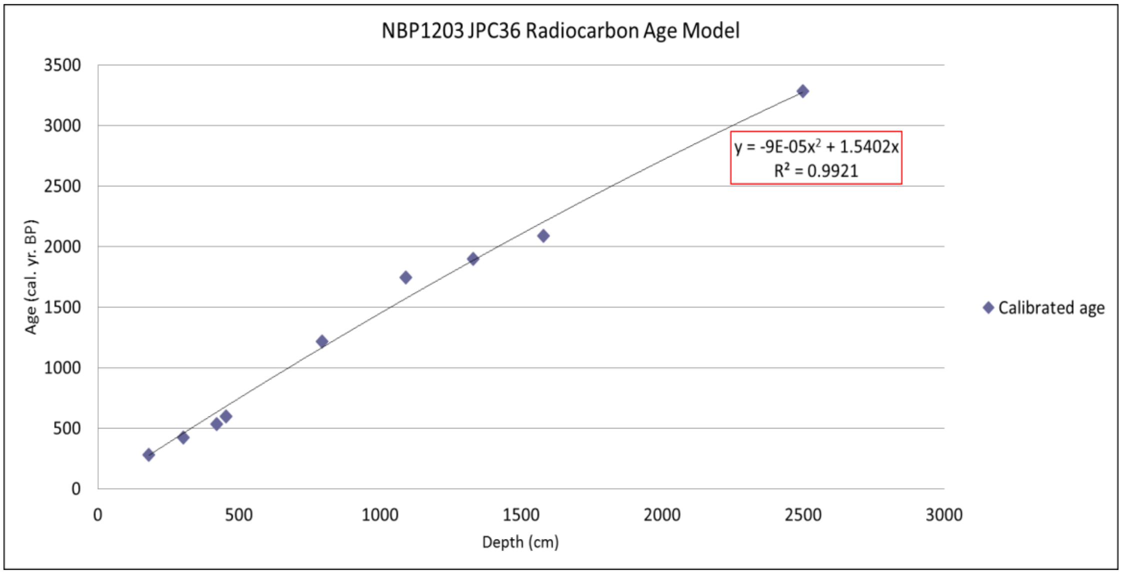

Figure 34: Age model for ^{14}C dates. A best fit second-order polynomial is used.

Discussion

The retreat of grounded ice around Antarctica is characterized by extreme variability. By 5,000 cal. yr. BP the grounding line was on the innermost shelf in the northeastern AP (Anderson et al., 2002). Therefore, the Perseverance Drift was deposited in open marine conditions from >3,375 cal. yr. BP to present.

Terrigenous Sediment Input Mechanisms

Terrigenous sediment is delivered to the Perseverance Drift by aeolian, iceberg, and current processes. This can occur by the melting of seasonal sea ice or direct transport from proximal exposed land that contributes sediment ranging from clay to fine-grained sand grains. After melting, icebergs also contribute terrigenous sediment to the deposit. These grains can be clay- to pebble-sized. Because the Perseverance Drift is formed by currents, they have a very large influence on the sediment delivery to the site. The strong bottom water currents are a big contributor of terrigenous material to the site. The winnowing of currents leaves behind a sandy to gravelly lag, and this current influence is likely responsible for the majority of the sand delivered to the site.

Biogenic Sediment Input Controls

Biogenic sediment is delivered to the Perseverance Drift by large phytoplankton blooms. The contribution of terrigenous silt- and clay-sized particles allow for the delivery of iron, which supplies nutrients to the diatoms and, in warm, open marine conditions, allows for these large blooms (Sedwick and DiTullio, 1997; Sedwick et al., 2000; Shen et al., 2006; Lannuzel et al., 2007; Raiswell et al., 2008; Atkins and Dunbar, 2009). These diatoms contribute silt-sized particles to the site. These particles can be broken up and contribute to the clay-sized fraction of this deposit. Heavy sea-ice coverage and low light levels can decrease the biogenic contribution to the site (Leventer et al., 2002).

Sediment Facies

Sediment Facies 1 is interpreted to be deposited in an open marine environment with cooler conditions and varied sea ice coverage (Figure 35). Its dark colors represent a strong terrigenous input. The dominant transport mechanism of the terrigenous sediment in this facies are very strong currents. This is a result of the presence of a high sand fraction that is interpreted to be a result of the winnowing of currents, which leave behind a sandy lag. Clay-sized to very fine-sand-sized particles are contributed by the melting of seasonal sea ice, which releases terrigenous grains sourced from aeolian transport. Direct contribution of terrigenous sand, silt, and clay also occurs by aeolian processes. This allows for biogenic productivity to occur, which accounts for the abundance of diatomaceous mud in the facies. However, intermittent sea ice is interpreted to be present, and therefore, mutes the contribution of biogenic productivity due to unfavorable conditions.

Sediment Facies 2 is interpreted to be deposited in an open marine environment with warm climate conditions and high biogenic productivity (Figure 35). Its green colors represent a strong biogenic input. A very strong current influence allows for winnowing leaving behind a sandy lag. The sand in this facies is also result of iceberg-rafting releasing sand-sized particles during melting. There is a high abundance of pebbles also transported via iceberg-rafting in this facies. This provides clues for a warm climate. The constant and direct input of sand, silt, and clay from aeolian processes and warm, open marine conditions allow for high diatom productivity, which is responsible for the high abundance of green, diatomaceous mud in the facies.

Sediment Facies 3 is interpreted to be deposited in cooler, open marine conditions with a strong terrigenous input based on the sediment's black and grey colors (Figure 35). Although the amount of sand is low in this facies, the winnowing of currents carrying terrigenous material allows for some of the sand to be deposited in this location. These currents are not as powerful as the ones responsible for Sediment Facies 1 and 2 because they do not contribute a high amount of sand, but they still do winnow mud from sand that is brought by the currents. Some of the low sand fraction is also likely a result of the melting of available seasonal sea ice, which contributes clay to very fine sand-sized grains to the seafloor. Iron-rich silt and clay are blown directly from exposed land allow for biogenic productivity, which results in the diatomaceous mud found in this facies. However, biogenic productivity decreases under the interpreted sea ice coverage. Therefore, both the currents and aeolian processes contribute the high amount of terrigenous material in the facies.

Sediment Facies 4 is interpreted to be deposited in warm, open marine conditions with a strong biogenic input based on its green colors (Figure 35). This is also consistent with the high abundance of pebbles in the facies which provide evidence for a warm climate. The low abundance of sand in this facies is a result of strong currents in the area, which allow for winnowing to leave behind a sandy lag. Similarly to Sediment Facies 3, the currents depositing this facies are not as strong as Sediment Facies 1 and 2 because of the low abundance of sand. Another source for the low abundance of sand in this facies is contributed to iceberg rafting releasing sand-sized particles during melting. The high abundance of green, diatomaceous mud is likely a result of high diatom productivity due to input of silt and clay from direct aeolian processes along with warm, open marine conditions.

In all facies, silt-sized grains dominate. The silt-sized fraction is sourced from both terrigenous sources and biogenic sources.

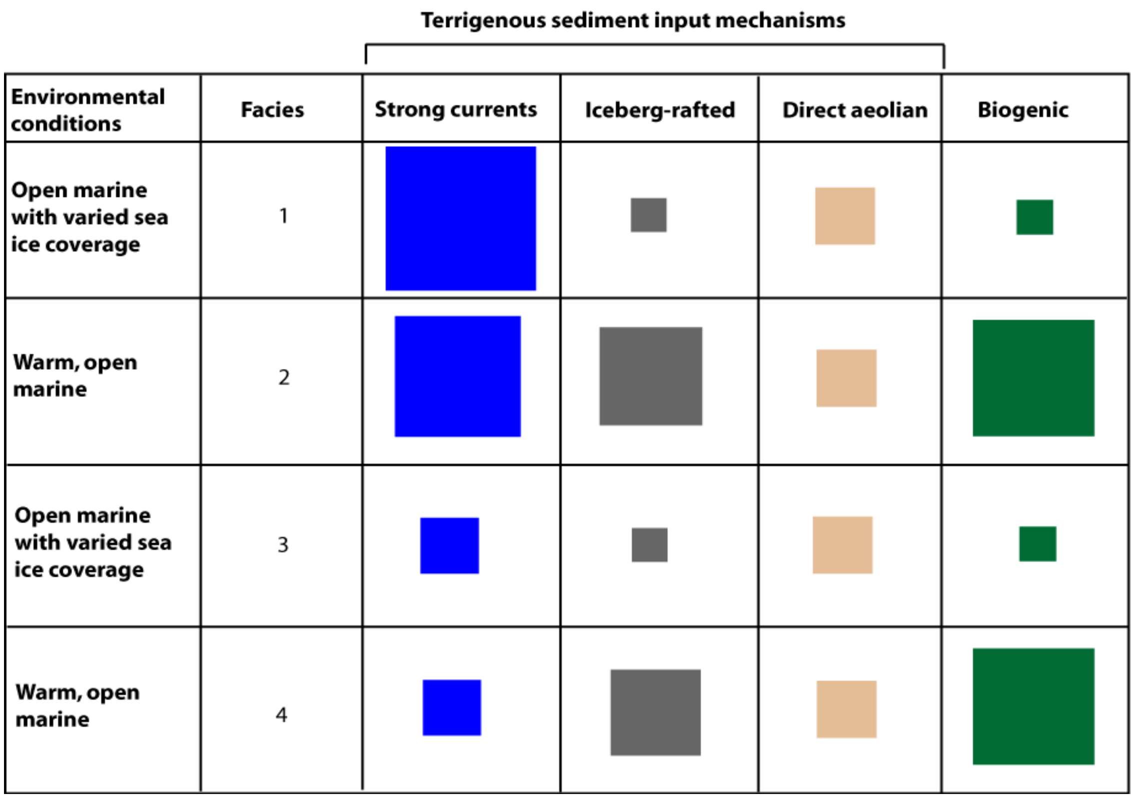

Figure 35: Varying sizes of squares represent the abundance of sediment input to the Perseverance Drift by its respective transport mechanism. Signal of currents and iceberg-rafted material varies through time based on grain size. Sea ice coverage controls the signal of biogenic input to the drift. Direct aeolian transport remains constant and independent of the climate.

Units

A change in the primary source of sediment is represented at the boundary between Unit 1 and Unit 2. Unit 1, from 0-1,700 cal. yr. BP, is comprised of mainly Facies 4. This suggests the site experienced a strong biogenic input. Unit 2, from 1,700-3,375 cal. yr. BP, is comprised of mainly Facies 3. This suggests the site experienced a strong terrigenous input. The rapid increase in pebble concentration from Unit 2 to Unit 1 also shows evidence of a change. With warmer and more permanent open marine conditions, an increase in coarse-grained material delivered to the site via icebergs is expected. In both units, there is a relatively constant contribution of clay, which is due to the direct input of terrigenous and biogenic clay-sized grains to the site. This high abundance of diatomaceous mud reinforces the overall, open marine conditions with moderate to high productivity through time.

Unit 1 is shows an abundance of Facies 2 and Facies 4. The majority of the sand that was delivered to the site is most likely a result of strong current winnowing, which removed fine-grained material, and iceberg transport releasing clay- to pebble-sized grains to the site. This requires warm, open ocean conditions. However, due to the Perseverance Drift's proximity to land, there is a constant influx of terrigenous sediment from direct aeolian delivery. A high iron input allowed for high marine organic sedimentation in the unit.

Unit 2 shows evidence of a dominant terrestrial influence by an abundance of Facies 3. Facies 1 is sparse overall. These low pulses of sand can be contributed to a cooler period with more perennial sea ice. However, seasonal melting of the sea ice contributes terrigenous sand grains to the site. The winnowing of fine-grained material by water bottom currents also contributes terrigenous sand to this unit. The presence of sea ice decreases the signal of biogenic sedimentation, allowing for the terrigenous component to dominate.

Unit 2 also shows two intervals of a *Chaetoceros* resting spore to vegetative cell ratio that is greater than one (Figure 33). Leventer et al. (2002) suggest that high resting spore abundance correlates with high concentration of diatoms linked to sea ice and sea-ice melt, as opposed to melting conditions. Leventer et al. (1996) also suggest that sea-ice melt contributes to water column stratification and massive, nutrient-depleting blooms, which are a result of iron being supplied to the system. However, the Perseverance Drift has relatively constant, high primary productivity of *Chaetoceros*, and this suggests that their vegetative cells may not be dependent on sea-ice-derived iron (Vadman, 2014).

Climate Interpretation

If Facies 1 and Facies 3 are characterized by a strong terrigenous input and sea-ice coverage, then they correlate to a cooler time period. From this, we can interpret 1,700->3,375 cal. yr. BP as the Neoglacial time period at this site. Various studies show the extent of the Neoglacial period varies throughout the AP (Figure 36). If Facies 2 and 4 are characterized by a strong biogenic input, then they correlate to a warmer time period. From this, we can interpret 0-1,700 cal. yr. BP as a Warm Period (Figure 36). This is a similar climate pattern to the Bransfield Basin study done by Barnard and others (2014), in which the Neoglacial is present from 2,700-1,600 cal. yr. BP and the MWP is from 1,600-600 cal. yr. BP (Figure 36). However, the Perseverance Drift is a drift deposit and may not record Late Holocene climate as well as other locations around the AP can. This is a result of the drift deposit is collecting sediment sourced from many regions from the AP and may not be a perfect model for paleoclimate reconstruction. Because the Perseverance Drift is downstream of collapsing ice shelves, freshwater from glacial melt, and IRD from the southern portion of the AP, it may be recording climate signals from the south (Hellmer et al., 2011).

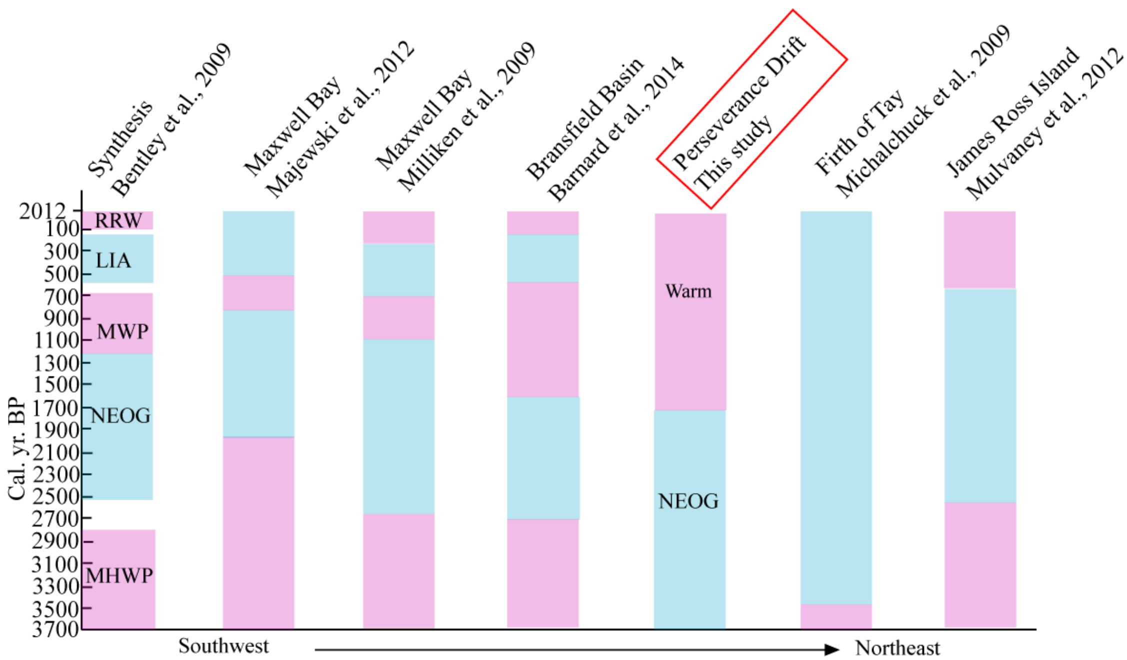

Figure 36: Late Holocene climate reconstruction in the northern AP. The Perseverance Drift shows evidence of the Neoglacial from >3,375-1,700 cal. yr. BP and a warming period from 1,700 cal. yr. BP to present (Modified from Barnard et al., 2014). The date for the end of the Neoglacial here is 100 years earlier than as recorded in the Bransfield Basin.

Ikaite

There is a spatial limitation of ikaite throughout the AP. It can be found in the Bransfield Basin, Firth of Tay, Vega Drift, and the Perseverance Drift (Figure 10). At the Bransfield Basin site, ikaite is found in hemipelagic muds (Suess et al., 1982). The Firth of Tay contains organic-rich, diatomaceous muds and ikaite (Domack et al., 2007). The Vega Drift, the site most similar to the Perseverance Drift, is a hemipelagic and pelagic depositional environment with organic-rich diatomaceous mud, IRD, and layers of volcaniclastic sand sourced from ice rafting, ash falls, or meltwater plumes (Camerlenghi et al., 2001; Backman and Domack, 2003). Although the Perseverance Drift's sand is not derived from a volcanic source, the site shares the similarity in high abundance of sand.

Unit 2 shows a higher abundance of ikaite intervals than Unit 1, 11 intervals versus 4. According to Zhou et al. (in press), ikaite forms with the contribution of iron-rich dust to the seafloor, and this allows for the release of phosphate during iron reduction to form the mineral. Within Unit 2, one centimeter of an ikaite interval is in Facies 1, four intervals are in Facies 3, and six intervals are present in Facies 4 (Table 3). The intervals of ikaite do not all appear in Facies 2, but this unit's strong, continuous terrigenous component aids in the formation of many ikaite intervals in other facies. Unit 1 has two ikaite intervals from Facies 3 and three ikaite intervals from Facies 4 (Table 3). There are no intervals of ikaite in Facies 1 and 2. This suggests that ikaite can form in biogenic-rich intervals as well. There is a constant contribution of terrigenous sediment to the site by sediment blown directly from land and transported by currents, allowing for ikaite to form in all facies. Specifically, the cold, deep Weddell Sea Transitional Water, one of the factors for ikaite's formation, could be the current responsible for the high terrigenous input.

Grain Shape and Grain Textures

The use of grain size and shape for clues to sediment transport history proved to be ineffective. While the discovery of silica precipitation on the grains tells a story within itself, the majority of original textures indicating glacial, aeolian, or current transport were covered. Because of this, the high resolution shape data also became unusable because it was not representing a clean grain with an outline representing its past transport history. Instead, it shows a grain either smoothed or roughened by silica precipitation.

Mean grain size and roughness coefficients (Rc) were also compared; however, no clear trend is shown between the two parameters (Figure 37). The intervals containing ikaite have a mean grain size ranging from 12.78μm to 22.76μm and an Rc from 0.00439 to 0.00846. The intervals without ikaite have a mean grain size ranging from 11.66μm to 32.13μm and an Rc from 0.00408 to 0.00867. These grain sizes are representative the fine- to medium-silt range.

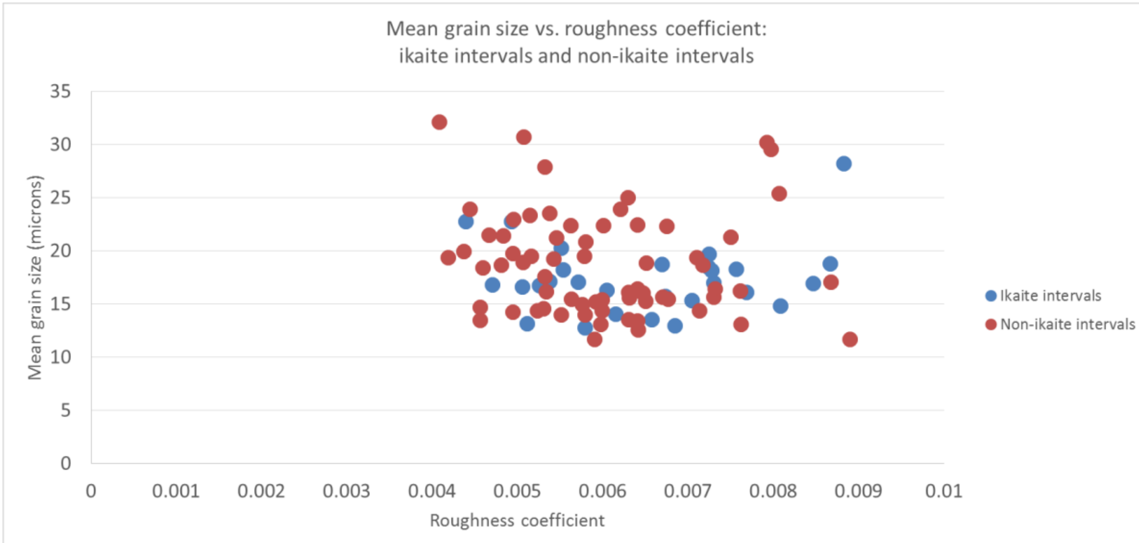

Figure 37: Comparison between mean grain size and roughness coefficient in ikaite and non-ikaite intervals.

To see if Rc changed throughout NBP1203 JPC36, Rc and depth were compared (Figure 38). Both the ikaite intervals and non-ikaite intervals have a relatively similar range in roughness coefficients down-core. The intervals containing ikaite have an Rc from 0.00439 to 0.00846. The intervals without ikaite have an Rc from 0.00408 to 0.00867. None of these comparisons have a correlation because of the silica precipitation found on the majority of the grains most likely alters the true shape of the grain.

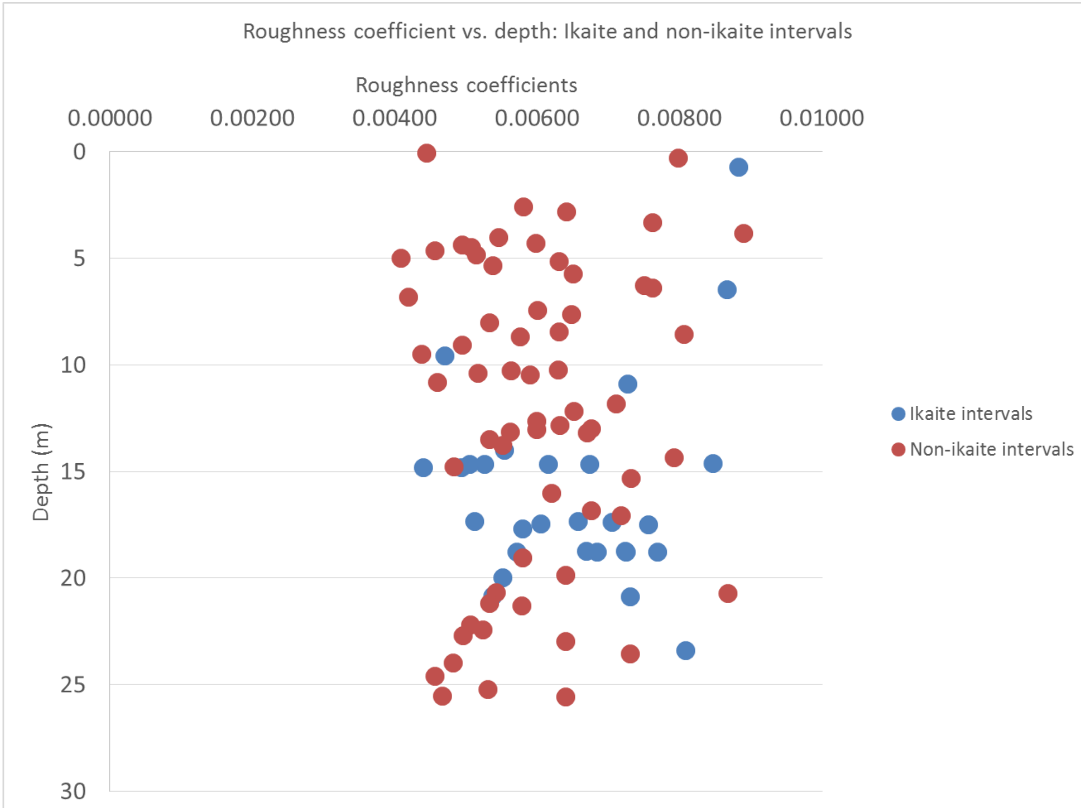

Figure 38: Comparison between roughness coefficient and depth in ikaite and non-ikaite intervals.

However, some grains do show evidence of glacial, aeolian, or current influence. They are shown in a cross-cutting relationship on the grains (Figure 27; Figure 28; Figure 29, respectively). The majority of the transport mechanisms are glacial. The rough, grinding transport that the grains experience by glaciers disrupts the mineral lattices, which increases dissolution rates and increases the surface area (Anderson et al., 1997). The majority of grains show some evidence of glacial transport. However, some do show evidence of aeolian and current microtextures. In Unit 1, only three intervals represent aeolian transport mechanism (Figure 33). One of the intervals is an ikaite interval. In Unit

2, three intervals represent an aeolian transport mechanism, and two intervals represent an equal abundance of aeolian and current transport (Figure 33).

Because the majority of grains have been exposed to glacial grinding, they are weak and vulnerable to chemical precipitation and chemical solutions which partially erased the majority of their surface. The high concentration of siliceous ooze on the seafloor allowed for the precipitation of silica. According to Krauskopf (1956), the precipitation of silica from a solution supersaturated in silica can occur very quickly, from several days to a few weeks. This suggests that the silica precipitated quickly and in-situ at the Perseverance Drift. Grains with abundant silica precipitation have been observed in Antarctica before (Narayana et al., 2010).

A slight trend arises when silica precipitation and depth were compared (Figure 39). All intervals sampled above 10m show a high silica precipitation range from 56-93%. From 10m to the base of the core, there is a variable silica precipitation range from 68-100%. This general trend suggests that silica precipitation decreases down-core. Interval 0.29-0.30m even shows evidence of some percentage of grains not having any silica precipitation. There is no drastic difference between ikaite and non-ikaite intervals. The ikaite intervals have a range of high silica precipitation from 67-100%, while the non-ikaite intervals have a range of high silica precipitation from 56-100%.

This suggests that although silica precipitation happens quickly, some of the intervals of younger, shallower sediment have yet to have a full 100% of all grains covered in high silica precipitation. The older sediment down-core show eight intervals of 100% of grains covered in high silica precipitation. Five of those intervals contain ikaite. The addition of SiO_2 into the sediment, along with terrestrial iron, could trigger the formation of ikaite.

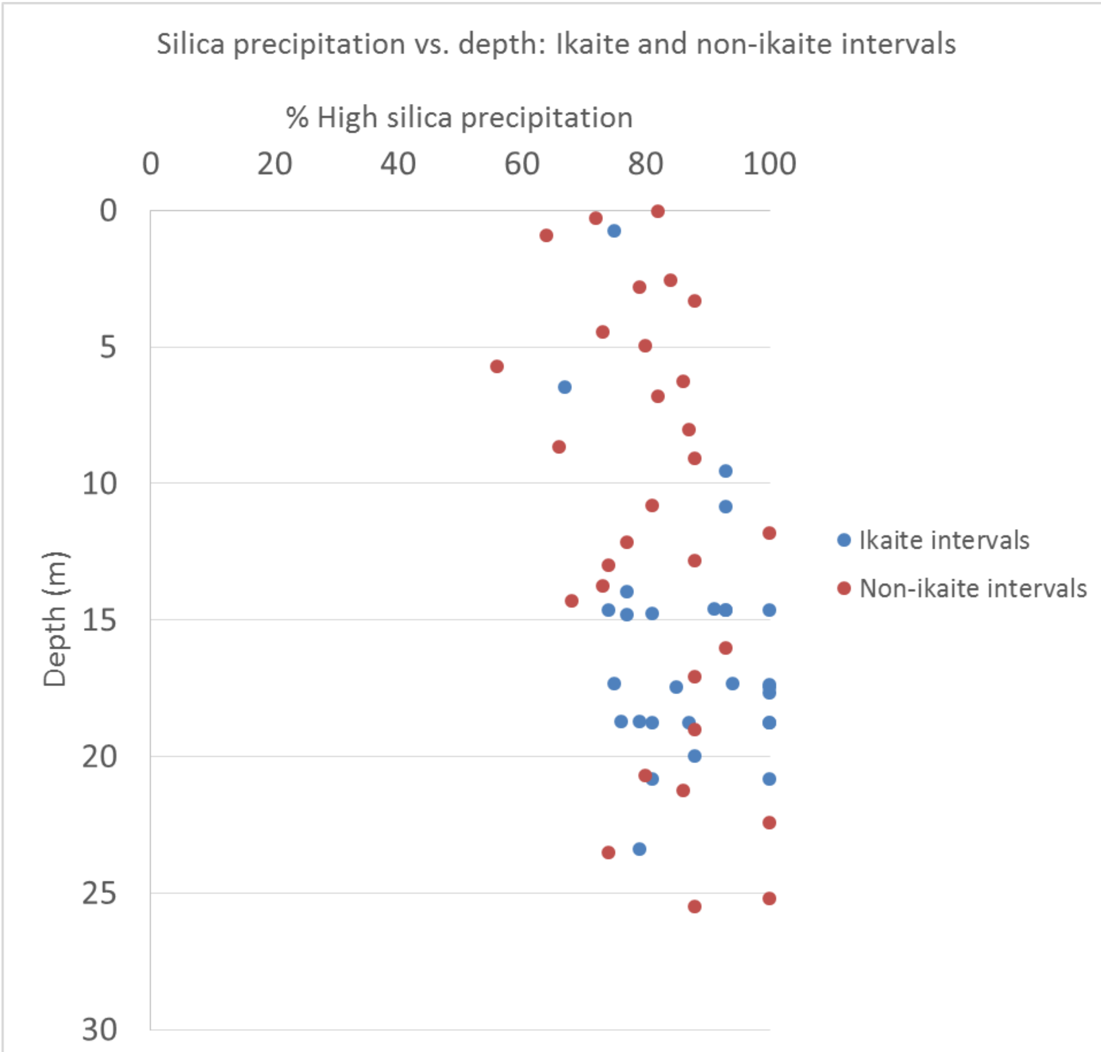

Figure 39: A comparison of silica precipitation versus depth.

The Perseverance Drift's high, continuous biogenic productivity through time makes it a unique area of study. The contribution of some iron-rich terrigenous grains allows desirable conditions for diatom and result in a "hotspot" of primary productivity.

It is also a site of high chlorophyll-*a* (chl-*a*) concentration (Ardelan et al., 2010). These factors may contribute to the abundant silica precipitation in this notable site.

Conclusions

The analysis of grain size, grain shape, and grain texture at the Perseverance Drift, Antarctica Peninsula reveal slight expressions paleoclimate changes in the northeastern Antarctic Peninsula. Four sediment facies were assigned to NBP1203 JPC36 based on grain size and lithological description. Because of the Perseverance Drift's proximity to land, in all facies there is a delivery of terrigenous sediment by strong winds directly to the site.

Facies 1 shows an influence of strong currents, which deliver high amounts coarse, terrigenous grains to the site. The presence of sea ice provides a place for aeolian, terrigenous grains to land and later be contributed to the site, and therefore, this decreases the percent biogenic sediment. The sand percentage for Facies 1 is ≥20%. Facies 3 is influenced by weaker currents and sea ice allowing for the abundant delivery of terrigenous grains to the site by aeolian processes. The biogenic sediment is decreased because of the presence of interpreted sea ice. Both Facies 1 and 3 are interpreted to be deposited in open marine conditions with varied sea ice coverage.

Facies 2 has less influence of strong currents that deliver lower amounts of coarse, terrigenous material to site. Many coarse, terrigenous grains are delivered via icebergs. The sand percentage is ≥20%. Facies 4 is influenced by weaker currents and input of terrigenous material by ice rafting. There is a high abundance of biogenic sedimentation in both Facies 2 and Facies 4 because of the interpreted warm, open marine environment.

A Neoglacial period, dominated by Facies 1 and Facies 3, is interpreted to be from 1,700- >3,375 cal. yr. BP. A Warm Period, dominated by Facies 2 and Facies 4, is interpreted to be from 1,700 cal. yr. BP to present. The end of the Neoglacial is 100 years apart from the Bransfield Basin in the northwestern Antarctic Peninsula.

The Perseverance Drift has continuous input of iron-rich terrigenous material from aeolian processes. There is no pattern between ikaite intervals and the assigned sediment facies. Because of the constant input of iron-rich terrigenous sediment throughout the core and the processes of phosphate recycling, ikaite can form.

Grain textures at the Perseverance Drift revealed a very high abundance of silica precipitation. The silica precipitation is interpreted to be deposited quickly and in situ. It covers the majority of microtextures that would help interpret the transport history to the site. However, glacial microtextures are the most prominent textures, followed by a small amount of aeolian and current. Because the silica precipitation covered the original grain, the grain shape analysis proved to not be a useful method for determining transport history. Further studies on the seawater chemistry at the Perseverance Drift will allow for a better interpretation of paleoclimate in the northeastern Antarctic Peninsula.

References Cited

Abram, N.J., Mulvaney, R., Wolff, E.W., Triest, J., Kipfstuhl, S., Trusel, L.D., Vimeux, F., Fleet, L., and Arrowsmith C., 2013, Acceleration of snow melt in an Antarctic Peninsula ice core during the twentieth century, Nature Geoscience, Vol. 6, pp. 404-411.

Al-Handal, A. Y., Riaux-Gobin, C., & Wulff, A., 2010, *Cocconeis pottercovei* sp. nov. and *Cocconeis pinnata* var. matsii var. nov., two new marine diatom taxa from King George Island, Antarctica. Diatom Research, Vol. 25 (1), pp. 1-11.

Anderson, J.B., Brake, C.F., and Myers, N.C., 1984, Sedimentation on the Ross Sea Continental Shelf, Antarctica, Marine Geology, Vol. 57, pp. 295-333.

Anderson, J.B., Shipp, S.S., Lowe, A.K., Wellner, J.S., and Mosola, A.B., 2002, The Antarctic Ice Sheet during the Last Glacial Maximum and its subsequent retreat history: a review, Quaternary Science Reviews, Vol. 21, pp. 49-70.

Anderson, J.B., Warny, S., Askin, R.A., Wellner, J.S., Bohaty, S.M., Kirshner, A., E., Livsey, D.N., Simms, A.R., Smith, T.R., Ehrmann, W., Lawver, L.A., Barbeau, D., Wise, S.W., Kulhanek, D.K., Weaver, F.M., Majewski, W., 2011, Progressive Cenozoic cooling and the demise of Antarctica's last refugium, Proceedings of the National Academy of Science, Vol. 108 (39), pp. 11356-11360.

Anderson, S.P., Drever, J.I., and Humphrey, N.F., 1997, Chemical weathering in glacial environments, Geology, Vol. 25, pp. 399-402.

Andrews, J.T., Domack, E.W., Cunningham, W.L., Leventer, A., Licht, K.J., Jull, A.J.T., DeMaster, D.J., Jennings, A.E., 1999, Problems and possible solutions concerning radiocarbon dating of surface marine sediments, Ross Sea, Antarctica, Quaternary Research, Vol. 52, pp. 206-216.

Ardelan, M. V., O. Holm-Hansen, C. D. Hewes, Christian S. Reiss, N. S. Silva, Henrieta Dulaiova, E. Steinnes, and E. Sakshaug, 2010, Natural iron enrichment around the Antarctic Peninsula in the Southern Ocean, Biogeosciences Vol. 7 (1), pp. 11-25.

Armand, L.K., Crosta, X., Romero, O., and Pichon, J.J., 2005, The biogeography of major diatom taxa in Southern Ocean sediments: 1. Sea ice related species, Paleogeography, Paleoclimatology, Paleoecology, Vol. 223, pp. 93-126.

Asthana, R., Shrivastava, P.K., Beg, M.J., Shome, S., and Kachroo, K., 2009, Surface microtextures of quartz grains from glaciolacustrine sediment core from Priyadarshini Lake, Schirmacher Oasis, East Antarctica as revealed under the scanning electron microscope, Indian Journal of Geosciences, Vol. 63, pp. 205-214.

Atkins, C.B., and Dunbar, G.B., 2009, Aeolian sediment flux from sea ice into Southern McMurdo Sound, Antarctica, Global and Planetary Change, Vol. 69, pp. 133-141.

Backman, E., and Domack, E.W., 2003, Depositional architecture and seafloor mapping of the Vega Drift, Erebus and Terror Gulf, Antarctic Peninsula, EOS Trans. AGU, 84, 46, Fall Meeting Supplementary Abstract, PP31B-0256.

Barrand, N.E., Vaughan, D.G., Steiner, N., Tedesco, Kuipers Munneke, P., Van Der Broeke, M.R., and Hosking, J.S., 2013, Trends in Antarctic Peninsula surface melting conditions from observations and regional climate modeling, Journal of Geophysical Research: Earth Surface, Vol. 118, pp. 315-330.

Barrett, P.J., Pyne, A.R., and Ward, B.L., 1983, Modern sedimentation in McMurdo Sound, Antarctica, Australian Academy of Science, Canberra, A.C.T., Antarctic Earth Science, pp. 550-554.

Barnard, A., 2010, Onset of a small but significant regional climate change documented in high-resolution late Holocene sediment cores from the maritime western Antarctic Peninsula, Master's Thesis, University of Houston, pp. 46-59.

Barnard, A., Wellner, J.S., and Anderson, J.B., 2014, Late Holocene climate change recorded in proxy records from Bransfield Basin sediment core, Antarctic Peninsula, Polar Research, Vol. 33, pp. 1-13.

Bartek, L. R., and Anderson, J. B., 199, Facies distribution resulting from sedimentation under polar interglacial climatic conditions within a high-latitude marginal basin, McMurdo Sound, Antarctica, Geological Society of America Special Papers, Vol. 261, pp. 27-50.

Bentley, M.J., Hodgson, D.A., Sugden, D.E., Roberts, S.J., Smith, J.A., O'Cofaigh, C., Domack, E.W., Larter, R.D., Roberts, S.J., Brachfeld, S., Leventer, A., Hjort, C., Hillenbrand, C.-D., Evans, J., 2009, Mechanisms of Holocene paleoenvironmental change in the Antarctic Peninsula region, The Holocene, Vol. 19, pp. 51-69.

Bentley, M.J., O Cofaigh, C., Anderson, J.B., Conway, H., Davies, B., Graham, A.G.C., Hillenbrand, C-D., Hodgson, D.A., Jamieson, S.S.R., Larter, R.D., Makintosh, A., Smith, J.A., Verleyen, Ackert, R.P., Bart, P.J., Berg, S., Brunstein, D., Canals, M., Colhoun, E.A., Crosta, X., Dickens, W.A., Domack, E., Dowdeswell, J.A., Dunbar, R., Glasser, N.F., Gohl, K., Golledge, N.R., Goodwin, I., Gore, D.B., Greenwood, S.L., Hall, B.L., Hall, K., Hedding, D.W., Hein, A.S., Hocking, E.P., Jakobsson, M., Johnson, J.S., Jomelli, V., Jones, R.S., Klages, J.P., Kristofferson, Y., Kuhn, G., Leventer, A., Licht, K., Lilly, K., Lindow, J., Lovingstone, S.J., Masse, G., McGlone, M.S., McKay, R.M., Melles, M., Miura, H., Mulvaney, R., Nel., W., Nitsche, F.O., O'Brian, P.E., Post, A.L., Roberts, S.J., Saunders, K. M., Selkirk, P.M., Simms, A.R., Spiegel, C., Stolldorf, T.D., Sugden, D.E., Van der Putten, N., Van Ommen, T., Verfaillie, D., Vyverman, W., Wagner, B., White, D.A., Witus, A.E., and Zwartz, D., 2014, A community based geological reconstruction of Antarctic Ice Sheet deglaciation since the Last Glacial Maximum, Quaternary Science Reviews, Vol. 100, pp. 1-9.

Bischoff, J.L., Fitzpatrick, J.A., and Rosenbauer, R.J., 1993, The solubility and stabilization of ikaite (CaCO3 6H2O) from 1-25C: Environmental and paleoclimatic implications for Thinolite Tufa, The Journal of Geology, Vol. 101, pp. 21-33.

Brachfeld, S. A., Banerjee, S. K., Guyodo, Y., & Acton, G. D., 2002, A 13,200 year history of century to millennial-scale paleoenvironmental change magnetically recorded in the Palmer Deep, Western Antarctic Peninsula, Earth and Plantery Science Letters, Vol. 194, pp. 311-326.

Buffen, A., Leventer, A., Rubin, A., and Hutchins, T., 2007, Diatom assemblages in surface sediments of the northwestern Weddell Sea, Antarctic Peninsula, Marine Micropaleontology, Vol. 62, pp. 7-30.

Camerlenghi, A., Domack, E.W., Rebesco, M., Gilbert, R., Ishman, S., Leventer, A., Brachfeld, S., and Drake, A., 2001, Glacial morphology and post-glacial contourites in northern Prince Gustav Channel (NW Weddell Sea, Antarctica), Marine Geophysical Researches, Vol. 22, pp. 417-433.

Charpentier, I., Sarocchi, D., and Sedano, L.A.R., 2013, Particle shape analysis of volcanic clast samples with the Matlab tool MORPHEO, Computers and Geosciences, Vol. 51, pp. 172-181.

Chewings, J.M., Atkins, C.B., Dunbar, G.B., and Golledge, N.R., 2014, Aeolian sediment transport deposition in a modern high latitude glacial marine environment, Sedimentology, Vol. 61, pp. 1535-1557.

Clark, P.U., Dyke, A.S., Shakun, J.D., Carlson, A.E., Clark, J., Wohlfarth, B., Mitrovica, J.X., Hostetler, S.W., and McCabe, A.M., 2009, The Last Glacial Maximum, Science, Vol. 325, pp. 710-714.

Cook, A.J., Fox, A.J., Vaughan, D.G., and Ferrigno, J.G., 2005, Retreating glacier fronts on the Antarctic Peninsula over the past half-century, Science, Vol. 308, pp. 541-544. doi: 10.1126/science. 110423.

Cook, A.J., and Vaughan, D.G., 2009, Overview of areal changes of the ice shelves on the Antarctic Peninsula over the past 50 years, The Cryosphere Discussions, Vol. 3, pp. 579-630.

Cooper, M., and Leventer, A., 2005, *Thalassisosira anarctica* records of recent warming in the Antarctic Peninsula, Colgate University Geology 440 Seminar, unpublished data.

Crosta, X., Romero, O., Armand, L.K., and Pichon, J.J., 2005, The biogeography of major diatom taxa in Southern Ocean sediments: 2, Open ocean related species, Paleogeography, Paleoclimatology, Paleoecology, Vol. 223, pp. 66-92.

Cunningham, W.L., Andrews, J.T., Jennings, A.E., Licht, K.J., and Leventer, A., 1999, Late Pleistocene- Holocene marine conditions in the Ross Sea Antarctica: evidence from the diatom record, Holocene, Vol. 9, pp 129-140.

Darby, D.A., Burckle, L.H., and Clark, D.L., 1974, Airborne dust on the Arctic pack ice, its composition and fallout rate, Earth and Planetary Science Letters, Vol. 24, pp. 166-172.

DeMaster, D.J., Nelson, T.M., Harden, S.L., and Nittrouer, C.A., 1991, The cycling and accumulation of biogenic silica and organic carbon in Antarctic deep-sea and continental margin environments, Marine Chemistry, Vol. 35, pp. 489-502.

DeMaster, D.J., 2002, The accumulation and cycling of biogenic silica in the Southern Ocean: revisiting the marine silica budget, Deep-Sea Research, Part III, Topical Studies in Oceanography, Vol. 49, pp. 3155-3167.

Dixit, S., Van Cappellen, P., and Van Bennekom, A.J., 2001, Processes controlling solubility of biogenic silica and porewater buildup of silicic acid in marine sediments, Marine Chemistry, Vol. 73, pp. 333-352.

Domack, E.W. and McClennen, C.E., 1996, Accumulation of glaciomarine sediments in fjords of the Antarctic Peninsula and their use as late Holocene paleonvironmental indicators, in: Ross, R., Quetin, L. (Eds.), *Foundations of Ecosystem Research West of the Antarctic Peninsula*, Antarctic Research Series, Vol. 70, AGU, Washington, DC, pp. 135-154.

Domack, E.W., Leventer, A., Dunbar, R., Taylor, F., Brachfeld, S., Sjunneskog, C., and ODP Leg 178 Scientific Party, 2001, Chronology of the Palmer Deep site, Antarctic Peninsula: A Holocene paleoenvironmental reference for the circum-Antarctic, Holocene, Vol. 11, pp. 1-9.

Domack, E.W., 2002, A synthesis for site 1098: Palmer Deep, In Barker, P.F., Camerlenghi, A., Acton, G.D., and Ramsay, A.T.S., editors, *Proceedings of the ocean drilling program, scientific results, Ocean Drilling Program*, Texas A & M University, College Station, TX.

Domack, E.W., Leventer, A., Root, S., Ring, J., Williams, E., Carlson, D., Hirshorn, E., Wright, W., Gilbert, R., and Burr, G., 2003, Marine sedimentary record of natural environmental variability and recent warming in the Antarctic Peninsula, In Domack, E.W., Leventer, A., Burnett, A., Bindschadler, R., Convery, P., and Kirby, M., editors, *Antarctic Peninsula Climate Variability: Historical and Paleoenvironmental Perspectives*, Antarctic Research Series 79, American Geophysical Union, pp. 205-222.

Domack, E., Duran, D., Leventer, A., Ishman, S., Doane, S., McCallum, S., Amblas, D., Ring, J., Gilbert, R., and Prentice, M., 2005, Stability of the Larsen B ice shelf on the Antarctic Peninsula during the Holocene epoch, Nature, Vol. 436, pp. 681-685.

Domack, E. W., Halverson, G., Willmott, V., Leventer, A., Brachfeld, S., and Ishman, S., 2007, Spatial and temporal distribution of ikaite crystals in Antarctic glacial marine sediments. *US Geological Survey and The National Academies*.

Ding, Q., Steig, E.J., Battisti, D.S., and Kuttel, M., 2011, Winter warming in West Antarctica caused by central tropical Pacific warming, Nature Geoscience, Vol. 4, pp. 398- 403.

Ducklow, H.W., Baker, K., Martinson, D.G., Quetin, L.B., Ross, R.M., Smith, R.C., Stammerjohn, S.E., Vernet, M., and Fraser, W., 2007, Marine pelagic ecosystems: the West Antarctic Penisnula, Philosphical Transactions of the Royal Society: Biological Sciences, Vol. 362, pp. 67-94.

Dunbar, R.B., Dehn, M., and Leventer, A., 1985, Distribution of biogenic components in surface sediments from the Antarctic continental shelf, Antarctic Journal of the United States, Vol. 19, pp. 71-73.

Dunbar, R.B., Leventerm A., and Stockton, W.L., 1989, Biogenic sedimentation in McMurdo Sound, Antarctica, Marine Geology, Vol. 85, pp. 155-179.

Ehrlich, R., and Weinberg, B., 1970, An exact methods for characterization of grain shape, Journal of Sedimentary Petrology, Vol. 40, No. 1, pp. 205-212.

Ehrlich, R., Brown, P.J., Yarus, J.M., and Przygocki, R.S., 1980, The origin of shape frequency distributions and the relationship between size and shape, Journal of Sedimentary Petrology, Vol. 50 (2), pp. 475-484.

Faugeres, J.-C., Stow, D.A.V., Imber, P., and Viana, A., 1999, Seismic features diagnostic of contourite drifts, Marine Geology, Vol. 162, pp. 1-38.

Franzke, C., 2013, Significant reduction of cold temperature extremes at Faraday/ Vernadsky station in the Antarctic Peninsula, International Journal of Climatology, Vol. 33, pp. 1070-1078.

Fryxell, G.A., Kang, S.-H., and Ashworth, T.K., 1989, AMERIEZ 1988 and ODP Leg 119, Antarctic phytoplankton summer and winter stage indicators, Antarctic Journal, US, Vol. 24, pp. 156-157.

Füchtbauer, H., 1988, Sediment Petrologie Teil II, *Sedimente und Sedimentgesteine*, 4. Auflage.—1141 S., 660 Abb. 113 Tab.

Gibson, J.A.E., Trull, T., Nichols, P.D., Summons, R.E., and McMinn, A., 1999, Sedimentation of 13C-rich organic matter from Antarctic sea ice algae: A potential indicator of past sea ice extent, Geology, Vol. 27, pp. 331-334.

Haines, J., and Mazzullo, J., 1988, The original shapes of quartz silt grains: A test of the validity of the use of quartz grain shape analysis to determine the sources of terrigenous silt in marine sedimentary deposits, Marine Geology, Vol. 78, pp. 227-240.

Harris, P.T., 2000, Ripple cross-laminated sediments on the East Antarctic Shelf: Evidence for episodic bottom water production during the Holocene?, Marine Geology, Vol. 170, pp. 317-330.

Harris, P.T., Brancolini, G., Armand, L., Busetti, M., Beaman, R.J., Giorgetti, G., Presti, M., and Trincardi, F., 2001, Continental shelf drift deposit indicates non-steady state Antarctic bottom water production in the Holocene, Marine Geology, Vol. 179, pp. 1-8.

Hellmer, H.H., Huhn, O., Gomis, D., and Timmermann, R., 2011, On the freshening of the northwestern Weddell Sea continental shelf, Ocean Science, Vol. 7, pp. 305-316.

Hernandez-Molina, F.J., Larter, R.D., Rebesco, M., and Maldonado, A., 2006, Miocene reversal of bottom water flow along the Pacific Margin of the Antarctic Peninsula: Stratigraphic evidence from a contourite sedimentary tail, Marine Geology, Vol. 228, pp. 93-116.

Heroy, D.C., and Anderson, J.B., 2005, Ice-sheet extent of the Antarctic Peninsula region during the Last Glacial Maximum (LGM): Insights from glacial geomorphology, Geological Society of America Bulletin, Vol. 117, pp. 1497-1512.

Heroy, D.C. and Anderson, J.B., 2007, Radiocarbon constraints on the Antarctic Peninsula Ice Sheet retreat following the Last Glacial Maximum (LGM), Quaternary Science Reviews, Vol. 26, pp. 3289-3297.

Hillenbrand, C.-D., Kuhn, G., and Fredrichs, T., 2009, Record of Mid-Pleistocene depositional anomaly in West Antarctic continual margin sediments: and indicator for ice-sheet collapse?, Quaternary Science Reviews, Vol. 28, pp. 1147-1159.

Hodgson, D.A., Bentley, M.J., Roberts, S.J., Smith, J.A., Sugden, D.E., and Domack, E.W., 2006, Examining Holocene stability of Antarctic Peninsula ice shelves, EOS Transactions, American Geophysical Union, Vol. 87, pp. 305-312.

Hofmann, E.E., Klinck, J.M., Lascara, C.M., and Smith, D.A., 1996, Water mass distribution and circulation west of the Antarctic Peninsula and including Bransfield Strait, Foundations for ecological research west of the Antarctic Peninsula Antarctic Research Series, Vol. 70, pp. 61-80.

Hughes, P., and Krissek, L.A., 1985, Modern sediments of the Terra Nova Bay polynya, Ross Sea, Antarctica, Antarctic Journal, Vol. 20, pp. 107-108.

Ishman, S.E., and Domack, E.W., 1994, Oceanographic controls on the benthic foraminifers from the Bellinghausen margin of the Antarctic Peninsula, Marine Micropaleontology, Vol. 24, pp. 119-155.

Jacobs, S.S., Jenkins, A., Giulivi, C.F., and Dutrieux, P., 2011, Stronger ocean circulation and increased melting under Pine Island Glacier ice shelf, Nature Geoscience, Vol. 4, pp. 519-523.

Khim, B., Yoon, H.I., Kang, C.Y., and Bhak, J.J., 2002, Unstable climatic oscillations during the late Holocene in the eastern Bransfield Basin, Antarctic Peninsula, Quaternary Research, Vol. 58, pp. 234-245.

Khim, B.K., Kim, D., Shin, H.C., and Kim, D.Y., 2005, Stable carbon and nitrogen isotopes of sinking particles in the eastern Bransfield Strait (Antarctica), Ocean Science Journal, Vol. 40, pp. 167-176.

Kirshner, A. E., & Anderson, J. B., 2011, Cenozoic Glacial History of the Northern Antarctic Peninsula: a micromorphological investigation of quartz sand grains, *Tectonic, Climatic, and Cryospheric Evolution of the Antarctic Peninsula*, pp. 153-165.

Klinck, J.M., Hofmann, E.E., Beardsley, R.C., Salihoglu, B., and Howard, S., 2004, Water-mass properties and circulation on the west Antarctic Peninsula continental shelf in austral fall and winter 2001, Deep Sea Research Part II- Tropical Studies in Oceanography, Vol. 51, pp. 1925-1946.

Krauskopf, K.B., Dissolution and precipitation of silica at low temperatures, Geochimica et Cosmochimica Acta, Vol. 10, pp. 1-26.

Krinsley, D. H., 1971, 30. Surface features of quartz sand grains from Leg 18 of The Deep Sea Drilling Project, *Deep Sea Drilling Result Project Results and Publications*, Vol. 18, pp. 925-933.

Lannuzel, D., Schoemann, V., de Jong, J.T.M., Tison, J.L., and Chou, L., 2007, Distribution and biogeochemical behavior of iron in the East Antarctic sea ice, Marine Chemistry, Vol. 106, pp. 18-32.

Laluraj, C. M., Thamban, M., & Satheesan, K., 2014, Dust and associated geochemical fluxes in a firn core from coastal East Antarctica and its linkages with Southern Hemisphere climate variability over the last 50 years, Atmospheric Environment, Vol. 90, pp. 23-32.

Leventer, A., Domack, E. W., Ishman, S. E., Brachfeld, S., McClennen, C. E., & Manley, P., 1996, Productivity cycles of 200–300 years in the Antarctic Peninsula region: understanding linkages among the sun, atmosphere, oceans, sea ice, and biota. Geological Society of America Bulletin, Vol. 108(12), pp. 1626-1644.

Leventer, A., 1998, The Fate of Antarctic "Sea Ice Diatoms" and Their Use as Paleoenvironmental Indicators, in *Antarctic Sea Ice: Biological Processes, Interactions and Variability* (eds M. P. Lizotte and K. R. Arrigo), American Geophysical Union, Washington, D. C.. doi: 10.1029/AR073p0121

Leventer, A., Domack, E., Barkoukis, A., McAndrews, B., and Murray, J, 2002, Laminations from the Palmer Deep: A diatom-based interpretation, Paleoceanography, Vol. 17 (3), pp. 3-15.

Livsey, D.N., Simms, A.R., Clary, W.G., Wellner, J.S., Anderson, J.B., and Chandler, J.P., 2013, Fourier grain-shape analysis of Antarctic marine core: The relative influence of provenance and glacial activity on grain shape, Journal of Sedimentary Research, Vol. 83, pp. 80-90.

Lu, Z., Rickaby, R.E.M., Kennedy, H., Kennedy, P., Pancost, R.D., Shaw, S., Lennie, A., Wellner., J., and Anderson, J., 2012, An ikaite record of late Holocene climate at the Antarctic Peninsula, Earth and Planetary Science Letters, Vol. 325-326, pp. 108-115.

MacAyeal, D.R., 1992, Irregular oscillations of the West Antarctic Ice Sheet, Nature, Vol. 359, pp. 29-32.

Maddison, E.J., Pike, J., Leventer, A., and Domack, E., 2005, Deglacial seasonal and sub-seasonal diatom record from Palmer Deep, Antarctica, Journal of Quaternary Science, Vol. 20, pp. 435-446.

Madhavaraju, J., Barragan, J.C.G., Hussain, S.M., and Mohan, S.P., 2009, Microtextures on quartz grains in the beach sediments of Puerto Penasco and Bahia Kino, Gulf of California, Sonora, Mexico, Revista Mexicana de Ciencias Geologicas, Vol. 26, pp. 367-379.

Mahaney, W.C., 1995, Pleistocene and Holocene glacier thicknesses, transport histories, and dynamics inferred from SEM microtextures on quartz particles, Boreas, Vol. 24, pp. 293-304.

Mahaney, W. C., 2002, *Atlas of Sand Grain Surface Textures and Applications*, Oxford University Press, Oxford, United Kingdom.

Majewska, R., Gambi, M. C., Totti, C. M., Pennesi, C., & De Stefano, M., 2013, Growth form analysis of epiphytic diatom communities of Terra Nova Bay (Ross Sea, Antarctica), Polar biology, Vol. 36 (1), pp. 73-86.

Majewski, W., Wellner, J.S., Szczucinski, W., and Anderson, J.B., 2012, Holocene oceanographic and glacial changes recorded in Maxwell Bay, West Antarctica, Marine Geology, Vol. 326-328, pp. 67-79.

Mashiotta, T.A., 1992, Biogenic sedimentation in Andvord Bay, Antarctica: A 3,000 year record of paleoproductivity, Bachelors of Arts Thesis, Hamilton College, p. 72.

Mazzullo, J., and Ritter, C., 1991, Influence of sediment source on the shapes and surface textures of glacial quartz sand grains, Geology, Vol. 19, pp. 384-388.

McConnell, J.R., Aristarain, A.J., Banta, J.R., Edwards, P.R., and Simoes, J.C., 2007, 20th century doubling in dust archived in an Antarctic Peninsula ice core parallels climate change and desertification in South America, PNAS, Vol. 104, pp. 5743-5748.

Meredith, M.P. and King, J.C., 2005, Rapid climate change in the ocean west of the Antarctic Peninsula during the second half of the 20th century, Geophysical Research Letters, Vol. 32, L19604.

Michalchuk, B.R., Anderson, J.B., Wellner, J.S., Manley, P.L., Majewski, W., and Bohaty, S., 2009, Holocene climate and glacial history of the northeastern Antarctic Peninsula: the marine sedimentary record from a long SHALDRIL core, Quaternary Science Reviews, Vol. 28, pp. 3049-3065.

Milliken, K.T., Anderson, J.B., Wellner, J.S., Bohaty, S.M., and Manley, P.L., 2009. High-resolution climate record from Maxwell Bay, South Shetland Islands, Antarctica, Geological Society of America Bulletin, Vol. 11/12, pp. 1711-1725.

Morris, E. M., and Vaughan, D. G., 2003, *Spatial and temporal variation of surface temperature on the Antarctic Peninsula and the limit of viability of ice shelves*, American Geophysical Union, pp. 61-68.

Murillo-Jimenez, J.M., Full, W., Nava-Sanchez, E.H., Camacho-Valdez, V., and Leon-Manilla, A., 2007, Sediment sources of beach sand from the southern coast of the Baja California Peninsula, Mexico- Fourier grain shape analysis, Geological Society of America Special Paper, Vol. 420, pp. 297-318.

Mulvaney, R., Abram, N.J., Hindermarsh, R.C.A., Arrowsmith, C., Fleet, L., Triest, J., Sime, L.C., Alemany, O., and Foord, S., 2012, Recent Antarctic Peninsula warming relative to Holocene climate and ice-shelf history, Nature, Vol. 489, pp. 141-145.

Narayana, A.C., Mohan, R., Mishra, R., 2010, Morphology and surface textures of quartz grains from freshwater lakes of McLeod Island, Larsemann Hills, East Antarctica, Current Science, Vol. 99, pp. 1420-1425.

Naveira Garabato, A.C., Heywood, K.J., and Stevens, D.P., 2002, Modification and pathways of Southern Ocean Deep Waters in the Scotia Sea, Deep Sea Research, Vol. 49, pp. 681-705.

Nelson, D.M., and Gordon, L.I., 1982, Production and pelagic dissolution of biogenic silica in the Southern Ocean, Geochimia Cosochimia Acta, Vol. 46, pp. 491-500.

Nelson, D.M., Ahren, J.A., and Herlihy, L.J., 1991, Cycling of biogenic silica within the upper water column of the Ross Sea, Marine Chemistry, Vol. 35, pp. 461-476.

Nelson, D.M., Treguer, P., Brzezinski, M.A., Leynaert, A., and Queguiner, B., 1995, Production and dissolution of biogenic silica in the ocean: revised global estimates, comparison with regional data and relationship to biogenic sedimentation, Global Biogeochemical Cycles, Vol. 9, pp.359-372.

Nelson, D.M., and Brzezinski, M.A., 1997, Diatom growth and productivity in oligotrophic midocean gyre: a 3 year record from the Saragasso Sea near Bermuda, Limnol. Oceanography, Vol. 42, pp. 473-486.

Ó Cofaigh, Colm., Bethan J. Davies, Stephen J. Livingstone, James A. Smith, Joanne S. Johnson, Emma P. Hocking, Dominic A. Hodgson, Anderson, J.B., Bentley, M.J., Canals, M., Domack, E.W., Dowdeswell, J.A., Evans, J., Glasser, N.F., Hillenbrand, C-D., Larter, R.D., Roberts, S.J., and Simms, A., 2014, Reconstruction of ice-sheet changes in the Antarctic Peninsula since the Last Glacial Maximum, Quaternary Science Reviews, Vol. 100, pp. 87-110.

Orsi, A.H., Whitworth III, T., and Nowlin Jr., W.D., 1995, On the meridional extent and fronts of the Antarctic circumpolar current, Deep Sea Research, Vol. 42. No. 5, pp. 641-673.

Parish, T. R., and Bromwich, D. H., 1998, A case study of Antarctic katabatic wind interaction with large-scale forcing, Monthly Weather Review, Vol. 126 (1), pp. 199-209.

Perez, R. B., Brachfeld, S., Gorring, M., Leventer, A., Maritz, J., Domack, E. W., and Gilbert, R., 2005, Geochemical and rock-magnetic analyses of kasten cores from the Joinville-d'Urville Trough, Northeastern Antarctic Peninsula: Results and correlation with the Western Antarctic Peninsula, in AGU 2005 Fall Meeting Abstracts, Vol. 1, p. 624.

Pike, J., Crosta, X., Maddison, E.J., Stickley, C.E., Denis, D., Barbara, L., and Renssen, H., 2009, Observations on the relationship between Antarctic coastal diatoms *Thalassiosira Antarctica* Comber and *Porosira glacialis* (Grunow) Jorgensen and sea ice concentrations during the Late Quaternary, Marine Micropaleontology, Vol. 73, pp. 14-25.

Pittman, E.D., 1972, Diagensis of quartz in sandstones as revealed by scanning electron microscopy, Journal of Sedimentary Petrology, Vol. 42 (3), pp. 507-519.

Pudsey, C.J., and Evans, J., 2001, First survey of Antarctic sub-ice shelf sediments reveals mid-Holocene ice shelf retreat, Geology, Vol. 29, pp. 787-790.

Raiswell, R., Benning, L.G., Tranter, M., and Tulaczyk, S., 2008, Bioavailable iron in the Southern Ocean: the significance of the iceberg conveyor belt, Geochemical Transactions, Vol. 9, p. 7.

Rau, G.H., Sullivan, C.W., and Gordon, L.I., 1991, δ^{13}C and δ^{15}C variations in Weddell Sea particulate organic matter, Marine Chemistry, Vol. 35, pp. 359-369.

Renwick, J.A., 2005, Persistent positive anomalies in the Southern Hemisphere Circulation, American Meteorological Society, Vol. 133, pp. 977-988.

Reynolds, J.M., 1981, The distribution of mean annual temperatures in the Antarctic Peninsula, British Antarctic Survey Bulletin, No. 54, pp. 123-133.

Rickaby, R.E.M., Shaw, S., Bennitt, G., Kennedy, H., Zabel, M., and Lennie, A., 2006, Potential of ikaite to record the evolution of oceanic δ^{18}O, Geology, Vol. 34, pp. 497-500.

Pritchard, H.D., Ligtenberg, S.R.M., Fricker, H.A., Vaughan, D.G., Van Den Broeke, M.R., and Padman, L., 2012, Antarctic ice-sheet loss driven by basal melting of ice shelves, Nature, Vol. 484, pp. 502-505.

Sedwick, P.N., and DiTullio, G.R., 1997, Regulation of algal blooms in Antarctic shelf waters by the release of iron from melting sea ice, Geophysical Research Letters, Vol. 24, pp. 2515-2518.

Sedwick, P.N., DiTullio, G.R., and Mackey, D.J., 2000, Iron and manganese in the Ross Sea, Antarctica: seasonal iron limitation in Antarctic shelf waters, Journal of Geophysical Research, Vol. 105, pp. 11321-11336.

Selleck, B.W., Carr, P.F., and Jones, B.G., 2011, A review and synthesis of glenodonites (pseudomorphs after ikaite) with new data: assessing applicability as recorders of ancient coldwater conditions, Journal of Sedimentary Research, Vol. 77, pp. 980-991.

Sharp, M., and Gomez, B., 1986, Processes and debris comminution in the glacial environment and implications for quartz sand-grain micromorphology, Sedimentary Geology, Vol. 46, pp. 33-47.

Shen, Z.X., Cao, J.J., Zhang, X.Y., Arimoto, R., Ji, J.F., Balsam, W.L., Wang, Y.Q., Zhang, R.J., and Li, X.X., 2006, Spectroscopic analysis of iron-oxide minerals in aerosol particles from northern China, Science of the Total Environment, Vol. 367, pp. 899-907.

Shevenell, A. E., Domack, E. W., and Kernan, G. M., 1996, Record of Holocene palaeoclimate change along the Antarctic Peninsula: evidence from glacial marine sediments, Lallemand Fjord, *Papers and Proceedings of the Royal Society of Tasmania*, Vol. 130 (2), pp. 55-64.

Shevenell, A., and Kennett, J.P., 2002, Antarctic Holocene climate change: A benthic foraminiferal stable isotope record from Palmer Deep, Paleoceanography, Vol. 17, pp. 1-12.

Sjunneskog, C. and Taylor, F., 2002, Postglacial marine diatom record of the Palmer Deep, Antarctic Peninsula (ODP Leg 178, Site 1098) 1. Total diatom abundance, Paleoceanography, Vol. 17 (3), pp. 1-8.

Slomp, C.P., Van der Gaast, S.J., and Van Raaphorst, W., 199, Phosphorous binding by poorly crystalline iron oxides in North Sea sediments, Marine Chemistry, Vol. 52, pp. 55-73.

Steig, E.J., Schneider, D.P., Rutherford, S.D., Mann, M.E., Comiso, J., and Sindell, D., 2009, Warming of the Antarctic ice-sheet surface since the 1957 International Geophysical Year, Nature, Vol. 457, pp. 459-462.

Suess, E., Balzer, Hesse, K.-F., Muller, P.J., Ungerer, C.A., and Wefer, G., 1982, Calcium carbonate hexahydrate from organic-rich sediments of the Antarctic shelf: Precursors to glendonites, Science, New Series, Vol. 216, No. 4550, pp. 1128-1131.

Sweet, D. E., and Soreghan, G.S., 2010, Application of quartz sand microtextureal analysis to infer cold-climate weathering for the Equatorial Fountain Fromation (Pennsylvanian-Permian, Colorado, USA, Journal of Sedimentary Research, Vol. 80, pp. 666-677.

Taylor, F., Whitehead, J.M., and Domack, E., 2001, Holocene paleoclimate change in the Antarctic Peninsula: evidence from the diatom, sedimentary, and geochemical record, Marine Micropaleontology, Vol. 41, pp. 25-43.

Taylor, F., and Sjunneskog, C., 2002, Postglacial marine diatom record of the Palmer Deep, Antarctic Peninsula (ODP Leg 178, Site 1098) 1. Total diatom abundance, Paleoceanography, Vol. 17 (3), pp. 1-8.

Tokarczyk, R., 1987, Classification of water masses in the Bransfield Strait and southern part of the Drake Passage using a method of statistical multidimensional analysis, Polish Polar Research, Vol. 8, pp. 333-366.

Tregeur, P., Nelson, D.M., Van Bennekom, A.J., DeMaster, D.J., Leynart, A., Queguiner, B., 1995, The silica balance in the world ocean: a re-estimate, Science, Vol. 268, pp. 375-379.

Turner, J., Colwell, S.R., Marhsall, G.J., Lachlan-Cope, T.A., Carleton, A.M., Jones, P.D., Lagun, V., Reid, P.A., and Iagovkina, S., 2005, Antarctic climate change during the last 50 years, International Journal of Climatology, Vol. 25, pp. 279-294.

Vadman, K., 2014, Diatom record for the Perseverance Drift, Antarctic Peninsula, Bachelor’s of Art Thesis, Colgate University, pp. 16-32.

Van Cappellen, P., and Qiu, L., 1997, Biogenic silica dissolution in sediments of the Southern Ocean, I Solubility, Deep Sea Research II, Vol. 44, pp. 1109-1128.

Van Ommen, Tas, 2013, Antarctic response, Nature Geoscience, Vol. 6, pp. 334-335.

Vaughan, D. G., and C. S. M. Doake, 1996, Recent atmospheric warming and retreat of ice shelves on the Antarctic Peninsula, Nature, Vol. 379, pp. 328-331.

Vaughan, D.G., Marshall, G.J., Connolley, W.M., Parkinson, C., Mulvaney, R., Hodgson, D.A., King, J.C., Pudsey, C.J., Turner, J., 2003, Recent rapid climate warming on the Antarctic Peninsula, Climate Change, Vol. 60, pp. 243-274.

Vaughan D.G., 2006, Recent trends in melting conditions on the Antarctic Peninsula and their implications for ice-sheet mass balance and sea level, Arctic, Antarctic, and Alpine Research, Vol. 38, pp. 147-152.

Villareal, T.A. and Fryxell, G.A., 1983, Temperature effects on the valve structure of the bipolar diatoms *Thalassiosira Antarctica* and *Porosira glacialis*, Polar Biology, Vol. 2 (3), pp. 163-169.

Villinski, J.C., Dunbar, R.B., and Mucciarone, D.A., 2000, Carbon 13/Carbon 12 ratios of sedimentary organic matter from the Ross Sea, Antarctica: A record of phytoplankton bloom dynamics, Journal of Geophysical Research, Vol. 105, pp. 14, 163-14, 172.

Von Gyldenfeldt, A.-B., Fahrbach, E., Garcia, M.A., and Schroder, M., 2002, Flow variability at the tip of the Antarctic Peninsula, Deep Sea Research, Vol. 49, pp. 4743-4766.

Warner, N.R., and Domack, E.W., 2001, Millenial- to decadal paleoenvironmental change during the Holocene in the Palmer Deep, Antarctica, as recorded by particle size analysis, Paleoceanography, Vol. 17, pp. 1-14.

Wellner, J. S., Anderson, J. B., Ehrmann, W., Weaver, F. M., Kirshner, A., Livsey, D., and Simms, A. R., 2011, History of an evolving ice sheet as recorded in SHALDRIL cores from the northwestern Weddell Sea, *Antarctica.Tectonic, Climatic, and Cryospheric Evolution of the Antarctic Peninsula*, pp. 131-151.

Wentworth, C.K., 1922, A scale of grade and class terms for clastic sediments, The Journal of Geology, Vol. 30, pp. 377-392.

Wright, W., 2000, The Schollaert Sediment Drift: An ultra-high resolution paleoenvironmental archive in the Gerlache Strait, Antarctica, Bachelor's of Arts Thesis, Hamilton College, p. 128.

Zhou, X., Lu., Z., Rickaby, R.E.M., Domack, E.W., Wellner, J.S., and Kennedy, H.A., *in press*, Ikaite abundance controlled by porewater phosphorus level: implications for extensive glendonite deposits, Earth and Planetary Science Letters.

Appendix 1: Data and Results

Sample name	<4µm	4-8µm	8-16µm	16-32µm	32-63µm	> 63µm
NBP1203 JPC36 0.01-0.02mb	9.485	12.84	18.536	18.521	21.235	19.383
NBP1203 JPC36 0.02-0.03m	11.719	11.918	17.073	17.735	20.411	21.145
NBP1203 JPC36 0.04-0.05m	11.061	10.649	15.037	17.661	21.153	24.44
NBP1203 JPC36 0.06-0.07mb	11.18	12.484	18.024	19.679	20.6	18.034
NBP1203 JPC36 0.08-0.09mb	11.659	11.625	16.207	18.819	21.567	20.124
NBP1203 JPC36 0.1-0.11mb	10.791	10.839	16.775	20.357	21.55	19.688
NBP1203 JPC36 0.15-0.16mb	10.901	9.133	14	18.59	21.865	25.511
NBP1203 JPC36 0.2-0.21m	9.609	8.866	13.649	16.864	21.412	29.6
NBP1203 JPC36 0.25-0.26mb	9.053	7.54	11.241	16.382	24.138	31.646
NBP1203 JPC36 0.29-0.3m	9.438	8.51	12.71	16.196	21.504	31.642
NBP1203 JPC36 0.35-0.36m	11.285	11.865	15.927	18.448	20.657	21.819
NBP1203 JPC36 0.4-0.41mb	13.684	14.912	20.344	20.032	16.997	14.031
NBP1203 JPC36 0.45-0.46mb	15.106	16.971	19.879	18.649	16.478	12.916
NBP1203 JPC36 0.5-0.51mb	15.559	18.102	20.636	18.345	16.779	10.579
NBP1203 JPC36 0.55-0.56mc	12.959	24.098	20.594	15.341	18.923	8.085
NBP1203 JPC36 0.6-0.61m	12.005	13.929	18.647	21.516	19.87	14.032
NBP1203 JPC36 0.65-0.66mb	12.902	16.867	19.544	19.934	19.288	11.466
NBP1203 JPC36 0.7-0.71m	11.076	13.019	17.743	20.103	20.086	17.972
NBP1203 JPC36 0.725-0.735m	6.725	9.417	29.137	17.218	25.548	11.955
NBP1203 JPC36 0.75-0.76m	13.096	13.719	16.556	17.267	20.128	19.234
NBP1203 JPC36 0.8-0.81m	14.881	16.1	19.545	17.439	17.406	14.63
NBP1203 JPC36 0.84-0.85mb	15.483	13.663	16.457	17.089	19.048	18.261
NBP1203 JPC36 0.9-0.91mb	15.35	26.832	24.635	12.675	12.305	8.204
NBP1203 JPC36 9.5-9.51m	12.053	18.346	19.41	16.004	17.574	16.613
NBP1203 JPC36 1-1.01m	11.961	13.317	16.838	17.94	18.925	21.018
NBP1203 JPC36 1.04-1.05m	12.682	15.128	18.709	18.412	17.916	17.153
NBP1203 JPC36 1.09-1.1m	12.164	16.142	20.279	18.892	17.621	14.901
NBP1203 JPC36 1.15-1.16mb	15.273	16.437	18.476	18.488	17.882	13.445
NBP1203 JPC36 1.2-1.21m	14.228	16.298	18.546	17.285	17.594	16.049
NBP1203 JPC36 1.81-1.82m Void	0	0	0	0	0	0
NBP1203 JPC36 1.86-1.87m Void	0	0	0	0	0	0
NBP1203 JPC36 1.91-1.92mb	14.784	16.709	18.569	19.623	19.442	10.872
NBP1203 JPC36 1.96-1.97mb	11.937	16.482	17.348	17.9	23.365	12.967
NBP1203 JPC36 2.01-2.02m	15.722	13.733	16.135	19.512	19.773	15.124
NBP1203 JPC36 2.06-2.07m	15.419	19.735	20.211	15.883	16.103	12.648
NBP1203 JPC36 2.11-2.12mb	14.295	14.319	16.201	18.409	19.867	16.908

Figure A1-1: Grain size data for NBP1203 JPC36. Ikaite intervals are highlighted in blue. Table continued on next page.

Sample name	<4µm	4-8µm	8-16µm	16-32µm	32-63µm	> 63µm
NBP1203 JPC36 2.16-2.17mb	17.672	12.17	15.375	17.924	18.649	18.209
NBP1203 JPC36 2.21-2.22mc	17.017	13.24	15.761	16.825	17.386	19.772
NBP1203 JPC36 2.26-2.27m	13.102	12.401	14.874	17.61	20.641	21.372
NBP1203 JPC36 2.31-2.32mb	16.376	16.309	17.593	17.907	18.501	13.314
NBP1203 JPC36 2.36-2.37m	15.626	16.296	18.478	17.605	16.731	15.264
NBP1203 JPC36 2.41-2.42mb	15.463	17.43	18.102	18.926	20.128	9.952
NBP1203 JPC36 2.46-2.47mb	14.215	16.44	16.389	17.64	21.119	14.197
NBP1203 JPC36 2.51-2.52mb	14.975	13.41	15.517	16.998	20.652	18.447
NBP1203 JPC36 2.56-2.57mb	13.503	11.518	15.187	18.493	19.787	21.511
NBP1203 JPC36 2.61-2.62m	14.446	14.745	17.949	19.463	19.625	13.771
NBP1203 JPC36 2.66-2.67m	15.2	13.46	17.335	18.411	17.8	17.795
NBP1203 JPC36 2.71-2.72mb	15.665	16.337	19.067	18.399	17.411	13.122
NBP1203 JPC36 2.76-2.77m	15.428	17.065	18.947	17.346	17.177	14.038
NBP1203 JPC36 2.81-2.82m	14.299	25.43	23.528	13.261	14.3	9.182
NBP1203 JPC36 2.86-2.87mb	13.305	18.145	18.114	16.006	19.889	14.542
NBP1203 JPC36 2.91-2.92m	15.855	12.056	15.269	18.018	19.155	19.646
NBP1203 JPC36 2.96-2.97m	15.159	16.153	18.404	17.295	18.148	14.84
NBP1203 JPC36 3.01-3.02m	14.166	15.908	17.715	17.568	19.265	15.377
NBP1203 JPC36 3.06-3.07m	16.246	16.651	18.535	16.465	16.54	15.562
NBP1203 JPC36 3.11-3.12m	15.875	15.825	18.302	19.218	18.894	11.886
NBP1203 JPC36 3.16-3.17m	15.542	14.654	17.93	19.335	19.096	13.444
NBP1203 JPC36 3.21-3.22m	14.934	13.092	15.593	17.587	19.264	19.53
NBP1203 JPC36 3.26-3.27m	14.977	11.683	15.055	18.846	19.996	19.442
NBP1203 JPC36 3.31-3.32m	16.684	15.04	17.096	17.184	16.891	17.106
NBP1203 JPC36 3.36-3.37m	13.763	15.852	16.864	16.985	20.755	15.782
NBP1203 JPC36 3.41-3.42m	14.031	18.848	21.292	15.809	15.416	14.605
NBP1203 JPC36 3.46-3.47m	12.002	14.072	16.454	17.747	21.645	18.081
NBP1203 JPC36 3.51-3.52m	11.729	13.759	17.219	16.793	18.45	22.049
NBP1203 JPC36 3.56-3.57m	9.799	13.472	18.864	18.059	18.581	21.226
NBP1203 JPC36 3.61-3.62m	10.746	14.119	18.033	17.468	19.349	20.285
NBP1203 JPC36 3.66-3.67mb	10.84	18.682	21.111	18.121	19.387	11.859
NBP1203 JPC36 3.71-3.72m	12.362	27.233	25.541	12.656	14.599	7.61
NBP1203 JPC36 3.76-3.77m	11.894	22.81	21.599	14.196	17.117	12.384
NBP1203 JPC36 3.81-3.82mb	12.57	10.07	12.878	16.973	22.437	25.071
NBP1203 JPC36 3.86-3.87m	12.982	15.243	17.03	17.813	20.361	16.57
NBP1203 JPC36 3.91-3.92mb	13.059	11.758	15.541	17.033	18.836	23.773
NBP1203 JPC36 3.96-3.97m	13.747	14.415	17.419	20.344	21.27	12.805

Figure A1-1 (cont.): Table continued on next page.

Sample name	<4µm	4-8µm	8-16µm	16-32µm	32-63µm	> 63µm
NBP1203 JPC36 4.01-4.02m	13.013	18.201	21.916	19.768	17.447	9.655
NBP1203 JPC36 4.06-4.07m	12.798	13.383	16.5	19.02	20.445	17.855
NBP1203 JPC36 4.11-4.12m	12.345	12.84	14.856	16.929	21.427	21.602
NBP1203 JPC36 4.16-4.17m	13.116	10.25	14.268	17.796	20.751	23.819
NBP1203 JPC36 4.21-4.22m	12.85	13.473	17.579	19.31	19.82	16.968
NBP1203 JPC36 4.26-4.27m	14.428	15.675	19.821	20.306	18.092	11.678
NBP1203 JPC36 4.31-4.32m	11.601	15.433	19.661	18.57	18.111	16.624
NBP1203 JPC36 4.36-4.37m	8.667	28.442	24.386	11.96	19.707	6.837
NBP1203 JPC36 4.41-4.42m	12.022	11.89	15.033	18.599	23.838	18.618
NBP1203 JPC36 4.46-4.47m	9.121	6.459	10.403	18.062	26.294	29.661
NBP1203 JPC36 4.51-4.52m	13.909	12.014	16.39	18.931	19.837	18.919
NBP1203 JPC36 4.56-4.57m	13.966	12.834	16.331	20.368	22.576	13.924
NBP1203 JPC36 4.61-4.62m	13.567	15.503	17.888	21.046	23.116	8.88
NBP1203 JPC36 4.66-4.67m	14.604	13.607	17.112	19.787	20.086	14.803
NBP1203 JPC36 4.71-4.72m	12.063	10.116	14.192	18.897	24.831	19.901
NBP1203 JPC36 4.76-4.77m	13.329	14.121	16.83	19.495	21.584	14.64
NBP1203 JPC36 4.81-4.82m	13.361	11.06	14.615	18.714	20.367	21.882
NBP1203 JPC36 4.86-4.87m	14.135	13.141	17.024	19.868	19.799	16.032
NBP1203 JPC36 4.91-4.92m	12.736	12.262	15.827	18.096	20.528	20.552
NBP1203 JPC36 4.96-4.97m	9.468	7.476	10.566	14.567	22.918	35.005
NBP1203 JPC36 5.01-5.02m	12.602	11.023	15.554	18.825	20.66	21.336
NBP1203 JPC36 5.06-5.07m	15.298	12.263	16.104	18.391	19.083	18.86
NBP1203 JPC36 5.11-5.12m	15.338	14.779	17.566	19.767	18.524	14.026
NBP1203 JPC36 5.16-5.17m	14.314	14.036	17.335	18.578	19.202	16.535
NBP1203 JPC36 5.21-5.22m	15.211	13.143	17.396	19.634	18.762	15.854
NBP1203 JPC36 5.26-5.27m	11.119	12.748	17.048	19.176	21.252	18.657
NBP1203 JPC36 5.31-5.32m	10.965	10.155	12.611	16.745	23.436	26.089
NBP1203 JPC36 5.36-5.37m	12.528	9.767	13.673	17.646	21.376	25.01
NBP1203 JPC36 5.41-5.42m	14.697	13.323	17.263	17.865	18.399	18.453
NBP1203 JPC36 5.46-5.47m	12.986	13.093	18.69	21.486	20.46	13.285
NBP1203 JPC36 5.51-5.52m	11.538	15.945	20.548	21.073	21.024	9.871
NBP1203 JPC36 5.56-5.57m	10.218	14.111	18.374	20.098	22.901	14.298
NBP1203 JPC36 5.61-5.62m	9.983	16.07	20.769	20.427	20.252	12.5
NBP1203 JPC36 5.66-5.67m	13.98	16.692	19.212	18.382	20.248	11.486
NBP1203 JPC36 5.71-5.72m	11.202	18.307	20.603	22.004	21.698	6.185
NBP1203 JPC36 5.76-5.77m	13.647	15.748	19.955	20.408	18.373	11.869
NBP1203 JPC36 5.81-5.82m	14.047	18.337	19.766	18.638	18.882	10.33

Figure A1-1 (cont.): Table continued on next page.

Sample name	<4µm	4-8µm	8-16µm	16-32µm	32-63µm	> 63µm
NBP1203 JPC36 5.86-5.87m	14.478	16.829	18.338	19.499	20.16	10.696
NBP1203 JPC36 5.91-5.92m	13.605	15.844	18.273	18.304	19.314	14.661
NBP1203 JPC36 5.96-5.97m	15.112	13.59	16.069	17.913	19.146	18.17
NBP1203 JPC36 6.01-6.02m	14.574	16.034	18.966	19.072	18.518	12.835
NBP1203 JPC36 6.06-6.07m	14.74	15.96	18.994	19.476	18.293	12.537
NBP1203 JPC36 6.11-6.12m	12.17	14.611	17.777	19.276	19.846	16.32
NBP1203 JPC36 6.16-6.17m	13.973	15.486	17.433	18.98	20.221	13.908
NBP1203 JPC36 6.21-6.22m	14.428	13.507	16.318	17.738	18.618	19.391
NBP1203 JPC36 6.26-6.27m	12.767	10.916	14.896	18.968	21.489	20.964
NBP1203 JPC36 6.31-6.32m	15.194	15.363	17.517	18.309	19.028	14.589
NBP1203 JPC36 6.36-6.37m	12.809	20.162	21.607	17.724	18.73	8.968
NBP1203 JPC36 6.41-6.42m	14.096	18.55	21.002	18.828	16.775	10.75
NBP1203 JPC36 6.46-6.47m	14.168	14.328	15.92	17.325	19.283	18.976
NBP1203 JPC36 6.51-6.52m	14.166	14.1	16.427	17.051	18.538	19.718
NBP1203 JPC36 6.56-6.57m	15.836	16.511	19.153	19.042	18.836	10.623
NBP1203 JPC36 6.61-6.62m	14.46	17.725	18.699	18.365	19.171	11.58
NBP1203 JPC36 6.66-6.67m	13.554	14.827	17.986	18.213	19.388	16.032
NBP1203 JPC36 6.71-6.72m	14.73	15.442	18.651	18.648	18.238	14.291
NBP1203 JPC36 6.76-6.77m	13.576	15.005	17.618	17.98	20.779	15.042
NBP1203 JPC36 6.81-6.82m	14.855	11.882	15.199	17.688	20.039	20.336
NBP1203 JPC36 6.86-6.87m	12.885	11.762	15.943	17.92	19.804	21.686
NBP1203 JPC36 6.91-6.92m	11.987	13.518	17.309	17.768	21.151	18.267
NBP1203 JPC36 6.96-6.97m	11.813	9.242	13.203	17.943	23.051	24.747
NBP1203 JPC36 7.01-7.02m	12.345	12.119	15.434	17.879	21.145	21.078
NBP1203 JPC36 7.06-7.07m	12.463	14.293	18.244	18.987	19.271	16.742
NBP1203 JPC36 7.11-7.12m	12.591	14.573	18.001	18.625	19.418	16.792
NBP1203 JPC36 7.16-7.17m	14.002	14.161	16.523	18.327	19.441	17.546
NBP1203 JPC36 7.21-7.22m	11.388	9.403	13.312	17.965	23.06	24.872
NBP1203 JPC36 7.26-7.27m	14.459	14.432	17.566	19.925	19.639	13.979
NBP1203 JPC36 7.31-7.32m	11.176	12.797	15.83	18.538	22.178	19.481
NBP1203 JPC36 7.36-7.37m	10.23	11.96	14.365	16.074	23.209	24.163
NBP1203 JPC36 7.41-7.42m	10.889	10.534	14.863	16.601	19.904	27.209
NBP1203 JPC36 7.46-7.47m	12.767	12.482	16.766	19.541	20.193	18.251
NBP1203 JPC36 7.51-7.52m	14.403	13.351	16.835	17.983	18.727	18.701
NBP1203 JPC36 7.56-7.57m	14.533	15.22	18.361	18.905	18.967	14.014
NBP1203 JPC36 7.61-7.62m	14.916	16.896	18.559	18.308	18.362	12.959
NBP1203 JPC36 7.66-7.67m	12.946	14.742	16.591	17.766	20.264	17.69
NBP1203 JPC36 7.71-7.72m	13.719	12.95	16.338	17.991	19.826	19.177

Figure A1-1 (cont.): Table continued on next page.

Sample name	<4µm	4-8µm	8-16µm	16-32µm	32-63µm	> 63µm
NBP1203 JPC36 7.76-7.77m	13.011	13.132	16.256	18.274	20.474	18.853
NBP1203 JPC36 7.81-7.82m	14.226	13.311	16.063	17.882	20.117	18.4
NBP1203 JPC36 7.86-7.87m	13.09	11.043	14.378	17.806	21.088	22.596
NBP1203 JPC36 7.91-7.92m	10.962	10.534	13.506	21.256	25.206	18.535
NBP1203 JPC36 7.96-7.97m	13.615	12.904	16.186	22.004	23.003	12.287
NBP1203 JPC36 8.01-8.02m	10.646	8.136	11.522	16.895	23.208	29.593
NBP1203 JPC36 8.06-8.07m	14.486	12.092	15.635	19.775	22.182	15.831
NBP1203 JPC36 8.11-8.12m	15.047	12.479	14.811	20.482	22.34	14.84
NBP1203 JPC36 8.16-8.17m	16.521	12.493	15.627	18.74	19.684	16.935
NBP1203 JPC36 8.21-8.22m	15.055	13.671	15.458	18.945	21.761	15.109
NBP1203 JPC36 8.26-8.27m	15.346	13.937	16.104	19.261	20.614	14.739
NBP1203 JPC36 8.31-8.32m	16.88	12.625	16.405	18.638	18.379	17.073
NBP1203 JPC36 8.36-8.37m	13.692	14.527	17.426	18.852	20.425	15.078
NBP1203 JPC36 8.41-8.42m	17.344	22.63	23.233	15.631	13.737	7.424
NBP1203 JPC36 8.46-8.47m	14.946	21.087	20.925	15.577	18.058	9.406
NBP1203 JPC36 8.51-8.52m	13.193	14.894	15.958	17.199	22.692	16.064
NBP1203 JPC36 8.56-8.57m	13.029	13.585	16.545	17.563	19.727	19.551
NBP1203 JPC36 8.61-8.62m	13.794	12.762	15.26	18.816	20.638	18.73
NBP1203 JPC36 8.66-8.67m	14.486	15.451	18.266	23.3	21.524	6.973
NBP1203 JPC36 8.71-8.72m	13.72	13.015	16.112	21.143	22.372	13.638
NBP1203 JPC36 8.76-8.77m	16.36	13.996	17.587	20.592	19.13	12.335
NBP1203 JPC36 8.81-8.82m	15.436	14.52	18.237	20.856	18.409	12.542
NBP1203 JPC36 8.86-8.87m	13.252	12.338	15.623	20.843	23.993	13.951
NBP1203 JPC36 8.91-8.92m	13.146	12.022	15.308	21.523	24.174	13.827
NBP1203 JPC36 8.96-8.97m	12.698	12.722	17.116	20.201	21.91	15.353
NBP1203 JPC36 9.01-9.02m	14.133	13.712	17.641	20.641	21.062	12.811
NBP1203 JPC36 9.06-9.07m	15.112	18.364	21.373	17.645	15.943	11.563
NBP1203 JPC36 9.11-9.12m	12.743	13.754	17.523	19.734	22.265	13.981
NBP1203 JPC36 9.16-9.17m	14.185	13.049	15.919	19.19	22.196	15.46
NBP1203 JPC36 9.21-9.22m	12.413	13.857	15.833	18.932	22.927	16.037
NBP1203 JPC36 9.26-9.27m	12.273	12.878	15.629	20.307	23.182	15.731
NBP1203 JPC36 9.31-9.32m	13.074	11.821	14.976	19.736	23.194	17.199
NBP1203 JPC36 9.36-9.37m	13.537	12.637	16.878	19.616	19.57	17.762
NBP1203 JPC36 9.41-9.42m	13.531	12.48	15.553	19.252	21.6	17.585
NBP1203 JPC36 9.46-9.47m	12.075	10.427	14.213	19.113	21.045	23.126
NBP1203 JPC36 9.51-9.52m Void	0	0	0	0	0	0

Figure A1-1 (cont.): Table continued on next page.

Sample name	<4µm	4-8µm	8-16µm	16-32µm	32-63µm	> 63µm
NBP1203 JPC36 9.56-9.57m	8.746	7.760	25.014	18	27	13
NBP1203 JPC36 9.61-9.62m Void	0	0	0	0	0	0
NBP1203 JPC36 9.66-9.67m	12.965	11.461	14.918	21.574	23.978	15.103
NBP1203 JPC36 9.71-9.72m	13.927	12.343	16.37	19.939	21.268	16.153
NBP1203 JPC36 9.76-9.77m	15.4	12.54	16.202	20.61	20.23	15.018
NBP1203 JPC36 9.81-9.82m	15.854	16.359	19.371	19.438	18.102	10.876
NBP1203 JPC36 9.86-9.87m	12.733	13.396	16.917	20.826	21.541	14.587
NBP1203 JPC36 9.91-9.92m	14.061	12.946	15.974	18.901	20.917	17.2
NBP1203 JPC36 9.96-9.97m	14.553	12.146	16.176	19.454	20.972	16.699
NBP1203 JPC36 10.01-10.02m	14.486	12.98	16.158	18.62	20.173	17.583
NBP1203 JPC36 10.06-10.07m	13.643	14.291	16.193	20.753	21.846	13.274
NBP1203 JPC36 10.11-10.12m	13.025	11.862	14.878	18.363	22.487	19.385
NBP1203 JPC36 10.16-10.17m	14.712	14.511	17.524	19.378	20.434	13.441
NBP1203 JPC36 10.21-10.22m	12.95	10.855	14.295	17.399	20.745	23.757
NBP1203 JPC36 10.26-10.27m	14.006	16.188	19.101	19.88	19.473	11.352
NBP1203 JPC36 10.31-10.32m	13.611	12.099	16.377	19.82	21.01	17.083
NBP1203 JPC36 10.36-10.37m	12.349	10.621	14.984	19.018	20.194	22.834
NBP1203 JPC36 10.41-10.42m	14.239	15.219	19.243	21.332	18.841	11.126
NBP1203 JPC36 10.46-10.47m	10.05	18.751	19.747	19.31	23.77	8.372
NBP1203 JPC36 10.51-10.52m	14.066	13.542	16.99	19.286	19.435	16.681
NBP1203 JPC36 10.56-10.57m	14.75	16.794	18.314	19.03	19.422	11.691
NBP1203 JPC36 10.61-10.62m	12.54	16.683	18.336	21.335	22.417	8.689
NBP1203 JPC36 10.66-10.67m	14.157	15.039	16.785	19.699	21.105	13.214
NBP1203 JPC36 10.71-10.72m	13.143	14.932	17.876	20.42	21.874	11.755
NBP1203 JPC36 10.76-10.77m	14.486	13.866	17.159	19.908	19.737	14.845
NBP1203 JPC36 10.81-10.82m	14.828	11.8	16.132	19.516	19.799	17.925
NBP1203 JPC36 10.86-10.87m	14.623	12.18	16.351	19.136	20.862	16.849
NBP1203 JPC36 10.91-10.92m	16.179	17.317	20.651	19.008	16.55	10.295
NBP1203 JPC36 10.96-10.97m	13.761	14.756	17.235	18.909	21.738	13.6
NBP1203 JPC36 11.01-11.02m	9.656	10.088	10.87	25.272	32.652	11.463
NBP1203 JPC36 11.06-11.07m	15.914	15.526	18.159	18.948	18.921	12.531
NBP1203 JPC36 11.11-11.12m	14.13	15.72	17.957	19.044	21.104	12.045
NBP1203 JPC36 11.16-11.17m	17.56	13.842	17.904	19.971	18.466	12.257
NBP1203 JPC36 11.21-11.22m	13.748	14.022	17.567	19.089	19.66	15.914
NBP1203 JPC36 11.26-11.27m	13.902	12.721	17.208	20.105	20.423	15.64
NBP1203 JPC36 11.31-11.32m	15.14	13.191	17.513	20.484	19.207	14.465
NBP1203 JPC36 11.36-11.37m	14.632	14.849	18.337	19.774	18.802	13.606

Figure A1-1 (cont.): Table continued on next page. Ikaite intervals are highlighted in blue.

Sample name	<4µm	4-8µm	8-16µm	16-32µm	32-63µm	> 63µm
NBP1203 JPC36 11.41-11.42m	16.15	14.978	18.267	20.688	18.85	11.067
NBP1203 JPC36 11.46-11.47m	13.585	14.331	17.871	19.549	19.462	15.202
NBP1203 JPC36 11.51-11.52m	14.006	13.672	16.403	19.451	20.754	15.715
NBP1203 JPC36 11.56-11.57m	12.51	14.397	15.397	21.691	26.434	9.572
NBP1203 JPC36 11.61-11.62m	13.594	13.753	16.035	20.355	23.378	12.885
NBP1203 JPC36 11.66-11.67m	12.684	11.4	14.478	20.849	24.061	16.527
NBP1203 JPC36 11.71-11.72m	12.857	13.23	18.021	21.589	19.781	14.523
NBP1203 JPC36 11.76-11.77m	12.209	12.613	17.238	21.099	21.364	15.477
NBP1203 JPC36 11.81-11.82m	13.674	11.444	14.801	20.1	23.022	16.959
NBP1203 JPC36 11.86-11.87m	12.965	16.728	18.723	18.933	21.029	11.623
NBP1203 JPC36 11.91-11.92m	14.364	13.708	16.641	20.253	20.69	14.345
NBP1203 JPC36 11.96-11.97m	16.646	15.574	18.591	21.109	17.859	10.222
NBP1203 JPC36 12.01-12.02m	14.065	16.119	18.489	18.81	19.694	12.824
NBP1203 JPC36 12.06-12.07m	13.774	12.342	14.925	19.459	22.547	16.954
NBP1203 JPC36 12.11-12.12m	15.362	17.157	18.372	18.903	20.41	9.797
NBP1203 JPC36 12.16-12.17m	14.534	12.926	16.113	18.11	18.946	19.371
NBP1203 JPC36 12.21-12.22m	12.213	11.883	13.455	20.838	28.108	13.503
NBP1203 JPC36 12.26-12.27m	15.957	12.583	15.458	19.749	20.867	15.386
NBP1203 JPC36 12.31-12.32m	16.825	13.141	16.37	19.301	18.788	15.575
NBP1203 JPC36 12.36-12.37m	17.329	13.881	17.539	21.09	17.633	12.528
NBP1203 JPC36 12.41-12.42m	12.488	24.532	20.702	13.976	18.448	9.854
NBP1203 JPC36 12.46-12.47mb	14.918	12.481	13.932	19.561	23.593	15.515
NBP1203 JPC36 12.51-12.52m	16.78	15.829	21.231	21.934	16.347	7.879
NBP1203 JPC36 12.56-12.57m	14.081	15.11	19.224	22.202	20.295	9.088
NBP1203 JPC36 12.61-12.62m	12.814	18.28	18.468	20.898	21.888	7.653
NBP1203 JPC36 12.66-12.67m	10.558	19.724	19.708	18.947	22.723	8.339
NBP1203 JPC36 12.71-12.72m	12.357	13.772	16.988	23.243	21.752	11.888
NBP1203 JPC36 12.76-12.77m	16.229	14.96	18.393	20.602	19.656	10.162
NBP1203 JPC36 12.81-12.82m	14.275	14.287	17.381	19.629	19.915	14.514
NBP1203 JPC36 12.86-12.87m	13.469	12.281	16.484	20.131	19.879	17.755
NBP1203 JPC36 12.91-12.92m	13.337	15.821	20.164	21.412	18.926	10.34
NBP1203 JPC36 12.96-12.97m	14.327	13.106	17.14	20.56	18.992	15.875
NBP1203 JPC36 13.01-13.02m	13.937	15.767	18.789	26.018	24.91	0.578
NBP1203 JPC36 13.06-13.07m	14.335	12.44	16.996	20.396	19.548	16.285
NBP1203 JPC36 13.11-13.12m	12.804	13.142	16.276	18.506	21.777	17.495
NBP1203 JPC36 13.16-13.17m	14.836	14.341	18.464	22.288	20.107	9.965

Figure A1-1 (cont.): Table continued on next page.

Sample name	<4µm	4-8µm	8-16µm	16-32µm	32-63µm	> 63µm
NBP1203 JPC36 13.21-13.22m	14.699	14.581	16.368	19.401	22.014	12.938
NBP1203 JPC36 13.26-13.27m	15.354	15.424	18.736	19.094	18.474	12.917
NBP1203 JPC36 13.31-13.32m	15.361	14.957	19.305	20.609	18.334	11.434
NBP1203 JPC36 13.36-13.37m	17.018	13.949	17.89	20.534	18.796	11.813
NBP1203 JPC36 13.41-13.42m	13.172	14.228	19.958	22.747	19.116	10.779
NBP1203 JPC36 13.46-13.47m	13.019	16.213	17.219	17.399	17.137	19.014
NBP1203 JPC36 13.51-13.52m	13.337	13.445	18.005	20.653	19.115	15.444
NBP1203 JPC36 13.56-13.57m	13.579	14.656	19.791	21.547	18.89	11.535
NBP1203 JPC36 13.61-13.62m	14.857	15.284	18.871	20.615	18.913	11.461
NBP1203 JPC36 13.66-13.67m	15.187	16.814	18.041	17.721	22.042	10.196
NBP1203 JPC36 13.71-13.72m	16.679	15.382	18.277	18.618	18.047	12.999
NBP1203 JPC36 13.76-13.77m	9.156	25.374	20.935	17.129	22.969	4.437
NBP1203 JPC36 13.81-13.82m	10.876	21.02	20.328	15.85	23.791	8.135
NBP1203 JPC36 13.86-13.87m	15.425	15.508	16.713	16.117	18.063	18.175
NBP1203 JPC36 13.91-13.92m	17.12	13.957	16.787	19.143	18.642	14.351
NBP1203 JPC36 13.96-13.97m	15.241	12.944	16.176	18.479	18.382	18.779
NBP1203 JPC36 14.01-14.02m	15.608	13.053	15.261	18.418	20.015	17.645
NBP1203 JPC36 14.06-14.07m	16.375	13.358	16.307	19.446	20.565	13.95
NBP1203 JPC36 14.11-14.12m	15.957	13.121	17.344	19.424	18.872	15.283
NBP1203 JPC36 14.16-14.17m	10.859	10.709	15.633	19.656	22.964	20.179
NBP1203 JPC36 14.21-14.22m	12.512	11.409	15.361	18.614	22.057	20.046
NBP1203 JPC36 14.26-14.27m	12.864	11.826	15.426	18.471	21.223	20.19
NBP1203 JPC36 14.31-14.32m	9.321	7.161	10.647	16.844	25.672	30.354
NBP1203 JPC36 14.36-14.37m	12.755	11.128	14.409	17.598	21.507	22.604
NBP1203 JPC36 14.41-14.42m	15.481	17.559	20.088	18.856	15.116	12.9
NBP1203 JPC36 14.46-14.47m	11.431	24.321	21.306	15.053	19.165	8.722
NBP1203 JPC36 14.51-14.52m	13.71	13.127	17.004	20.591	20.794	14.775
NBP1203 JPC36 14.56-14.57m	12.609	19.967	19.992	18.176	19.1	10.157
NBP1203 JPC36 14.61-14.62m	16.539	13.029	15.894	18.175	19.496	16.868
NBP1203 JPC36 14.62-14.63m	5.042	6.888	35.996	25.215	20.065	6.795
NBP1203 JPC36 14.63-14.64m	11.286	9.658	26.766	19.460	25.623	7.206
NBP1203 JPC36 14.64-14.65m	9.437	10.137	30.756	18.614	24.389	6.666
NBP1203 JPC36 14.65-14.66m	5.671	7.335	34.135	24.881	21.529	6.449
NBP1203 JPC36 14.66-14.67m	15.603	13.756	15.804	18.469	21.225	15.143
NBP1203 JPC36 14.71-14.72m	9.872	21.691	17.635	16.419	24.563	9.82
NBP1203 JPC36 14.76-14.77m	13.022	14.487	17.249	17.235	20.071	17.936
NBP1203 JPC36 14.78-14.79m	9.085	9.740	29.522	19.506	23.130	9.017

Figure A1-1 (cont.): Table continued on next page. Ikaite intervals are highlighted in blue.

Sample name	<4µm	4-8µm	8-16µm	16-32µm	32-63µm	> 63µm
NBP1203 JPC36 14.79-14.8m	10.093	10.171	30.117	19.386	22.591	7.643
NBP1203 JPC36 14.81-14.82m	15.775	15.087	19.011	20.389	17.354	12.383
NBP1203 JPC36 14.86-14.87m	15.71	13.692	17.113	20.931	19.102	13.451
NBP1203 JPC36 14.91-14.92m	15.754	13.948	17.638	20.299	18.661	13.701
NBP1203 JPC36 14.96-14.97m	13.913	13.28	17.855	21.907	20.5	12.546
NBP1203 JPC36 15.01-15.02m	16.488	14.226	18.059	20.785	19.433	11.009
NBP1203 JPC36 15.06-15.07m	16.887	14.988	18.945	20.853	17.614	10.714
NBP1203 JPC36 15.11-15.12m	16.964	18.912	20.002	17.905	15.96	10.257
NBP1203 JPC36 15.16-15.17m	14.895	17.669	20.897	19.721	19.237	7.58
NBP1203 JPC36 15.21-15.22m	15.67	16.077	19.101	20.337	18.611	10.204
NBP1203 JPC36 15.26-15.27m	18.061	16.352	18.349	19.856	17.395	9.988
NBP1203 JPC36 15.31-15.32m	15.733	13.651	15.431	20.055	22.781	12.349
NBP1203 JPC36 15.36-15.37m	17.935	30.267	24.196	11.608	11.515	4.478
NBP1203 JPC36 15.41-15.42m Void	0	0	0	0	0	0
NBP1203 JPC36 15.46-15.47m Void	0	0	0	0	0	0
NBP1203 JPC36 15.51-15.52m Void	0	0	0	0	0	0
NBP1203 JPC36 15.56-15.57m	12.275	25.086	22.259	16.14	18.915	5.325
NBP1203 JPC36 15.61-15.62m	16.293	14.864	16.269	20.424	21.982	10.168
NBP1203 JPC36 15.66-15.67m	16.451	15.995	17.463	17.973	18.566	13.553
NBP1203 JPC36 15.71-15.72m	14.985	14.361	16.742	18.847	21.393	13.672
NBP1203 JPC36 15.76-15.77m	15.702	16.317	16.992	17.092	19.368	14.53
NBP1203 JPC36 15.81-15.82m	17.236	14.628	16.248	16.947	18.149	16.793
NBP1203 JPC36 15.86-15.87m	13.072	14.351	16.776	17.754	19.939	18.108
NBP1203 JPC36 15.91-15.92m	12.337	14.271	16.692	20.085	22.134	14.482
NBP1203 JPC36 15.96-15.97m	14.164	12.444	16.53	19.68	20.711	16.471
NBP1203 JPC36 16.01-16.02m	11.686	10.432	14.346	18.072	20.904	24.56
NBP1203 JPC36 16.06-16.07m Void	0	0	0	0	0	0
NBP1203 JPC36 16.11-16.12m Void	0	0	0	0	0	0
NBP1203 JPC36 16.16-16.17m Void	0	0	0	0	0	0
NBP1203 JPC36 16.21-16.22m Void	0	0	0	0	0	0
NBP1203 JPC36 16.26-16.27m Void	0	0	0	0	0	0

Figure A1-1 (cont.): Table continued on next page. Ikaite intervals are highlighted in blue.

Sample name	<4µm	4-8µm	8-16µm	16-32µm	32-63µm	> 63µm
NBP1203 JPC36 16.31-16.32m	14.135	12.831	17.005	20.802	21.793	13.434
NBP1203 JPC36 16.36-16.37m Void	0	0	0	0	0	0
NBP1203 JPC36 16.41-16.42m	13.762	13.849	19.863	23.264	19.694	9.568
NBP1203 JPC36 16.46-16.47m	15.095	14.443	17.278	20.287	20.87	12.026
NBP1203 JPC36 16.51-16.52m	12.49	16.2	17.361	19.595	24.286	10.067
NBP1203 JPC36 16.56-16.57m	12.909	19.561	18.963	19.402	21.246	7.92
NBP1203 JPC36 16.61-16.62m	13.087	14.822	19.555	22.078	20.319	10.14
NBP1203 JPC36 16.66-16.67m	10.705	18.389	17.326	18.963	26.56	8.058
NBP1203 JPC36 16.71-16.72m	16.371	14.209	17.496	20.499	20.385	11.04
NBP1203 JPC36 16.76-16.77m	14.292	15.13	17.533	21.338	21.404	10.304
NBP1203 JPC36 16.81-16.82m	8.917	20.228	20.717	18.766	23.448	7.924
NBP1203 JPC36 16.86-16.87m	13.393	21.746	21.772	18.244	17.462	7.382
NBP1203 JPC36 16.91-16.92m Void	0	0	0	0	0	0
NBP1203 JPC36 16.96-16.97m	16.057	17.045	19.981	21.009	17.996	7.912
NBP1203 JPC36 17.01-17.02m	14.821	15.752	18.865	20.273	18.24	12.049
NBP1203 JPC36 17.06-17.07m	13.479	12.774	16.523	19.681	20.717	16.825
NBP1203 JPC36 17.11-17.12m	16.173	15.275	18.602	19.377	17.804	12.769
NBP1203 JPC36 17.16-17.17m Void	0	0	0	0	0	0
NBP1203 JPC36 17.21-17.22m Void	0	0	0	0	0	0
NBP1203 JPC36 17.26-17.27m	16.031	15.203	18.07	20.1	18.001	12.595
NBP1203 JPC36 17.31-17.32m	17.789	15.724	18.524	20.954	17.87	9.138
NBP1203 JPC36 17.32-17.33m	9.732	12.532	31.477	18.003	23.947	4.309
NBP1203 JPC36 17.36-17.37m	15.93	15.27	18.037	19.628	18.272	12.863
NBP1203 JPC36 17.41-17.42m	14.783	15.685	18.59	19.452	17.399	14.09
NBP1203 JPC36 17.45-17.46m	8.725	8.677	25.269	19.346	27.119	10.865
NBP1203 JPC36 17.46-17.47m	11.725	13.043	16.744	23.154	23.143	12.192
NBP1203 JPC36 17.51-17.52m	13.867	15.293	21.809	22.452	16.498	10.082
NBP1203 JPC36 17.56-17.57m	15.052	15.234	19.85	22.584	17.136	10.144
NBP1203 JPC36 17.61-17.62m	14.337	15.003	17.556	21.139	20.882	11.084
NBP1203 JPC36 17.66-17.67m	14.211	23.555	21.304	17.201	16.009	7.719
NBP1203 JPC36 17.71-17.72m	16.451	15.036	17.09	20.356	19.616	11.451
NBP1203 JPC36 17.76-17.77m	14.969	13.516	15.596	21.555	22.263	12.102
NBP1203 JPC36 17.81-17.82m	13.164	15.036	18.469	21.074	19.05	13.208

Figure A1-1 (cont.): Table continued on next page. Ikaite intervals are highlighted in blue.

Sample name	<4µm	4-8µm	8-16µm	16-32µm	32-63µm	> 63µm
NBP1203 JPC36 17.86-17.87m Void	0	0	0	0	0	0
NBP1203 JPC36 17.91-17.92m Void	0	0	0	0	0	0
NBP1203 JPC36 17.96-17.97m Void	0	0	0	0	0	0
NBP1203 JPC36 18.01-18.02m Void	0	0	0	0	0	0
NBP1203 JPC36 18.06-18.07m Void	0	0	0	0	0	0
NBP1203 JPC36 18.11-18.12m	15.406	14.628	16.561	20.374	21.455	11.577
NBP1203 JPC36 18.16-18.17m	15.913	13.64	15.843	21.208	22.048	11.347
NBP1203 JPC36 18.21-18.22m	13.584	19.423	20.159	19.001	18.525	9.309
NBP1203 JPC36 18.26-18.27m	15.283	13.719	16.623	20.828	21.116	12.433
NBP1203 JPC36 18.31-18.32mb	16.413	15.873	18.256	19.608	17.812	12.038
NBP1203 JPC36 18.36-18.37m	16.148	12.331	15.646	19.768	20.894	15.212
NBP1203 JPC36 18.41-18.42m	14.832	12.98	15.494	21.506	23.026	12.162
NBP1203 JPC36 18.46-18.47m	14.769	15.405	18.641	19.708	18.907	12.57
NBP1203 JPC36 18.51-18.52m	13.577	13.987	16.32	19.156	21.377	15.583
NBP1203 JPC36 18.56-18.57m	17.015	14.597	17.384	19.715	17.948	13.341
NBP1203 JPC36 18.61-18.62m	15.646	15.474	18.735	20.477	19.19	10.477
NBP1203 JPC36 18.66-18.67m	14.568	13.979	17.398	21.151	19.71	13.193
NBP1203 JPC36 18.71-18.72m	16.486	12.524	15.729	20.063	20.806	14.391
NBP1203 JPC36 18.72-18.73m	8.055	7.674	20.288	16.213	40.775	6.996
NBP1203 JPC36 18.73-18.74m	7.351	8.762	22.809	15.629	34.535	10.913
NBP1203 JPC36 18.74-18.75m	5.698	12.888	26.981	11.841	35.092	7.500
NBP1203 JPC36 18.75-18.76m	8.251	8.732	26.923	19.302	24.232	12.561
NBP1203 JPC36 18.76-18.77m	14.294	11.322	15.238	18.713	20.339	20.093
NBP1203 JPC36 18.77-18.78m	11.723	9.890	27.672	19.968	25.886	4.862
NBP1203 JPC36 18.81-18.82m	15.63	14.725	16.759	20.188	20.422	12.276
NBP1203 JPC36 18.86-18.87m	15.554	13.156	15.859	20.116	20.561	14.754
NBP1203 JPC36 18.91-18.92m	15.983	14.607	16.328	21.535	22.308	9.24
NBP1203 JPC36 18.96-18.97m	14.502	15.733	17.437	19.758	20.927	11.643
NBP1203 JPC36 19.01-19.02m	16.737	16.887	17.552	19.23	21.98	7.614
NBP1203 JPC36 19.06-19.07m	17.789	15.06	17.409	19.006	18.675	12.061
NBP1203 JPC36 19.11-19.12m	12.898	20.407	17.823	17.644	23.797	7.431

Figure A1-1 (cont.): Table continued on next page. Ikaite

intervals are highlighted in blue.

Sample name	<4µm	4-8µm	8-16µm	16-32µm	32-63µm	> 63µm
NBP1203 JPC36 19.16-19.17m	15.536	13.478	15.9	19.83	20.604	14.651
NBP1203 JPC36 19.21-19.22m	17.079	14.326	17.058	19.609	19.33	12.598
NBP1203 JPC36 19.26-19.27m	13.058	12.262	15.585	21.116	26.944	11.036
NBP1203 JPC36 19.31-19.32m	14.801	16.939	18.007	17.311	18.427	14.516
NBP1203 JPC36 19.36-19.37m	16.472	13.817	18.245	20.784	18.106	12.576
NBP1203 JPC36 19.41-19.42m	17.558	13.968	17.616	20.138	17.832	12.888
NBP1203 JPC36 19.46-19.47m	14.34	13.847	16.554	19.58	21.99	13.688
NBP1203 JPC36 19.51-19.52m	15.211	14.136	16.45	19.61	21.426	13.166
NBP1203 JPC36 19.56-19.57m	15.563	15.891	17.954	18.922	19.736	11.933
NBP1203 JPC36 19.61-19.62m	16.399	15.293	16.768	20.056	20.612	10.871
NBP1203 JPC36 19.66-19.67m	18.27	15.292	18.085	19.247	17.856	11.25
NBP1203 JPC36 19.71-19.72m	14.863	16.156	18.15	20.55	20.522	9.758
NBP1203 JPC36 19.76-19.77m	12.969	18.97	19.224	18.607	21.146	9.083
NBP1203 JPC36 19.81-19.82m	15.7	15.965	17.267	17.646	18.952	14.47
NBP1203 JPC36 19.86-19.87m	12.062	24.056	20.452	16.948	20.799	5.684
NBP1203 JPC36 19.91-19.92m	14.097	13.092	16.726	21.338	21.575	13.172
NBP1203 JPC36 19.96-19.97m	11.9	11.774	15.66	20.411	22.941	17.315
NBP1203 JPC36 20.01-20.02m	15.852	13.424	16.382	19.208	19.721	15.413
NBP1203 JPC36 20.06-20.07m	16.825	16.077	19.021	19.944	17.631	10.501
NBP1203 JPC36 20.11-20.12m	10.567	12.463	14.488	20.372	30.431	11.68
NBP1203 JPC36 20.16-20.17m	16.578	15.114	16.958	20.315	19.697	11.337
NBP1203 JPC36 20.21-20.22m	13.705	20.58	21.302	18.131	17.612	8.671
NBP1203 JPC36 20.26-20.27m	14.714	17.103	18.846	18.925	21.375	9.037
NBP1203 JPC36 20.31-20.32m	15.107	18.642	21.234	17.952	16.913	10.153
NBP1203 JPC36 20.36-20.37m	16.085	20.399	21.117	16.942	17.564	7.894
NBP1203 JPC36 20.41-20.42m	14.824	15.482	17.384	18.4	19.03	14.88
NBP1203 JPC36 20.46-20.47m	18.565	13.752	17.933	21.602	19.557	8.592
NBP1203 JPC36 20.51-20.52m	14.697	13.98	17.565	19.429	20.661	13.668
NBP1203 JPC36 20.56-20.57m	15.105	11.164	16.381	19.725	20.896	16.729
NBP1203 JPC36 20.61-20.62m	14.687	13.908	19.063	21.815	18.943	11.583
NBP1203 JPC36 20.66-20.67m	11.786	10.192	14.622	19.132	22.398	21.87
NBP1203 JPC36 20.71-20.72m	11.601	12.454	18.766	26.038	24.455	6.687
NBP1203 JPC36 20.76-20.77m	12.992	11.97	15.437	21.938	24.338	13.325
NBP1203 JPC36 20.81-20.82m	13.332	12.922	15.898	21.089	23.078	13.681
NBP1203 JPC36 20.83-20.84m	8.365	8.357	25.001	18.172	24.477	15.628
NBP1203 JPC36 20.84-20.85m	5.729	7.805	37.376	24.625	18.265	6.198
NBP1203 JPC36 20.86-20.87m	14.043	14.191	17.512	20.434	21.817	12.004

Figure A1-1 (cont.): Table continued on next page. Ikaite intervals are highlighted in blue.

Sample name	<4µm	4-8µm	8-16µm	16-32µm	32-63µm	> 63µm
NBP1203 JPC36 20.91-20.92m	15.496	12.747	16.425	20.294	20.702	14.336
NBP1203 JPC36 20.96-20.97m	15.806	12.394	15.401	20.37	21.438	14.591
NBP1203 JPC36 21.01-21.02mb	16.073	13.376	16.161	20.704	21.566	12.121
NBP1203 JPC36 21.06-21.07m	16.318	14.471	17.255	20.029	20.032	11.895
NBP1203 JPC36 21.11-21.12m	11.769	21.092	23.096	16.793	18.852	8.397
NBP1203 JPC36 21.16-21.17m	17.473	16.008	18.046	21.223	21.194	6.056
NBP1203 JPC36 21.21-21.22m	12.808	16.129	18.904	19.507	20.976	11.676
NBP1203 JPC36 21.26-21.27m	14.243	11.744	15.17	18.658	20.59	19.597
NBP1203 JPC36 21.31-21.32mb	15.068	13.38	15.935	20.394	20.943	14.28
NBP1203 JPC36 21.36-21.37m	16.322	20.669	22.391	16.784	17.405	6.43
NBP1203 JPC36 21.41-21.42mb	15.994	13.043	17.274	19.415	18.73	15.544
NBP1203 JPC36 21.46-21.47m	16.444	15.369	17.967	19.435	19.131	11.654
NBP1203 JPC36 21.51-21.52m	16.194	15.047	17.645	20.495	19.368	11.251
NBP1203 JPC36 21.56-21.57m	12.278	21.036	20.811	16.978	22.532	6.365
NBP1203 JPC36 21.61-21.62m	17.629	13.017	15.846	18.603	18.571	16.335
NBP1203 JPC36 21.66-21.67m	15.721	13.235	16.336	19.773	19.966	14.969
NBP1203 JPC36 21.71-21.72m	16.157	14.528	17.23	19.128	19.039	13.918
NBP1203 JPC36 21.76-21.77m	14.851	15.059	17.44	18.61	19.304	14.736
NBP1203 JPC36 21.81-21.82m	15.622	14.262	17.003	19.105	19.58	14.428
NBP1203 JPC36 21.86-21.87mb	16.321	13.431	16.82	20.214	19.415	13.799
NBP1203 JPC36 21.91-21.92m	17.028	13.395	16.387	18.923	18.575	15.691
NBP1203 JPC36 21.96-21.97m	13.444	14.393	16.728	19.578	21.302	14.554
NBP1203 JPC36 22.01-22.02m	12.975	11.516	15.832	19.288	21.095	19.294
NBP1203 JPC36 22.06-22.07m	15.784	13.402	18.1	20.309	18.044	14.36
NBP1203 JPC36 22.11-22.12m	14.318	14.616	18.442	19.984	18.777	13.864
NBP1203 JPC36 22.16-22.17m	11.919	10.026	13.598	18.354	22.374	23.73
NBP1203 JPC36 22.21-22.22m	15.896	15.284	17.707	19.014	18.629	13.471
NBP1203 JPC36 22.26-22.27m	16.323	14.573	17.115	20.616	19.644	11.729
NBP1203 JPC36 22.31-22.32m	14.036	11.708	14.477	19.796	22.284	17.701
NBP1203 JPC36 22.36-22.37m	16.442	15.332	18.566	19.581	17.688	12.391
NBP1203 JPC36 22.41-22.42m	8.256	24.222	22.785	17.763	22.224	4.751
NBP1203 JPC36 22.46-22.47m	14.826	25.048	23.817	13.316	15.99	7.003
NBP1203 JPC36 22.51-22.52m	14.889	23.756	23.571	14.671	13.904	9.208
NBP1203 JPC36 22.56-22.57m	13.094	12.49	16.328	19.884	21.261	16.942
NBP1203 JPC36 22.61-22.62m	14.193	12.65	16.358	19.787	20.053	16.958
NBP1203 JPC36 22.66-22.67m	11.287	12.276	16.405	19.324	20.798	19.91
NBP1203 JPC36 22.71-22.72m	16.377	14.998	19.373	20.504	17.172	11.576
NBP1203 JPC36 22.76-22.77m	14.594	16.228	18.26	20.688	23.286	6.944

Figure A1-1 (cont.): Table continued on next page.

Sample name	<4µm	4-8µm	8-16µm	16-32µm	32-63µm	> 63µm
NBP1203 JPC36 22.81-22.82mb	16.351	12.607	15.975	20.334	20.489	14.244
NBP1203 JPC36 22.86-22.87m	20.061	14.8	17.848	20.245	16.707	10.339
NBP1203 JPC36 22.91-22.92m	15.467	16.326	19.047	18.369	17.976	12.816
NBP1203 JPC36 22.96-22.97m	15.722	10.638	14.059	16.945	19.891	22.745
NBP1203 JPC36 23.01-23.02m	12.959	23.674	24.105	13.729	13.992	11.541
NBP1203 JPC36 23.06-23.07m	15.854	13.025	16.917	18.913	17.932	17.359
NBP1203 JPC36 23.11-23.12m	15.815	14.049	17.516	22.01	19.881	10.729
NBP1203 JPC36 23.16-23.17m	13.97	13.581	15.441	20.134	26.384	10.492
NBP1203 JPC36 23.21-23.22m	17.993	13.776	17.528	20.035	17.832	12.836
NBP1203 JPC36 23.26-23.27m	16.449	13.465	16.18	19.268	19.181	15.458
NBP1203 JPC36 23.31-23.32m	15.808	16.342	17.966	18.152	19.066	12.666
NBP1203 JPC36 23.36-23.37m	15.774	14.523	16.679	20.568	20.578	11.878
NBP1203 JPC36 23.39-23.4m	8.126	10.452	31.242	17.865	25.165	7.149
NBP1203 JPC36 23.41-23.42m	15.319	15.232	16.98	19.883	20.7	11.886
NBP1203 JPC36 23.46-23.47m	16.231	12.608	15.38	19.525	20.184	16.073
NBP1203 JPC36 23.51-23.52mc	16.301	16.129	18.059	16.887	16.731	15.893
NBP1203 JPC36 23.56-23.57m	16.615	16.137	18	17.149	17.558	14.542
NBP1203 JPC36 23.61-23.62m	17.306	16.936	18.455	18.956	17.427	10.919
NBP1203 JPC36 23.66-23.67m	16.03	16.633	18.17	18.986	19.093	11.088
NBP1203 JPC36 23.71-23.72m	16.747	15.748	18.022	19.753	19.28	10.451
NBP1203 JPC36 23.76-23.77m	15.745	14.422	16.749	19.963	20.882	12.24
NBP1203 JPC36 23.81-23.82m	13.083	16.859	21.869	20.318	17.573	10.298
NBP1203 JPC36 23.86-23.87m	10.042	14.848	19.607	20.046	21.115	14.343
NBP1203 JPC36 23.91-23.92m	19.148	12.709	16.639	20.361	18.672	12.472
NBP1203 JPC36 23.96-23.97m	17.45	12.074	15.212	18.632	18.996	17.635
NBP1203 JPC36 24.01-24.02m	12.567	11.627	15.74	20.1	23.298	16.669
NBP1203 JPC36 24.06-24.07m	13.904	13.019	18.55	22.829	20.647	11.051
NBP1203 JPC36 24.11-24.12m	10.607	15.083	14.49	22.833	29.417	7.569
NBP1203 JPC36 24.16-24.17m	13.259	16.823	19.429	21.879	20.701	7.908
NBP1203 JPC36 24.21-24.22m	15.675	16.637	21.384	21.333	16.162	8.81
NBP1203 JPC36 24.26-24.27m	14.328	14.574	16.725	21.197	22.972	10.204
NBP1203 JPC36 24.31-24.32m	12.304	20.804	22.566	18.01	18.426	7.89
NBP1203 JPC36 24.36-24.37m	10.948	19.228	20.473	18.477	21.663	9.211
NBP1203 JPC36 24.41-24.42m	16.318	14.877	17.414	21.142	20.175	10.073
NBP1203 JPC36 24.46-24.47m	15.984	11.949	14.871	20.704	22.442	14.051
NBP1203 JPC36 24.51-24.52m	15.893	14.68	19.24	21.721	18.439	10.027
NBP1203 JPC36 24.56-24.57m	14.012	20.045	22.865	20.617	16.687	5.774
NBP1203 JPC36 24.61-24.62m	15.929	13.439	16.382	21.19	21.332	11.727

Figure A1-1 (cont.): Table continued on next page. Ikaite intervals are highlighted in blue.

Sample name	<4µm	4-8µm	8-16µm	16-32µm	32-63µm	> 63µm
NBP1203 JPC36 24.66-24.67m	17.153	12.053	15.244	19.286	20.302	15.961
NBP1203 JPC36 24.71-24.72m	11.644	17.763	20.009	20.194	22.033	8.358
NBP1203 JPC36 24.76-24.77m	17.854	17.014	18.865	19.475	17.713	9.08
NBP1203 JPC36 24.81-24.82m	13.404	13.956	14.581	23.564	26.463	8.032
NBP1203 JPC36 24.86-24.87m	17.843	16.181	18.386	18.853	16.969	11.768
NBP1203 JPC36 24.91-24.92m	12.805	20.929	20.999	16.943	18.773	9.55
NBP1203 JPC36 24.96-24.97m	17.768	12.861	16.295	19.094	18.983	14.999
NBP1203 JPC36 25.01-25.02m	17.132	13.783	16.91	19.196	19.781	13.198
NBP1203 JPC36 25.06-25.07m	11.535	11.958	13.766	18.876	26.584	17.281
NBP1203 JPC36 25.11-25.12m	16.686	12.376	16.599	19.478	18.585	16.276
NBP1203 JPC36 25.16-25.17m	19.022	15.735	19.817	20.341	15.432	9.654
NBP1203 JPC36 25.21-25.22m	9.076	24.788	19.736	16.955	23.855	5.59
NBP1203 JPC36 25.26-25.27m	16.446	13.695	16.758	20.259	17.946	14.896
NBP1203 JPC36 25.31-25.32m	18.594	14.226	16.848	21.275	20.496	8.562
NBP1203 JPC36 25.36-25.37m	18.059	14.168	17.34	19.616	17.945	12.871
NBP1203 JPC36 25.41-25.42m	17.385	15.12	17.63	18.882	18.358	12.625
NBP1203 JPC36 25.46-25.47m	18.931	14.885	18.591	18.788	16.17	12.635
NBP1203 JPC36 25.51-25.52m	12.861	11.839	14.963	17.52	20.258	22.558
NBP1203 JPC36 25.56-25.57m	16.683	18.264	21.135	18.977	15.961	8.98
NBP1203 JPC36 25.61-25.62m	12.758	17.007	17.649	19.308	22.396	10.882
NBP1203 JPC36 25.66-25.67m	15.908	16.844	19.053	17.574	16.832	13.79
NBP1203 JPC36 25.71-25.72m	15.214	14.708	18.805	19.939	17.484	13.849
NBP1203 JPC36 25.76-25.77m	15.401	15.705	18.406	18.435	17.942	14.112
NBP1203 JPC36 25.81-25.82m Void	0	0	0	0	0	0

Figure A1-1 (cont.): Grain size data for NBP1203 JPC36.